Fundamental Processes in Single Molecule Junctions:
Interplay of Forces and Electronic Effects

Christian Lotze

Im Fachbereich Physik der Freien Universität Berlin
eingereichte Dissertation

18.7.2013

Diese Arbeit entstand in der Arbeitsgruppe von Prof. Dr. José Ignacio Pascual am Fachbereich Physik der Freien Universität Berlin.

Berlin, 18.7.2013

Erstgutachter: Prof. Dr. José Ignacio Pascual
Zweitgutachterin: Prof. Dr. Stephanie Reich
Drittgutachterin: Prof. Dr. Elke Scheer

Datum der Disputation: 19.9.2013

Kurzfassung

Diese Arbeit beschreibt die Untersuchung grundlegender Eigenschaften einzelner Moleküle im direkten oder Tunnelkontakt mit Hilfe von Rastertunnelmikroskopie (STM) und dynamischer Rasterkraftmikroskopie (AFM). Wir untersuchten vier verschiedene experimentelle Themen.

Beim Hochheben des molekularen Drahtes, 1,4-bis(pyridin-4-ylethynyl)benzene (BPEB), mit der Spitze eines STM beobachten wir einen atypischen Anstieg der elektrischen Leitfähigkeit. Mit Hilfe von Kraftfeld- und Dichtefunktionaltheorie (DFT) Simulationen können wir diesen Anstieg einer Strukturänderung im Molekül zuordnen. Die Rotation eines Pyridinrings geht einher mit der Rehybridisierung eines Kohlenstoffatoms von sp zu sp^2. Daraus resultiert eine Bindung zu einem Atom des Kupfersubstrates und folglich erhöhte elektronische Leitfähigkeit in das Substrat. In AFM-Messungen von Frequenzverschiebung gegen Abstand ($\Delta f(Z)$) beobachten wir nichtlineare, plastische Änderungen, die mit den Änderungen in der Leitfähigkeit korreliert sind und den Strukturänderungen des Moleküls zugeordnet werden können. Aus elastischen Bereichen der $\Delta f(Z)$-Spektren gewannen wir Werte für die der Rehybridisierung zugehörigen Bindungskräfte und Energien. DFT-Simulationen zeigen qualitative Übereinstimmungen mit den $\Delta f(Z)$ Spektren.

An einem Wasserstoffmolekül (H_2) Kontakt beobachten wir die Konversion von Energie aus Rauschen in gerichtete mechanische Energie. Die durch tunnelnde Elektronen zum zufälligen Schalten zwischen zwei Zuständen angeregten H_2-Moleküle, werden durch die Bewegung der oszillierenden AFM-Spitze in ihrer Schaltrate beeinflusst. Die H_2-Moleküle üben wiederum zustandsabhängige Kräfte auf die Spitze aus. Dies führt zu einer gegenseitigen Beeinflussung und schließlich einem effektiven Energieübertrag von den fluktuierenden H_2-Molekülen auf die Spitze. Dieses Prinzip ist als 'Stochastische Resonanz' bekannt und ermöglicht hier das Antreiben der AFM Stimmgabel.

Im Ladungstransferkomplex tetramethyltetrathiafulvalene-tetracyanoquinodimethane (TMTTF-TCNQ) untersuchen wir das (Ent)Laden von TCNQ mittels AFM. In AFM Δf-Spektren manifestiert sich das (Ent)Laden in einem Dip, der mit dem Prozess selbst korreliert ist. Wir beobachten eine Verschiebung von lokaler Kontaktpotentialdifferenz (LCPD) und Δf beim Wechsel in den jeweils anderen Ladungszustand. Das dynamische (Ent)Laden durch die oszillierende AFM-Spitze verursacht periodische Kräfte, die jedoch keinen Einfluss auf die Energiedissipation haben. Weiterhin beobachten wir, dass sich die Ladungszustände benachbarter Moleküle gegenseitig beeinflussen.

Schließlich untersuchen wir die zwitterionische Merocyanin-Form (MC) des molekularen Schalters 1,3,3-Trimethylindolino-6'nitrobenzopyrylospiran. Durch ortsaufgelöste $\Delta f(V_s)$ Spektroskopie können wir die intramolekulare (Dipol-)Ladungsverteilung auch auf der Oberfläche nachweisen. Wir beobachten eine Abschirmung der Ladungen durch im Substrat induzierte Spiegelladungen und die benachbarten Moleküle. Der Vergleich von DFT-Simulationen und ortsaufgelösten $LCPD$-Messungen ermöglicht uns das MC-Strukturmodell zu verbessern. Im repulsiven Kontakt zwischen Spitze und einer Methyl-Gruppe des Moleküls beobachten wir eine $LCPD$-Inversion. Wir interpretieren dies als eine Art Umkehr der Spitzen-Proben Geometrie, in dem das Molekül praktisch zu einem Teil der messenden Spitze wird.

Abstract

This thesis describes the investigation of fundamental properties of single molecules in the tunneling junction or tip contact, using combined scanning tunneling microscopy (STM) and atomic force microscopy (AFM). The experiments were performed in a setup that was in the beginning of this thesis planned, constructed and successfully taken into operation. Here, we address four different experimental topics.

We lift a molecular wire, 1,4-bis(pyridin-4-ylethynyl)benzene (BPEB), with the STM/AFM tip from a copper surface. During lift-up we observe an atypical increase of the conductance. In force field simulations we observe a structural change, the rotation of a pyridine ring. Density functional theory (DFT) simulations show that the ring rotation goes along with a rehybridization of a carbon atom from sp to sp^2. The additional bond is formed between the C and a surface atom and allows for current flow directly into the Cu substrate. In AFM $\Delta f(Z)$ spectra we observe a plastic non-linear change that is correlated with the increase in the conductance and can thus be assigned to the rehybridization. From $\Delta f(Z)$ in the elastic regime we obtain values of the force and energy that are related to the bond formed upon the rehybridization. Simulated dF/dZ spectra of the lifting, obtained from DFT, show qualitative agreement with the measurement.

At a molecular hydrogen (H_2) junction we observe the conversion of energy from noise into mechanical energy. Tunneling electrons lead to stochastic fluctuations between two H_2 states, each associated with a different force. The periodic oscillation of the tip modulates the stochastic noise and results in a concerted dynamics, driving the system into self-oscillation. We identified stochastic resonance as the underlying principle, allowing a directed transfer of energy from a noisy environment into directional mechanical motion.

In the charge transfer complex tetramethyltetrathiafulvalene-tetracyanoquinodimethane (TMTTF-TCNQ) we investigate the (dis)charging of TCNQ molecules by AFM. The manifestation of the (dis)charging in frequency shift-voltage ($\Delta f(V_s)$) spectra is a dip, that is associated with the (dis)charging event itself. We observe a shift of the local contact potential difference ($LCPD$) and Δf upon the change of the molecular charge state. We extract also a value for the fluctuation in the force during the dynamic discharging with the oscillating tip. Related energy dissipation cannot be observed, likely due to a too fast discharging process and no (dis)charging-induced structural changes. In $\Delta f(V_s)$ spectral maps we find indications for a mutual influence of neighboring molecules on their charge state.

Finally we investigate the zwitterionic merocyanine (MC) form of the molecular switch 1,3,3-Trimethylindolino-6'nitrobenzopyrylospiran, adsorbed in a dimer chain structure on Au(111). We can localize the intramolecular charges but find also an effective screening by the substrate and the charges of neighboring molecules. By comparison of DFT calculations and $LCPD$ maps we can also improve the structural MC dimer model. At a repulsive contact between the tip and a methyl of the molecule we observe a $LCPD$ contrast inversion, that we interpret as a reversal of the sample-probe situation: the contacted molecule becomes part of the tip and probes the surface.

Contents

Introduction

More than 63 years ago Richard Feynman envisioned new fields of science and technology on the nanoscopic scale [1]. He spoke about the possibility to store books and other kinds of information in structures of atomic dimensions and he suggested to miniaturize computers to allow faster processing speeds. Feynman explained the necessity to improve the resolution of electron microscopes in order to understand biological mechanisms, i.e. the cause of mutations or how light is converted to chemical energy. One of his visions was the construction of microscopic machines and the manipulation of single atoms: *'What would happen if we could arrange the atoms one by one the way we want them..'*.

It took 21 years from Feynman's visionary talk, until in 1981 Binnig and Rohrer developed the scanning tunneling microscope (STM) [2], and 5 more years that Binnig, Gerber and Quate presented the first atomic force microscope (AFM) [3]. With the help of these microscopes it was possible to measure up to Feynman's expectations. Nowadays STM and AFM are being used routinely as tools to image structures with atomic resolution [4–6] and to manipulate molecules and atoms into structures that in future could be used for data storage [7].

Progress in chemistry enabled the design and synthesis of molecular motors and switches, yielding molecules with functions. These motors can be driven by light, chemical energy [8, 9] or electrical energy provided by the tip of an STM [10]. Molecular switches on surfaces could controllably be converted in between their conformations by electrons, forces, electric fields, light and temperature [11–15].

As Feynman had claimed, technical progress has shown a successful trend of miniaturization. Today computers and data storage incorporate circuits and functional units, only sized tens of nanometers [16, 17]. Yet the needs for further miniaturization continues along with the rapidly advancing digitization of the world [18]. But the currently established silicon based technology is approaching a scale where physical limits of lithography and quantum effects could be reached [19, 20]. A promising candidate for future functional and efficient devices are molecular electronics. Several examples of molecular devices can be seen as a proof of concept, yet they are still far from end-user application.

In this thesis we investigated several 'functional' molecules with a comparatively new experimental method: low temperature (LT) scanning tunneling microscopy combined with dynamic atomic force microscopy implemented in the tuning fork based qPlus [21] design. It allowed us to study fundamental properties of single molecules [22–24]. The experimental setup was planned, constructed and successfully put into operation in the beginning of this thesis. In the first chapter we give a brief introduction to the theoretical background of STM/AFM and the experimental setup (chapter 1). In the following chapters 2-5 we present STM/AFM studies about four different molecular systems.

Charge transport through molecular wires is an essential field, that has to be understood on the way to molecular electronics. In chapter 2 we correlated the structural arrangement of a molecular wire, obtained from AFM and DFT, with its conductance. During the controlled lifting of a molecular wire, namely 1,4-bis(pyridin-4-ylethynyl)benzene (BPEB), with the tip of an STM/AFM from a copper surface we observed an atypical nonlinear increase in the conductance. We identified as the cause intramolecular structural changes, e.g. a rehybridization of a molecular carbon atom from sp to sp^2. The change of the hybridization led to an additional bond between molecule and copper surface, enhancing the conductance. We correlated these structural changes, expressed by nonlinearities in the conductance vs. lifting distance curve, with nonlinear changes in the stiffness obtained from AFM $\Delta f(Z)$ curves. We obtained values of the energies and forces associated with the rehybridization process from $\Delta f(Z)$ spectra.

Energy harvesting from ambient noise is a concept that could be used e.g. to power functional nanoscopic devices like nanocars or electronic circuits. In chapter 3 we investigated the conversion of noise originating from a switching hydrogen (H_2) molecule into the mechanical motion of a macroscopic oscillator. The stochastic motion of a H_2 molecule was induced by the tunneling electrons and led to fluctuations of the force acting on the tip of the tuning fork. The periodic oscillation of the tip modulated the stochastic fluctuations of the H_2 and resulted in a concerted dynamics, driving the system into self-oscillation. Stochastic resonance was identified as the underlying mechanism, allowing a directed transfer of energy from a noisy environment into periodic motion of a tuning fork oscillator.

A molecular switch is a nanoscale 'machine' which can be converted reversibly between two or more states by external stimuli. The control and determination of their states is of fundamental interest for molecular electronics. In chapter 4 we examined the interplay between periodic (dis)charging of TCNQ molecules and the dynamics of the tuning fork oscillator. The molecules exist in a neutral (anionic) charge ground state and can be (dis)charged by applying a certain sample bias at a determined tip distance, hence electric field. From $\Delta f(V_s)$ spectroscopy we could identify the charge states. The periodic discharging, caused by the oscillating tip, appeared as a dip in the Δf and allowed an estimation of the difference in force between the two charge states. The (dis)charging process was found to be free of tip-sample dissipation. We observed a mutual influence of neighboring molecules on their charge state. The discharging of neighbor molecules at higher electric fields led to the recharging of a molecule below the tip.

Molecular switches adsorbed onto surfaces do often lose their ability to change their conformation [25]. In order to understand the underlying mechanisms that block the switching, the surface induced modification of their properties must be understood. In chapter 5 we characterized the intramolecular charge distribution of the zwitterionic merocyanine form of the molecular switch 1,3,3-trimethylindolino-6'nitrobenzopyrylospiran adsorbed on a Au(111) surface. We could confirm the existence of an intramolecular dipolar distribution of charges from the 3-dimensional mapping of the molecular electrostatic potential by means of spatially resolved $\Delta f(V_s)$ spectroscopy but found also an effective screening of the molecular charges by the substrate and a mutual cancellation of opposing dipole moments due to the molecular arrangement within the dimer

chains. Furthermore our investigations led to an improved molecular structural MC dimer model. An atypical inversion of the measured electrostatic potential was found at a repulsive contact formation between molecule and tip. The last was likely caused by an effective reversal of the sample-probe system such that the molecule became part of the tip, probing the sample.

Chapter 1.

Theory and Experimental Setup

Since its development and presentation in 1981 the scanning tunneling microscope (STM) has become a quite common and valuable research instrument in modern physics but also diagnostics instrument in industry. For presenting the first working STM the physicians G. Binnig and H. Rohrer [2, 26] were honored with the Nobel prize in physics in 1986 [27].

The great advantages of scanning tunneling microscopy with respect to other surface sensitive probing methods is the displaying of real space topographic and spectroscopic information, combined with the possibility to manipulate single atoms or molecules, while other methods often (e.g. LEED) do average over bigger areas, display the reciprocal space or give only spectroscopical information.

Scanning tunneling spectroscopy and inelastic tunneling spectroscopy can yield information about e.g. the electronic structure, vibrations and spin flip processes of surfaces and adsorbates [28].

Even though the topographic resolution of STM is very high, on the sub-Å scale, it is limited to image surfaces of (constant) density of states which does not necessarily resemble the topography of the sample. Especially when imaging molecules the molecular electronic structure does not give clear information on atomic positions within a molecule. And, STM is of course limited to conducting samples.

These limitations have been overcome with the atomic force microscope (AFM), developed and first introduced by G. Binnig *et al.* in 1986 [3]. Atomic resolution could be achieved in the contact mode already in 1987 [4]. The development of non-contact atomic force microscopy (NC-AFM), based on a tip attached to a lever oscillating with its resonance frequency (therefore NC-AFM is also called dynamic (atomic) force microscopy), allowed to measure sample topography without tip or sample being modified during the scanning, and later yielded true atomic resolution on reactive surfaces under UHV conditions [29].

The introduction of stiff sensors e.g. tuning forks [6, 30] or needle sensors [31, 32] allowed very small oscillation amplitudes and the attachment of a conducting tip to the force sensor, combining the advantages of STM and AFM in one experimental setup.

In this chapter we will describe the basic principles and theory of STM and AFM (sec. 1.1,1.2) and an overview of the used low-temperature STM/AFM system will be given (sec. 1.3). We will mainly stick to the aspects that are relevant for this thesis.

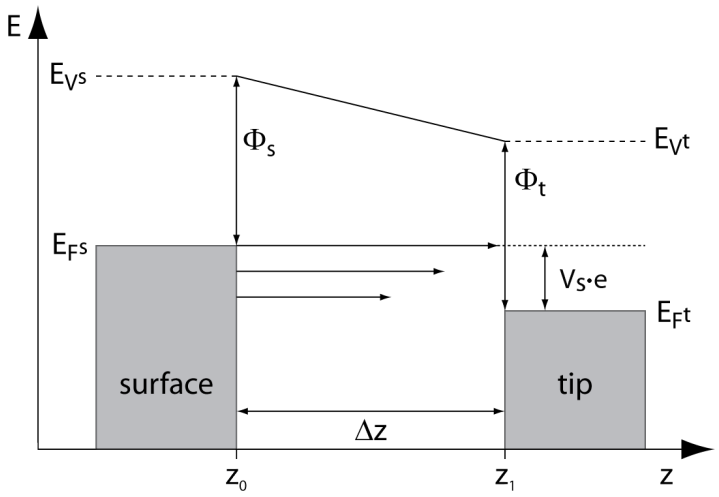

Figure 1.1.: Scheme of the tunneling through the potential barrier between surface and tip, with negative bias voltage applied to the surface. $E_{F\ s,t}$ are the Fermi levels of surface and tip, $E_{V\ s,t}$ the respective vacuum levels and $\Phi_{s,t}$ the work functions. At negative sample bias V_s, electrons tunnel from filled surface states into the tip's empty states.

1.1. Scanning Tunneling Microscopy

The basic principle behind STM is the effect of quantum tunneling. Ideally, we think of a conducting tip ending in a single atom and a conducting or semiconducting surface which are separated by a vacuum gap. The gap works now as a potential barrier. An electron, as a quantum mechanical particle, has then a finite probability to tunnel through this barrier. The tunneling probability depends on the local density of states (LDOS) of tip and surface, the electron energy, and the distance between tip and sample.

In electronic equilibrium with bias equal zero (the bias is the voltage applied to the sample with respect to the grounded tip) the tunneling current is equal in both directions and the resulting tunneling current is zero, if we assume the tip and the surface to be of the same material. With positive bias, applied with respect to the tip potential, electrons tunneling from the tip into the sample result in a positive net tunneling current. With negative sample bias, the resulting tunneling current is in the opposite direction, i.e. negative. The principle is displayed in figure 1.1, where an example for negative sample bias is shown.

1.1.1. Tunneling Theory

The simplest way to describe the tunneling process is by accounting the electron transmission through a 1D potential barrier, of width Δz and height ϕ_0. The transmission probability of a particle is given in the WKB approximation as follows [33]:

$$T(E) \approx \exp\left(-\frac{2}{\hbar}\int_{-\Delta z/2}^{+\Delta z/2}\sqrt{2m(\phi(z')-E)}\,\mathrm{d}z'\right) \text{ with } \phi(z) = \begin{cases} \phi_0 > 0 & \text{for } |z| \le \Delta z/2 \\ 0 & \text{else} \end{cases} \tag{1.1}$$

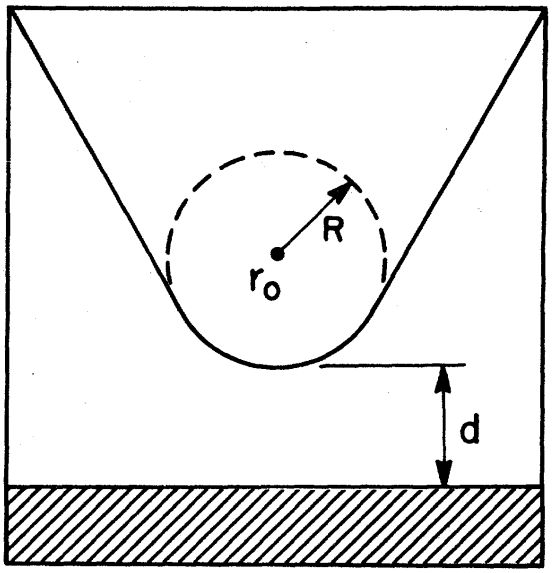

Figure 1.2.:
Image from the Tersoff and Hamann paper [37]: Schematic picture of the tunneling geometry. The probe tip is assumed to be locally spherical with a radius of R. The tip center is located at $\vec{r}_0$, the distance to the sample (shaded area) is d.

The probability to tunnel through the barrier therefore increases with decreasing particles mass m, the width of the potential barrier (Δz), and the difference between the potential height ϕ and the particles energy E (if $E \leq \phi$).

Based on the experiments of Giaever [34] and Nicol, Shapiro and Smith [35], who had observed a tunneling current flowing between two metals separated by a thin oxide layer, Bardeen [36] has shown that the transition matrix element M_{mn} between states of the probe Ψ_m and the surface Ψ_n becomes

$$M_{mn} = -\frac{\hbar^2}{2m_e} \int d\vec{S} \cdot (\Psi_m^* \nabla \Psi_n - \Psi_n \nabla \Psi_m^*). \tag{1.2}$$

The integral is over any surface lying entirely within the vacuum barrier region separating the two sides. With Bardeen's formalism the tunneling current is given, to first order, by

$$I = \frac{2\pi e}{\hbar} \sum_{m,n} f(E_m)[1 - f(E_n + eV_S)]|M_{mn}|^2 \delta(E_m - E_n). \tag{1.3}$$

where f is the Fermi-Dirac distribution, E_m and E_n the energies of the states of the two metals and V_s the applied bias voltage. Tersoff and Hamann [37] simplified the model by taking the limits of small voltage and temperature, so eq. 1.3 becomes

$$I = \frac{2\pi}{\hbar} e^2 V_s \sum_{m,n} |M_{mn}|^2 \delta(E_n - E_F)\delta(E_m - E_F) \tag{1.4}$$

where E_F is the Fermi energy.

To evaluate the matrix M_{mn} (1.2), Tersoff and Hamann expanded the surface wave function in the way that parallel to the surface it is consistent with Bloch's theorem and

perpendicular it is decaying exponentially into the vacuum. The tip was modeled as a locally spherical potential well in the way displayed in figure 1.2. The wave functions of the tip were chosen to have an asymptotic spherical form. For simplicity they assumed the work function Φ of the tip to be equal to that of the surface.

Finally the tunneling current becomes

$$I = 32\pi^3\hbar^{-1}e^2V_s\Phi^2D_t(E_F)R^2\kappa^{-4}e^{2\kappa R} \times \sum_n |\Psi_n(\vec{r}_0)|^2\delta(E_n - E_F) \tag{1.5}$$

where $D_T(E_F)$ is the density of states per unit volume of the tip, and $\kappa = \sqrt{2m\Phi}/\hbar$ the minimum inverse decay length for the wave functions in vacuum. The final simplified expression for the tunneling current comes to

$$I \propto V_s\rho_t(E_F)\rho_s(E_F, \vec{r}_0) \tag{1.6}$$

where $\rho_s(E_F, \vec{r}_0)$ is the local density of states at the surface at Fermi energy and $\rho_t(E_F)$ the LDOS at the tip. So does scanning tunneling microscopy at low bias represent the local density of states.

Image Acquisition

Imaging is a fundamental part in scanning tunneling microscopy experiments. The constant current mode is mainly used in scanning tunneling microscopy imaging. In this mode, a feedback controller with a proportional and an integral component compares the actual tunneling current with the set-point current, and adjusts the tip height to keep the tunneling current constant. By recording the height information, one gets a topographic image of the surface. Since the electronic structure of the substrate has also an influence on the tunneling current, the obtained image is always a convolution of the electronic structure and the topography but also the structure of the tip.

Another way to obtain STM images is to scan over the surface and measure the tunneling current. This imaging mode is called constant height mode. The method involves the risk to crash the tip into the sample, so it is usually used on smaller, flat sample areas. It is often used for spectroscopic imaging, where simultaneously differential conductance or frequency shift (in a combined STM/AFM setup) are measured.

1.1.2. STS: Tunneling Spectroscopy

Scanning tunneling spectroscopy is a way to investigate the electronic structure of metal substrates and adsorbed molecules. From the three parameters, tunneling current (I_t), bias voltage (V_s) and tip-sample distance (z), in STS one parameter is measured in dependence of a second one while the third one is kept constant. The most used combination is to measure the tunneling current by applying a bias voltage ramp at a fixed z to obtain a current-voltage characteristic. Using a lock-in amplifier, one can directly measure the differential tunneling conductance $\mathrm{d}I_t(V_s)/\,\mathrm{d}V_s$ [38]:

$$\frac{\mathrm{d}I_t(V_s,x,y)}{\mathrm{d}V_s} \propto \rho_s(E = e \cdot V_s, x, y). \tag{1.7}$$

This means the tunneling conductance is proportional to the samples LDOS at a certain point (x, y) of the sample at the energy $E = e \cdot V_s$. Equation 1.7 is only valid for small voltages. For higher bias voltages applied, the transmission coefficient with a bias dependent exponential growth has to be taken into account [38].

By measuring a topography image very slowly, one can modulate the applied bias voltage and measure the derivative of the tunneling current in every image point. This gives than a conductance map of the scanned region at a certain energy $e \cdot V_s$. These maps are called $\mathrm{d}I_t/\,\mathrm{d}V_s$ maps.

Another spectroscopy mode is the so called $z(V_s)$. By applying a bias ramp, the feedback adjusts the tip-sample distance z to keep the tunneling current constant at its setpoint. The derivative of the tunneling current can be also measured with a lock-in amplifier. This method has the advantage that adsorbates being sensitive to high tunneling currents may not be harmed. On the other hand, the tunneling current increases exponentially with decreasing tip-sample distance, resulting in an apparent higher LDOS at low bias voltages. This fact inhibits that this spectroscopy method can be used at low bias voltages.

1.2. Dynamic Atomic Force Microscopy

The extension of a pure STM to a tuning fork (TF) based dynamic AFM is from the technical side a not too complicated modification. But from the physical properties one can measure additionally it is a big change. The physical properties measured by dynamic atomic force microscopy are frequency shift (Δf), the oscillation amplitude (A_0) and the driving amplitude (A_D).

An illustration shows the significant properties in figure 1.3. In this model the tip is described as an effective mass m, attached to a spring with a stiffness k_0 ($k_0 = 1800$ N/m for tuning forks used in this thesis). The effective mass is given by the tuning fork's prong mass and the mass of tip and glue. Typical resonance frequencies of TFs used here are $f_0 = 18 - 30$ kHz. The frequency shift is the change $\Delta f = f_0 - f\prime$ of the resonance due to tip-sample interactions. The oscillation amplitude can be controlled to be as small as $A_0 = 0.1$ Å. This means during its oscillation cycle the tip can stay in the tunneling regime. This makes simultaneous measurement of tunneling current and Δf on the atomic scale possible. Alike the tunneling current in STM, the frequency shift can be used as a feedback signal in AFM, to obtain topography images of surfaces of constant force gradient. Due to the faster feedback, we used the STM for topography imaging.

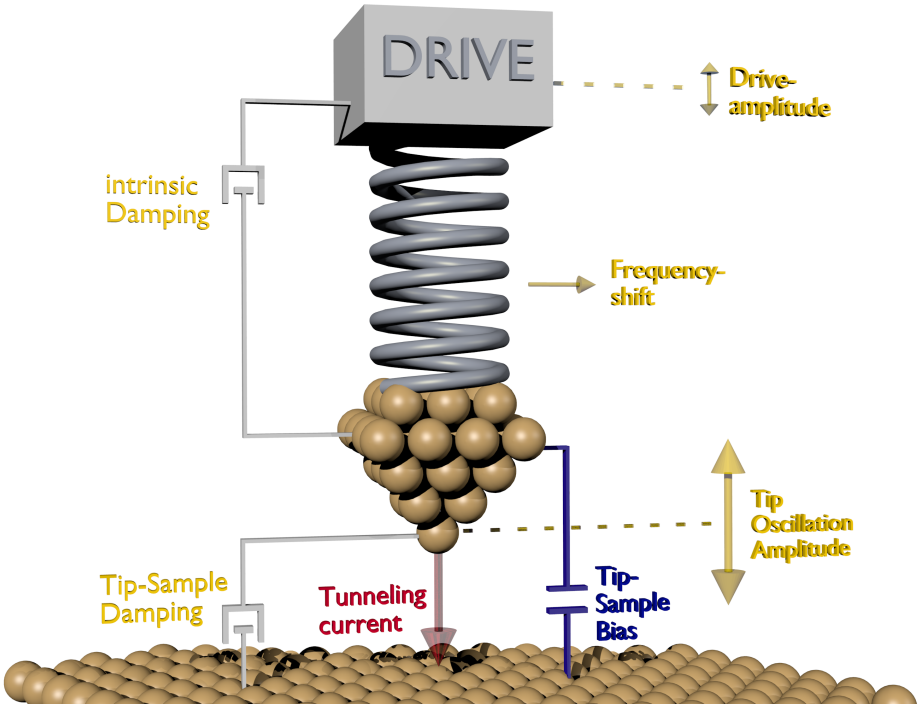

Figure 1.3.: Scheme of dynamic STM-AFM. The yellow labels correspond to observables in the AFM part in the setup. Additional AFM oscillator properties, not shown here, are the intrinsic stiffness of the (tuning fork) spring k_0 and its effective mass m, related to the oscillator resonance frequency as $f_0 = 1/2\pi \cdot (k_0/m)^{(1/2)}$.

1.2.1. The AFM: A Harmonic Oscillator

The free tuning fork is a real oscillator, which means it has some intrinsic damping due to friction. The equation of motion of the driven, damped harmonic oscillator is [39]:

$$m\ddot{x} - \frac{m\omega_0}{Q}\dot{x} + k_0 x = F_D cos(\omega t) \tag{1.8}$$

where k_0 is the spring constant of the oscillator, $\omega_0 = 2\pi f_0$ the resonance frequency with the relation $\omega_0^2 = k_0/m$, Q the quality factor which is related to the damping constant by $2\gamma = \omega_0/Q$ and $F_D = k \cdot A_D$ the amplitude of a periodic driving force with a driving frequency ω and A_D the amplitude of the driving motion.

The solution leads to the amplitude as a function of the driving frequency:

$$A(\omega) = \frac{k_0}{m}\frac{A_D}{\sqrt{4\gamma^2\omega_0^2 + (\omega_0^2 - \omega^2)^2}} \tag{1.9}$$

which is the resonance curve.

For $\omega = \omega_0$ the oscillator is in resonance. Equation 1.9 becomes then simply

$$A(\omega_0) = A_D \cdot Q \tag{1.10}$$

A close approximation of the Quality factor can be extracted from the full width of the resonance curve at $A_Q = A_0/\sqrt{2}$ with $Q = f_0/\Delta f(A_Q)$.

1.2.2. Oscillator in a Force Field: Force Spectroscopy

When the tip of the dynamic force microscope is brought closer to the sample, it is affected by the tip sample forces. Due to the oscillation in the distance-dependent force field, the force gradient causes a change of the effective stiffness of the TF oscillator. The oscillator is de-tuned to a new resonance frequency

$$f' = \sqrt{\frac{k_0 - \frac{\partial F_{TS}(z)}{\partial z}}{m}} \tag{1.11}$$

where $F_{TS}(z)$ is the tip-sample force and $f' = f_0 + \Delta f$ the resonance frequency of the detuned oscillator.

For small oscillation amplitudes, the frequency shift, which is the main observable in dynamic AFM, can be expressed as [21]:

$$\Delta f(z) = -\frac{f_0}{2k_0}\frac{\partial F_{TS}}{\partial z} \tag{1.12}$$

which means that the frequency shift is directly proportional to the tip-sample force gradient. In experiments, we are interested in interaction forces and energies between tip and sample. Therefore we perform $\Delta f(z)$ spectroscopy. If one measures the frequency shift as a function of the tip-sample distance, one can get the tip-sample force by an integration along the z axis:

$$F(z) := -\int_{z_0}^{z_1} \Delta f(z)\,\mathrm{d}z + F_{const} \tag{1.13}$$

where we define negative forces as being attractive.

However, in cases where the oscillation amplitudes are larger or the $\Delta f(z)$ features observed are in the order of the oscillation amplitude, the previous approximation gives inaccurate results. Franz Giessibl derived a more general expression for the frequency shift from first order perturbation theory with the Hamilton-Jacobi approach [40]:

$$\frac{\Delta f}{f_0} = \frac{1}{\pi A_0 k_0}\int_{-1}^{1} F(x + a(1+u))\frac{u}{\sqrt{1-u^2}}\mathrm{d}u \tag{1.14}$$

where x is the distance of closest tip approach between tip and sample during the oscillation. Sader and Jarvis developed from this a deconvolution method to yield the exact forces from $\Delta f(z)$ independent of the amplitude: [41]

$$F(z) = \frac{2k_0}{f_0}\int_z^{\infty}\left(1 + \frac{a^{1/2}}{8\sqrt{\pi(t-z)}}\right)\Delta f(t) - \frac{a^{3/2}}{\sqrt{2(t-z)}}\frac{\Delta f(t)}{dt}\mathrm{d}t \tag{1.15}$$

It is possible by further integration along z to obtain the potential energy as a function of the distance.

All these methods can only be applied within elastic regimes of tip-sample interaction. If plastic changes occur in the junction, the elastic regimes have to be treated separately and the obtained forces are values, each relative to the point after the last plastic deformation.

1.2.3. Dissipation in Atomic Force Microscopy

The equations from Sader and Jarvis are only valid for constant oscillation amplitudes. However, in real experiments the tip-sample interactions may be non-conservative, e.g. upon repeated bond-formation and bond-breaking during the dynamic tip motion. Then the damping constant - or the effective quality factor Q_{eff} - would change, which would influence the oscillation amplitude (eq. 1.10) as

$$A(f_0) = A_D \cdot Q_{eff} = A_D \cdot \left(Q - \frac{\pi f_o}{\gamma_{TS}} \right) \tag{1.16}$$

where γ_{TS} is the damping constant of the dissipative tip-sample interaction.

In order to keep the oscillation amplitude constant, an amplitude feedback controller adjusts the driving amplitude so that the oscillation amplitude is kept constant. This solution has an additional benefit as it allows to measure and quantify the dissipation. We calibrate therefore each qPlus sensor far away from the sample to determine its quality factor Q and the driving amplitude A_D of the free tuning fork, required to maintain a constant oscillation amplitude A_{osc}. In the experiment we measure the actual (constant) oscillation amplitude A_0 of the tuning fork and the actual driving amplitude A'_{drive} required to maintain the oscillation amplitude A_0 constant. With the energy stored in the motion of the oscillating cantilever, $E_0 = k/2 \cdot A_0^2$, one gets for the energy dissipated per oscillation cycle of the free tuning fork due to intrinsic damping:

$$D_0 = \frac{2\pi E_0}{Q} \tag{1.17}$$

for which the driving amplitude A_D is known. Then the energy dissipated per oscillation cycle due to tip-sample interactions becomes a simple linear relation [21]:

$$D_{TS} = D_0 \left(\frac{A'_D}{A_D} - 1 \right) \tag{1.18}$$

For a typical cantilever with $f_0 = 20$ kHz, $Q = 10000$ and $k = 1800$ N/m and an oscillation amplitude of $A_0 = 50$ pm one gets for the free tuning fork an energy of $E_0 = 21.2$ eV stored in the motion of the tuning fork and an intrinsic energy dissipation of $D_0 = 13$ meV each oscillation. This enables us to resolve dissipation effects in the order of millielectronvolts per oscillation cycle.

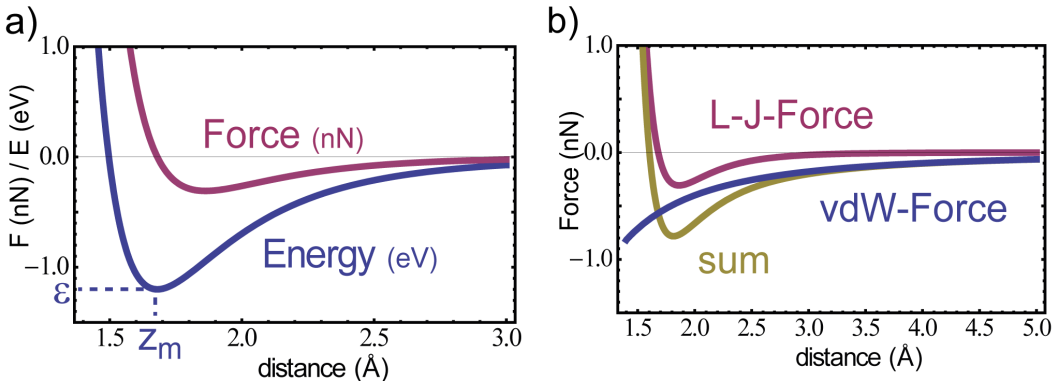

Figure 1.4.: a) Modeled Lennard-Jones potential (blue) and the derived Lennard-Jones force as a function of the distance of two atoms. z_m and ϵ denote the bond distance and the binding energy, respectively. **b)** Lennard-Jones force from a) and modeled van der Waals force (blue, Hamaker approach) and the sum of both (yellow).

1.2.4. Forces in Atomic Force Microscopy

Here we will discuss the different forces that play a role in AFM. These are the chemical forces, the van der Waals (vdW) force, electrostatic and magnetic forces. The last are usually very weak in comparison to the other forces and require magnetic tips and samples and, depending on the experiment, even external magnetic field to detect them. Since they do not play a role in our experiments they will not be discussed here.

Chemical Forces

Chemical forces are short range forces, which become significant at distances between tip and sample, where their wave functions overlap - this is the case at distances where tunneling currents can be observed. They are the only relevant forces with repulsive components. Chemical forces are often modeled by the Lennard-Jones(12,6) potential [42], which describes the potential energy as a function of the distance of two atoms:

$$E_{LJ}(z) = \epsilon \left(\left(\frac{z_m}{z} \right)^{12} - 2 \left(\frac{z_m}{z} \right)^{6} \right) \tag{1.19}$$

where ϵ is the depth of the potential at the distance z_m, so ϵ is the binding energy while z_m is the binding distance of the two involved atoms. A Lennard-Jones potential with parameters $\epsilon = -1.2$ eV and $z_m = 1.68$ Å is plotted in figure 1.4 a).

The $()^{12}$ term holds the repulsive part of the forces. They act only on very short distances. Physical origin is the Pauli repulsion: if two atoms are brought close together their filled orbitals will start to overlap. But due to the Pauli principle two electrons may not occupy the same quantum state simultaneously. So electrons are forced to occupy higher lying orbitals, which lets the energy of the system increase and, hence, leads to repulsion.

The $()^6$ term holds the attractive part of the forces which arise from van der Waals forces, but also permanent dipole-dipole interactions. This holds only for the case of single atoms - the idealized situation of a tip probing a molecule after removing the long range background forces. VdW forces are treated later separately, too. They are small for single atoms but they become large if many atoms are involved since vdW forces are of longer range than the repulsive forces and additive.

Differentiation of the Lennard-Jones potential in z-direction yields the chemical force as a function of the distance.

$$F_{LJ}(z) = -\frac{\partial E_{LJ}(z)}{\partial z} = 12\frac{\epsilon}{z_m}\left(\left(\frac{z_m}{z}\right)^{13} - \left(\frac{z_m}{z}\right)^{7}\right) \tag{1.20}$$

The Lennard-Jones potential derived force is plotted in fig. 1.4 a) together with the potential energy.

van der Waals Forces

The van der Waals (vdW) force originates from dipole interactions between molecules and atoms. They include forces between two permanent dipoles (Keesom force), permanent dipole and a corresponding induced dipole (Debye force) and the London dispersive forces, which are instantaneously induced dipoles [43].

The vdW potential for two atoms $E_{vdW} \propto -1/z^6$ is part of the chemical potential as it is of relative short range and weak. But due to its additive character it plays a role on macroscopic objects. In AFM experiments, where we want to observe the forces between atomic scale objects, e.g. the tip and molecules or atoms, the long range vdW forces due to the macroscopic tip can become significant.

For the case of a sphere of radius R at distance z from an infinite plane the approach by Hamaker [44] yields the van der Waals force:

$$F_{vdW}(z) = -\frac{HR}{6z^2} \tag{1.21}$$

where H is the material dependent Hamaker constant. Figure 1.4 b) shows the vdW force as a function of the distance for a sphere with radius $R = 20$ Å and a Hamaker constant $H = 3$ eV together with the Lennard-Jones force and their sum. As one can see, the vdW force gives a large attractive background. Larger vdW forces shift the minimum in the curve *sum* (figure 1.4 b) to smaller z distances. Another experimental problem is that the attractive forces can become so strong that tip may me pulled into contact.

So it is even more crucial to have a very sharp tip on a longer z scale (compared to STM, which requires only an atomically sharp apex). In order to interpret the interaction between the front atom of the tip and a sample from $\Delta f(z)$ spectra, independent of the macroscopic tip shape, a background correction can become necessary. Reference spectra taken on the substrate and subtracted from the spectra taken in the region of interest yield only the short range interaction between the very front of the tip and the region of interest [22, 24, 45].

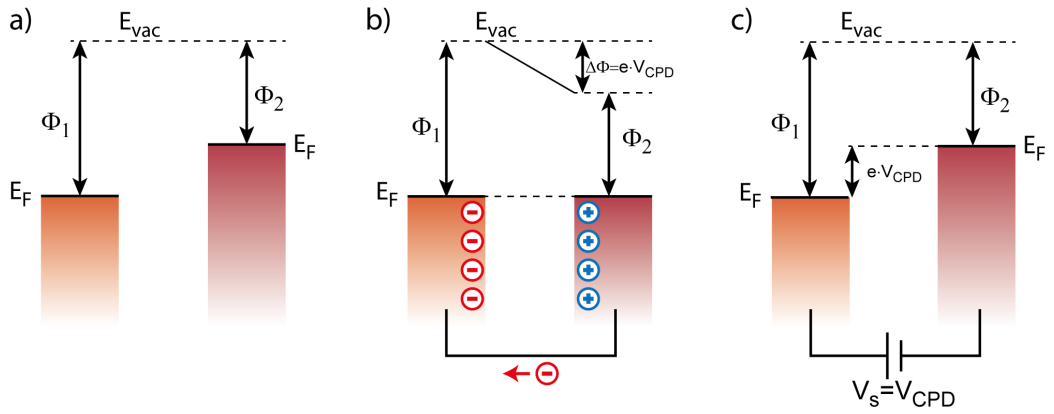

Figure 1.5.: Sketch: Origin of the contact potential difference (CPD). **a)** When two materials with different work functions Φ_i are in no electrical contact their vacuum levels are aligned. **b)** When the materials are electrically connected, their Fermi levels E_F align by electrons flowing into the metal with higher work function. This leads to a potential difference $CPD = \Delta\Phi/e$. **c)** The potential difference - and so the electrostatic forces - between both materials can be minimized if an external bias voltage $V_s = CPD$ is applied.

Electrostatic Forces

Electrostatic forces are from these three forces the ones with the longest range. They can occur by a potential difference between metallic tip and sample. In a simplified way tip and sample can be treated as a capacitor. The electrostatic force of a capacitor is given by [46]:

$$F_{el} = -\frac{\partial E_{cap}}{\partial z} = \frac{1}{2}\frac{\partial C}{\partial z}V^2 \tag{1.22}$$

where E_{cap} is the energy stored in a capacitor with capacitance C. In a capacitor formed by two different surfaces, e.g. the tip of an AFM and the substrate, the effective electrostatic potential is $V = V_s - CPD$. In an experimental setup is V_s an externally applied voltage and CPD the so called contact potential difference corresponding to the difference in the work functions of tip and sample. The function in eq. 1.22 is a parabolic curve and thus CPD corresponds to the voltage value where the absolute value of the force has a minimum. By applying an external bias so that $V_s = CPD$ the contact potential difference is compensated and the electrostatic forces are minimized. This method allows to determine the CPD experimentally, which will be discussed in detail in the next sections.

1.2.5. Kelvin Probe Force Microscopy

If two metals with different work function $\Phi_{1,2}$ are separated, their vacuum levels are aligned as shown in fig. 1.5 a). When they are brought into electrical contact their Fermi

levels will align. Therefore electrons will flow from the metal with lower work function $|\Phi_2|$ into the one with higher $|\Phi_1|$. The charges will accumulate on the surface, resulting in a space charge. Their electric field pushes the electrons back, until an equilibrium is reached (fig. 1.5 b). In equilibrium, the separated space charges yield a potential difference, the so called *contact potential difference* (CPD) that is given by $CPD = (\Phi_2 - \Phi_1)/e$ [46].

A method to measure the contact potential difference has already been developed by Lord Kelvin in 1898 [47], called Kelvin probe method. Here sample and probe are the two plates of a capacitor. An AC current is induced by an AC distance displacement of the two plates due to the difference in the work functions. This AC current can be nullified by applying an external DC voltage $V_{DC} = CPD$ and yields the work function difference $\Delta\Phi = e \cdot CPD$.

This method could be extended to yield lateral resolution on the sub-nanometer scale by a modified dynamic AFM setup, the so called Kelvin Probe Force Microscopy (KPFM) [48, 49]. The (DC) bias voltage is modulated with an AC voltage. If the DC component is not equal to the CPD, the AFM will be excited also at the modulation frequency and oscillate with a certain amplitude. Lock-in technique and a feedback on the DC bias can be used to keep the AC amplitude minimal. This method can be applied while scanning an image in AFM feedback, yielding a map of laterally resolved CPD.

1.2.6. Local Contact Potential Difference

The latest great advances in KPFM were achieved by Gross *et al.* in 2009 [23] using a qPlus [21] design dynamic force microscope. Due to the high stiffness of the tuning fork sensor, the oscillation amplitudes can be as small as 10 pm. This allows much closer (time-averaged) tip-sample distances and therefore a much higher resolution: Gross *et al.* could determine the charge state of single Au and Ag atoms adsorbed on a NaCl layer on Cu(111).

In this method the tip is positioned over the sample at a fixed (average) tip-sample distance. Then the bias voltage is ramped while the frequency shift is recorded. The capacitor approach eq. 1.22 yields then for the measured force gradient at $\bar{z} = const$.

$$\Delta f(V_s) \propto -\frac{\partial F_{el}}{\partial \bar{z}} = -\frac{1}{2}\frac{\partial^2 C}{\partial \bar{z}^2}(V_s - LCPD)^2 + \Delta f(\bar{z}). \tag{1.23}$$

The $\Delta f(V_s)$ curve is a parabola, centered at the value $LCPD$, the *local* contact potential difference, like in eq. 1.22. The prefactor on the right hand side, before the brackets, is reflected in the curvature of the parabola and is due to the distance-dependent capacitance of the junction. One has to account for other forces, e.g. van der Waals force and chemical forces, by an offset $\Delta f(\bar{z})$. The frequency shift value at $LCPD$ thus is due to all forces apart from (vanishing) electrostatic forces.

This method is relative slow, as it requires to measure a whole parabola at any point of interest on the sample (and fit every single spectrum with a parabolic function to extract $LCPD$ and $\Delta f(V_s = LCPD)$). But it has shown to yield very high lateral resolution, even on small variations of the local contact potential difference [50, 51].

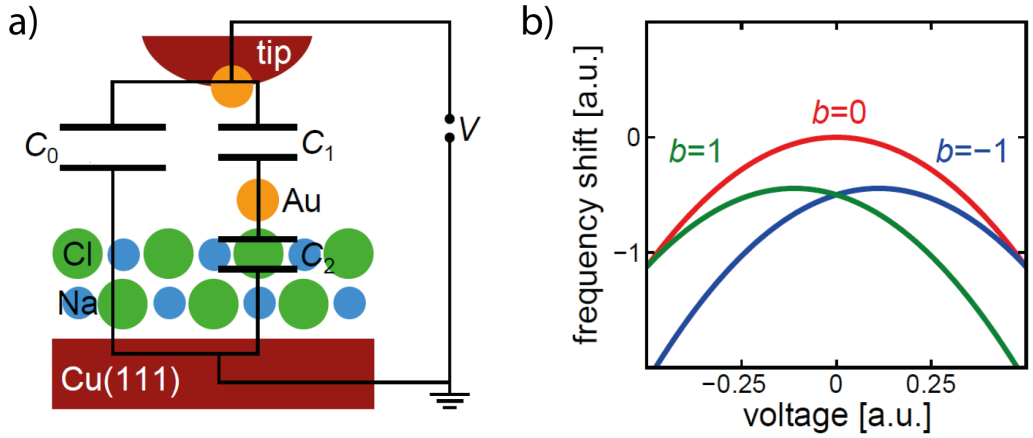

Figure 1.6.: Electrostatic model for a double-barrier tunnel junction, from [51]. **a)** Schematic illustration of tip, sample and an Au adatom on an insulating NaCl layer and equivalent circuit of the electrostatic model. $C_0(z)$, $C_1(z)$ and C_2 denote the tip-substrate capacitance, the tip-adatom capacitance and the adatom-substrate capacitance, respectively. **b)** The function $\Delta f(V) = a(b+V)^2 + cV^2$ in the model a) plotted for different values of b, which correspond to negative (blue), positive (green) or no charge (red). non-vanishing values of b, since independent of V, cause both a vertical and a lateral shift of the parabola. The b is attributed to an image charge, induced in the AFM tip.

Force Between a Metallic Tip and a Charged Atom

Gross *et al.* observed a vertical shift of the $\Delta f(V_s)$ parabola $LCPD$ to more negative Δf values (and hence more attractive force) when measured with the metallic AFM tip above a charged atom in comparison to a neutral atom [23, 51]. The shift occurred for both, positive and negatively charged atoms. They attributed this due to an additional term in eq. 1.23, originating from a polarizable tip. The double barrier tunneling junction (DBTJ) of their experimental setup, sketched in figure 1.6 a) (from [51]), can be modeled with an electrostatic force

$$F_z(V) = \frac{1}{2C_\Sigma^2}\frac{\partial C_1}{\partial z}(q + C_2 V)^2 + \frac{1}{2}\frac{\partial C_0}{\partial z}V^2 \tag{1.24}$$

where $C_0(z)$, $C_1(z)$ and C_2 denote the tip-substrate capacitance, the tip-adatom capacitance and the adatom-substrate capacitance, respectively and $C_\Sigma(z) = C_1(z) + C_2$. The first term on the right hand side of eq. 1.24 is independent of V and can be attributed to an image charge induced in the AFM tip. In previous studies it was argued that this term can be neglected due to the experimental conditions in KPFM, e.g. large oscillation amplitudes and, hence, large (average) tip-sample distances [52, 53]. This assumption is not valid for the small oscillation amplitudes and small tip-sample distances used in the tuning fork AFM setup. The frequency shift parabola is then of the form

$$\Delta f(V) = a(b+V)^2 + cV^2 \tag{1.25}$$

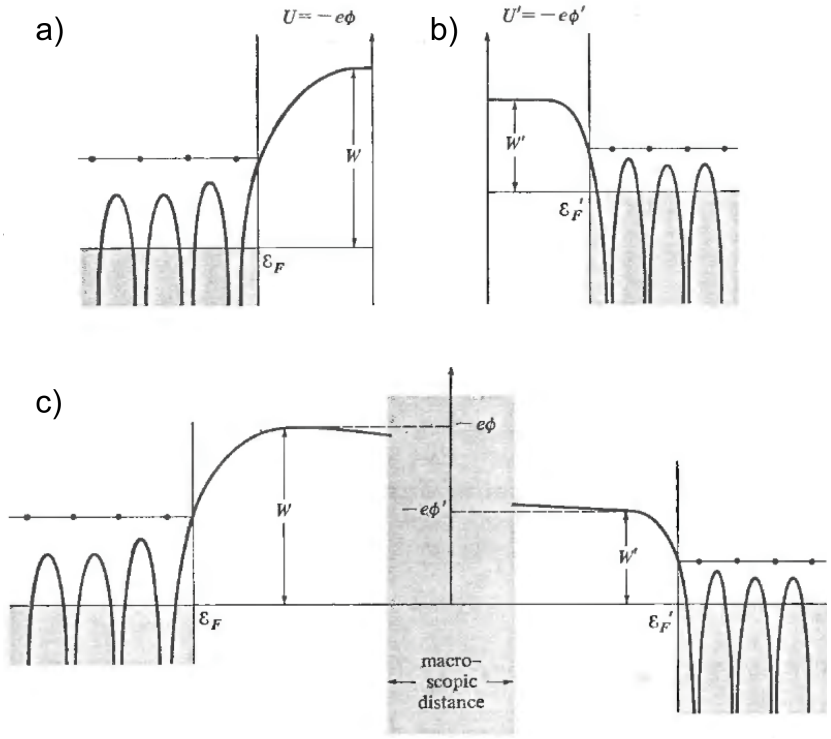

Figure 1.7.: (a) and **(b)** show the crystal potential U (or electrostatic potential $V = U/-e$) for two separate metals with work function W and W' and Fermi energy ϵ_F and ϵ_F', respectively. **(c)** In electrical contact, the Fermi levels of the two metals align, analogous to figure 1.5. On a macroscopic distance between the two metals, the potential drops linearly over the gap. At closer distances of the two metal surfaces, in the order of their lattice constants, the potential evolves more complicated. The potential vacuum level values $U = e\phi$ with respect to the Fermi level may not be reached, thus a (constant) work function is not defined any more. Figure is taken from [54].

where b accounts for the non-vanishing term due to the image charge induced in the AFM tip. Gross and Mohn showed (figure 1.6 b) that this model can indeed account for their observed shift of the $\Delta f(V_s)$ parabola $LCPD$ to more negative values on charged atoms [23, 51]. However, the general relation, that the parabola minimum $|\Delta f|$ shifts to negative (positive) $LCPD$ values if a surface charge q is positive (negative), remains valid. Due to the strong distance dependence of chemical forces, the effect of the vertical Δf shift will be difficult to distinguish if topographic effects are involved.

1.2.7. From Electrostatic Potential to Work Function

With the tip being in tunneling distance, variations in the contact potential difference could be resolved, which cannot be equalized with the concept of work function, anymore. The work function is a macroscopically defined property and reflects the long range approximation of the surface electrostatic potential. Far from the surface - in re-

lation to the lattice constant - one can assume that the surface is uniformly charged per unit area. With a second surface - the tip - parallel to the first one, this can be modeled as a capacitor. Inside a model capacitor the potential drops linear over the whole distance between the two surfaces, thus the potential difference at a given constant charge density will be constant at any distance z between the surfaces. These conditions are met in a typical cantilever AFM setup, where the tip amplitudes are in the order of ≥ 1 nm. Then the equilibrium tip distance is sufficiently far away from the surface, and one can indeed measure spatial variations of the work function.

In contrast to the model figure 1.5, which is typically presented to explain Kelvin probe force microscopy, the real situation close to the surface is much more complex. Figure 1.7 a) and b) (from [54]) show the crystal potential of two separate metals with different work function W, W' and different Fermi level ϵ_F and ϵ'_F, respectively. Within the bulk of a metal crystal the periodicity of the atoms causes a lattice-periodic potential, usually described by Bloch functions [55]. At the surface the crystal symmetry is broken, and a charge redistribution occurs. This leads to an effective surface dipole and causes, what we call work function.

But the evolution of the potential from the bulk into the vacuum can not be a step function as in the sketch in figure 1.5, but has to be continuous. For different surfaces, different potentials apply, for instance on ionic surfaces, where opposite charges in the surface are next to each other, the potential decays exponentially [56]. In metals, electrons are screened by an image charge and the potential is in its simplest approximation of the Coulomb form $V(z) \propto 1/z$ [57, 58]. The surface potentials decay within a few Å into the vacuum, this distance electrons have to travel, to escape the surface potential. Tuning fork based AFM with its small oscillation amplitudes does allow to approach the tip so close to the surface, that in the picture fig. 1.7 c) the surfaces would be so close to each other, that the potentials could not reach the vacuum level values $U = e\phi$ with respect to the Fermi level. Then the potential difference between tip and sample does no longer reflect the difference in the work function between tip and sample. What $LCPD$ in this case means is the local electrostatic potential.

Therefore we will not refer to the work function in our experiments, but rather speak of the local contact potential difference (LCPD) or (local) electrostatic potential.

1.3. Experimental Setup

The experiments presented in this work were performed in a low temperature STM/AFM chamber based on the design of Gerhard Meyer and SPS-Createc GmbH [59, 60]. The design and construction of the base chamber, as well as the design and installation of the typical ultrahigh vacuum, sample preparation and transfer tools was part of this thesis. The cryostat with the STM/AFM head was bought and installed by SPS-Createc GmbH. STM/AFM controller electronics were provided by SPS-Createc, as well. For controlling the AFM an additional phase locked loop (PLL) controller from SPECS-Nanonis was bought and incorporated into the setup [61]. For improving the performance of the STM/AFM further modifications were made, e.g. additional filtering and cooling wires. In the following a detailed description of the setup will be given.

1.3.1. UHV Chamber

The chamber design was developed from experience, collected within the group with the present low temperature scanning tunneling microscopes. A photograph of the whole machine is shown in fig. 1.8 a). The inset shows our final CAD drawing of the base chamber, as we ordered it from VAb GmbH [62], mounted on the frame with load-lock and turbo pump chamber. The base chamber consists of a preparation chamber and a SPM chamber. Both are separated by a gate valve. This allows sample preparation without contamination of the SPM chamber by molecules or sputter gas. It is also possible to perform a preparation chamber bakeout, while the SPM chamber remains cold at cryogenic temperatures.

Sample transfer between the microscope and the preparation chamber is accomplished with a rotatable linear manipulator. The standard metal-sample holder incorporates a direct current oven heater, on which the samples are mounted. A k-type thermocouple is attached to the samples on the sample holder. The manipulator is coolable with liquid helium. During sample preparation the sample temperature can be controlled over a wide range from 100 K to $\sim$ 900 K. This allows all preparation steps, e.g. sputtering, annealing and molecule evaporation to be done with the sample held in the manipulator at the desired temperature.

A major requirement was the possibility to prepare atomically clean surfaces and the evaporation of molecules. Therefore standard preparation tools and equipment as well as several special modifications were incorporated into the chamber:

- two load-lock/evaporator ports, connected through bypass tubes to the
- turbo pump chamber, to attach molecule or metal evaporators, sample holder and tuning fork sensor transfer tools without breaking the vacuum of the preparation chamber
- the preparation chamber is equipped with
  - quadrupole mass spectrometer for (residual) gas analysis

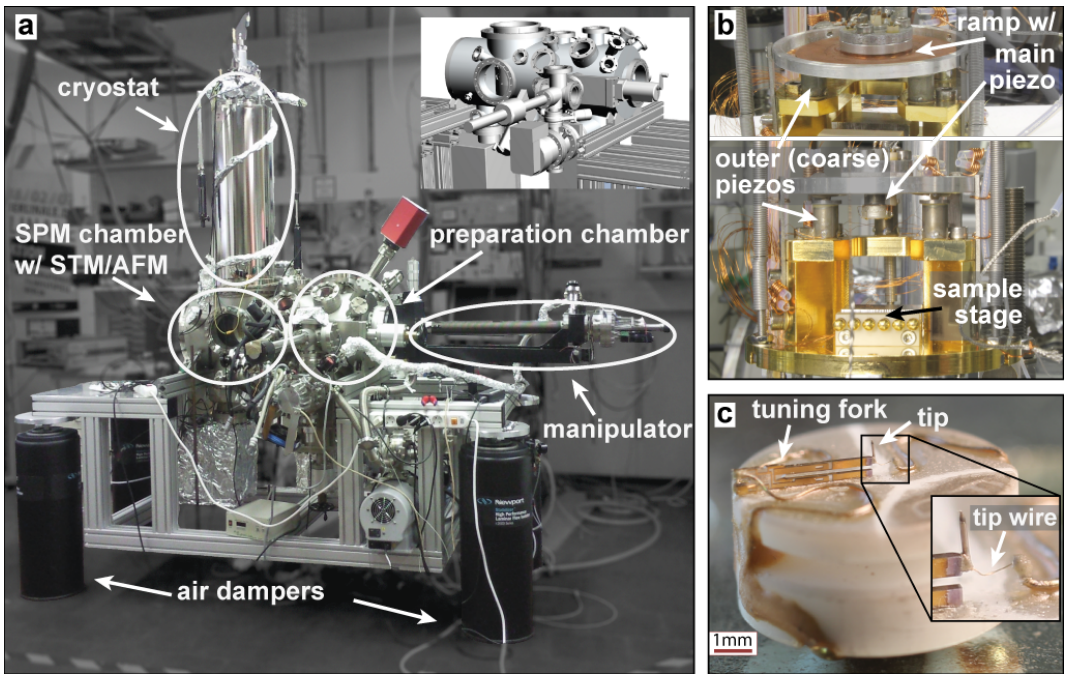

Figure 1.8.: SPM system constructed and used in this thesis. **a)** Photograph of the LT UHV STM/AFM chamber. The inset shows the CAD drawing of the base chamber, load-lock and frame. **b)** SPM head from different perspectives. Lower: View into the microscope from the sample transfer side. A sample can be placed on the sample stage. By un-clamping the SPM head, a spring presses the sample stage and sample up against the base plate, which holds the outer coarse piezos. These carry the ramp; in the ramp center is the central piezo, onto which the tuning fork sensor sticks, held by magnets. Rotation of the ramp moves the central piezo and the sensor with tip perpendicular to the sample surface. The upper figure of b) shows the ramp top - lateral translation is possible within the area of the aluminium ring, mounted around the ramp. **c)** Tuning fork dynamic force sensor. The tuning fork is glued with one prong to the sensor holder and a tungsten tip attached to the free prong. The inset shows a magnification of the 12μm gold tip wire. It decouples the tunneling current from the piezoelectric AC current of the oscillating tuning fork.

  - leak valves for gas dosing and
  - sputter ion gun for sample cleaning
  - sample parking with space for four sample holders and a special parking for tuning fork sensor transfer tools

- ionization gauges to monitor the pressure
- ion pumps and a titan sublimation pump maintain mechanical vibration free ultra high vacuum
- air damper feet decrease the mechanical coupling between building and the instrument

1.3.2. LT SPM Head

The SPM head was delivered and mounted by SPS-Createc GmbH together with the cryostat and radiation shields [60]. The construction of the head, developed by Dr. Gerhard Meyer and Dr. Sven Zöphel in the group of Prof. K.-H. Rieder at the FU Berlin, follows the Besocke beetle type [63] design. Although the design is relative simple, it delivers high mechanical and thermal stability and can be operated in a temperature range from 4.5 K to 300 K.

Figure (1.8 b) shows a photograph of the SPM head. In this setup the sample holder with sample is clamped against a baseplate, on which three so called coarse piezos are mounted. These have each a sapphire sphere mounted on top, holding a threefold ramp made from copper. By applying sawtooth voltage pulses to certain electrodes of the piezos the ramp does a rotational motion around its center. The lift height is 0.6 mm. An aluminium ring around the ramp allows lateral motion, covering a major part of the sample, but also protects the ramp from falling off the piezo-sapphires.

In its center the ramp holds the central piezo. It bears the tuning fork sensor with two magnets and makes three electrical contacts to the sensor: two for the tuning fork piezoelectric AC current and one for the tunneling current. The excitation of the tuning fork motion is done mechanically by applying an AC voltage to the central piezo. A sensor, like it is used in the SPM, is shown in a photograph in figure (1.8 c). The tuning forks are standard commercially available 32.768 kHz quartzes like they are being used in e.g. wristwatches. They are mounted on a Macor [64] base with one prong fixed with glue while the other prong remains free to oscillate normal to the sample surface.

An important feature when working with tuning fork sensors is the easy *in situ* sensor transfer while the SPM head stays at low temperatures. This is possible due to the magnet mount: two opposite oriented magnets each, in the sensor holder and in the central piezo, define the sensor orientation. Gold coated spheres - visible in the mirror image in the bottom right of fig. 1.8 c) - make the electrical contacts to counter electrodes at the bottom of the central piezo. A cut-out in the sensor holder allows sensor transfer with a special designed fork-like tool which can be held in the manipulator.

Sample holders and tuning fork sensors design were developed by Gerhard Meyer and Sven Zöphel; during this thesis newly constructed sensors and sample holders follow these designs.

Start-Up: The First Results

Shortly after the final assembly, the microscope could be put into operation. Figure 1.9 a) shows one of the first images with atomic resolution on a Au(111) surface. It is unprocessed and exhibits a low noise level, confirming optimal conditions. Afterwards a tuning fork sensor was inserted to test the AFM. Figure 1.9 b) shows a raw data plot of a $\Delta f\,(V_s)$ spectrum, taken at a Z distance of 5 Å higher than defined by the tunneling setpoint. The curve follows the expected parabolic shape and confirmed also the operational readiness of the AFM.

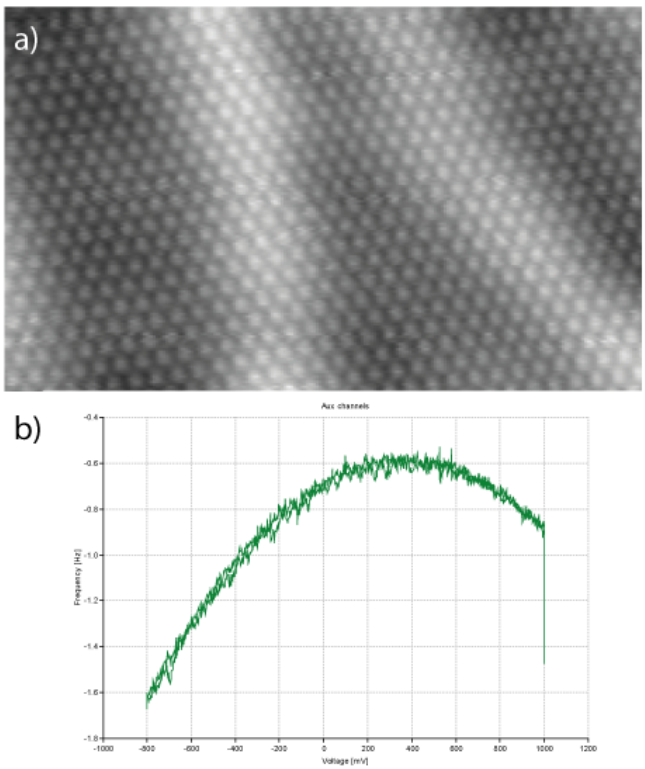

Figure 1.9.:
First results with the new STM/AFM at low temperatures. **a)** One of the first images showing atomic resolution on the Au(111) surface, at 5 K. The raw-data image exhibits no significant noise and proves the optimal condition of the STM. (I_t = 510 pA, V_s = 87 mV) **b)** The first AFM operation at 5 K. The figure shows a raw-data $\Delta f(V_s)$ spectrum taken at a tip Z position 5 Å above the tunneling setpoint (I_t = 150 pA, V_s = 1.05 V).

1.3.3. STM/AFM Wiring, Schematic Diagram and Signal Filtering

With the integration of the AFM parts in the STM also the electronic setup becomes more complex. Figure 1.10 shows a simplified scheme of the connections from outside electronics like AD/DA converter, digital signal processor (DSP) and phase locked loop (PLL) oscillator to the scanner parts which are inside UHV at low temperature.

The base cabling of an STM incorporates the sample bias connection, the tunneling current wire and the piezo high voltage cables. The current to voltage conversion is usually done with an external amplifier DLPCA-200 from Femto [65] (adjustable conversion between 10^3 and 10^9 V/A), attached directly to the cryostat, to keep signal ways short. With the modification to the tuning fork STM/AFM setup, additionally a low temperature current converter - an AD823 operational amplifier [66], with a fixed gain 10^{10} V/A - was mounted into the UHV chamber inside the liquid nitrogen radiation shield. A bistable relay mounted next to it can be switched from outside the chamber to choose between the internal or external amplifier.

Additional connections are needed for the AFM part of the machine. The driving signal is provided by applying an AC voltage to the central piezo. In contrast to established silicon cantilever AFM, where the cantilever readout is done via complex optical setups, the tuning fork readout is relative simple. The tuning fork consists of quartz, which is a piezo electric material [54]. A displacement or bending of the free tuning fork prong leads to a charge redistribution within the crystal. Gold coated electrodes on

the crystal collect the charge and a current between electrodes can be measured. The tuning fork piezo current is converted into a voltage with a gain of 10^8 V/A at a second AD823 operational amplifier mounted in the nitrogen radiation shield. After further low pass filtering, the TF signal is bandpass filtered and adjusted in a post voltage amplifier (SR560, [67]) to make it processable by the phase locked loop (PLL) controller. With this setup we can control the tuning fork sensor to oscillate at amplitudes down to 0.1 Å. From the Nanonis OC4 PLL we record the Δf and A_D signal with the Createc electronics, the oscillation amplitude and the phase error of the PLL are monitored, to ensure the validity of the AFM measurements.

The high quality factor Q of tuning forks leads to an easy excitation of oscillations. In typical operation conditions a tuning fork sensor with a Q of 10000 operated at an oscillation amplitude of $A_{osc} = 50$ pm needs to be excited with an amplitude of $A_{exc} = A_{osc}/Q = 5$ fm. We use a signal divider of $1/10000$ at the driving piezo to have optimal control of the driving amplitude. But due to the high Q noise can become a big problem in an AFM setup. All cables, especially the piezo signals for driving the scanner, must be electrically filtered. E.g. in our setup white noise in the coarse piezos with an amplitude of 10 μV would suffice to excite the TF uncontrollable at 50 pm amplitudes, too.

A filter box mounted at the cryostat high voltage piezo connectors improved the noise level drastically compared to the initial setup, making tuning fork oscillation amplitudes down to 0.1 Å possible. The filter box is thereby relative simple: each of the 10 x-y channels can be switched between unfiltered-bypass (needed when moving the ramp) and filtering. Each of the channels is a second order low pass consisting of two first order 1 kHz RC-low pass filters in series.

PLL: 'Heart and Brain' of the AFM Electronics

The tuning fork is controlled by a so-called phase locked loop (PLL) oscillator. Its main function is to keep the driving signal phase always shifted by 90° (in resonance) with respect to the tuning fork oscillation signal. If the resonance frequency of the oscillator changes, e.g. due to tip-sample forces, the PLL has to readjust the frequency of the driving signal to the new resonance frequency, in order to keep the phase constant (=locked). The difference between the actual resonance frequency and a previously (usually out of tunnel) determined frequency is the frequency shift Δf, the main observable in dynamic AFM. An additional feedback controller in the PLL allows for adjustment of the amplitude of the driving signal, in order to keep the tuning fork oscillation amplitude constant. If the oscillation amplitude is constant, a measurement of $\Delta f(Z)$ allows via an integration (see sec. 1.2.2 and equation 1.15) to yield the force as a function of Z. Moreover, the driving signal yields information about energy dissipation due to tip-sample interactions (sec. 1.2.3).

1.3.4. Tuning Fork Sensor Construction

A first set of two tuning fork sensors (as in fig. 1.8 c) was delivered with the machine from SPS Createc GmbH. After unintended heavy tip crashes the sensors may degrade.

This can result in asymmetric resonance peaks and lower quality factors.

To have always a well working sensor, we started to fabricate our own sensors, following the design of the Createc sensors. The basis is the Macor support which has holes to fit the magnets and metal spheres for electric contacts. A rotationally symmetric cutout allows a safe sensor transfer into the cold STM with a special fork like tool. Two magnets are used to hold the sensor in the STM in the right orientation.

Three spheres make the electrical contacts for tunneling current and the tuning fork current. Magnets, spheres and the tuning fork and wires are glued with a non-conductive UHV compatible adhesive H77 from Epotek [68]. The used tuning forks are standard quartzes type E158 from MicroCrystal [69] with a resonance frequency of 32.768 kHz. The stiffness was reported to be 1800 N/m [21]. They are glued to the Macor support so that the free prong can oscillate perpendicular to the sample surface. The tuning fork electrical contact wires are first glued with conductive glue H21D from Epotek [68] and then stabilized with H77.

One of the most critical parts is gluing the tungsten tip wire to the free prong of the tuning fork with non-conductive glue. We changed the wire thickness from the original 75μm to 50μm and later even 25μm. The reduction of the wire diameter to 50μm already reduces the mass to 44% (at 25μm to 11%) of a 75μm wires mass. Additionally less glue is needed to fix the wire to the tuning fork. We can produce tuning fork sensors with high resonance frequencies in the order of 28 kHz. For tunneling current measurements a 12.5μm gold wire is glued in a last construction step with conductive glue to the tip. The sensor tips are shortened to the proper length by electrochemical etching with NaOH solution, just before the transfer into the chamber, in order to reduce oxidation of the metallic tip.

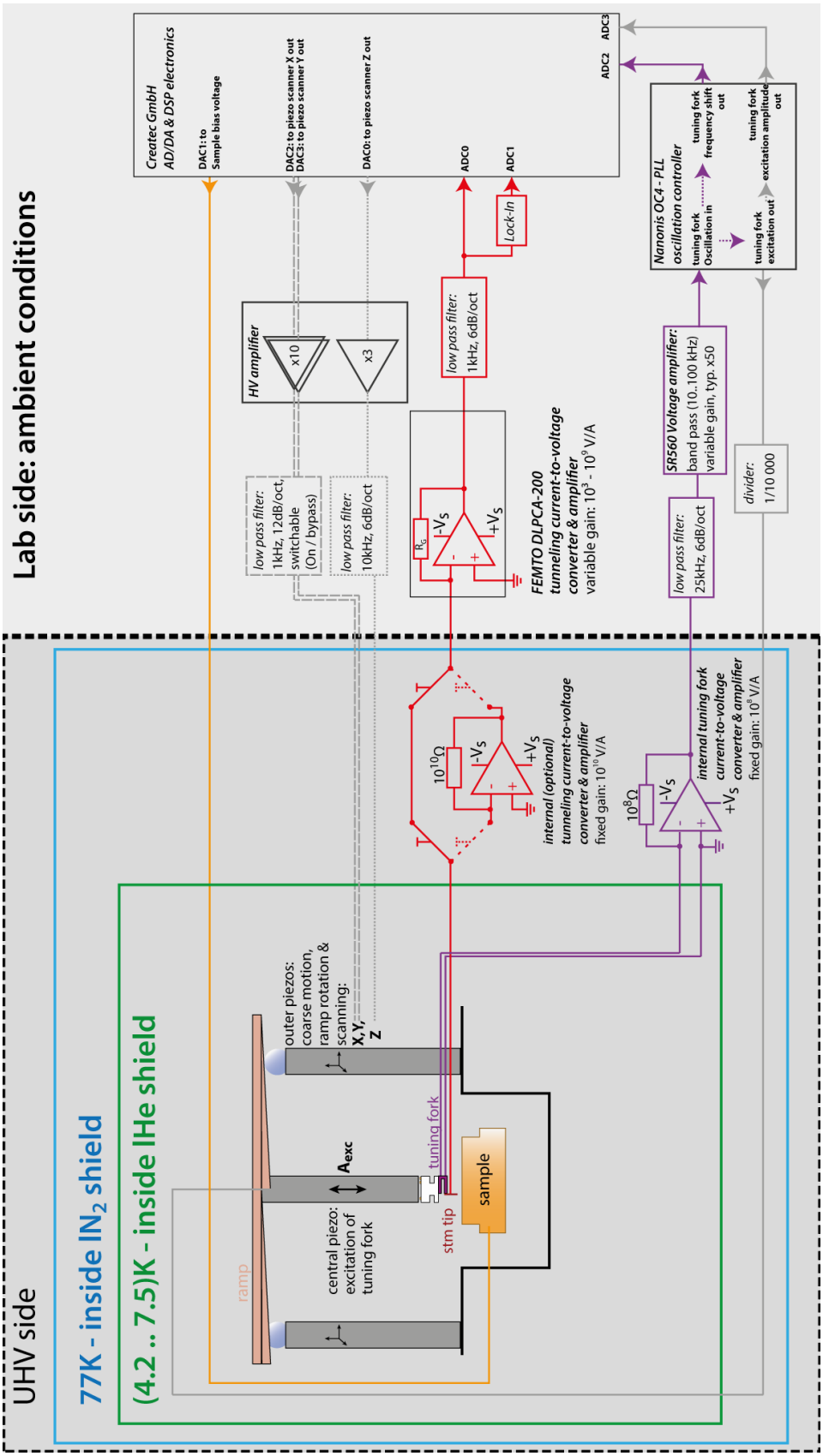

Figure 1.10.: SPM system electric circuit diagram. The SPM head with the TF sensor is housed in the LT part of the UHV chamber, the TF current amplifier is mounted on the lN_2 shield. Filters, controller electronics etc. are connected from the LAB side into the UHV chamber by UHV feedthroughs. For controlling of the SPM and data acquisition a computer (not shown), running special controller software, is connected to the Createc electronics and Nanonis OC4.

1.3.5. Substrates and Preparation Methods

In this thesis we investigate very well defined single molecule contacts and molecular islands. To be able to identify single molecules or to allow molecules to arrange in ordered islands, a requirement is also a well defined, atomically clean substrate. The low-index surfaces of coinage metal crystals are well characterized and understood and serve as substrates in many surface science studies. They are relative easy to clean and prepare. To remove adsorbates, they are sputtered with ionized noble gas atoms, accelerated to kinetic energies in the order of $\sim$ 1 keV and annealed afterwards to yield samples with large flat terraces.

The systems investigated throughout this thesis incorporated different noble metal single crystals. The investigated samples were Au(111), Cu(111) and Cu(110) single crystals. Properties of the different surfaces are listed in table 1.1.

All samples were prepared by repeated cycles of sputtering with Ne^+ ions and annealing to $\sim$800K to obtain an atomically clean, flat surface. Afterwards, the samples were prepared further (e.g. molecule evaporation), cooled down and transferred into the cold SPM. The preparation of the different systems will be described in the corresponding sections.

Surface	pattern	step height	Atom next neighbor distance	Work function
Au(111)	hexagonal	2.3545 Å	2.8837 Å	5.31 eV
Cu(111)	hexagonal	2.0871 Å	2.5561 Å	4.946 ± 0.010 eV
Cu(110)	rectangular	1.2781 Å	2.5561 Å $\times$ 3.6149 Å	4.4 eV

Table 1.1.: Physical properties of noble metal surfaces used in this thesis [5, 70–72]

Chapter 2.

Electron Transport Properties of Molecular Conformations Correlated with the Molecular Stiffness

Molecular wires are essential building blocks of molecular electronic devices. Of great interest is the dependence of their conductance on environmental influences. The conductance of molecular wires is affected by the contact to the metallic leads [73, 74]. But mechanical stress can also alter the conductance [12, 75]. Molecular break junction (MBJ) experiments can deliver insight on general properties of the wire stretching process, allowing to correlate the molecular wire conductance with the force and, hence, structural changes in the junction. Due to the experimental design of MBJ, that allows no control of the individual contact formations, only averaging over many contact formations reveals general properties of the molecular devices [76].

The goal of this study is to correlate the molecular electrical conductance with structural changes of individual molecular wires. We report on the controlled lifting of a flexible molecular wire, namely 1,4-**b**is(**p**yridin-4-yl**e**thynyl)**b**enzene (BPEB), combining dynamic force microscopy with scanning tunneling microscopy. During the lift-up process, we identify characteristic plastic and elastic deformations of the molecular wire in the AFM frequency shift signal. We correlate these with features in the electrical conductance, supported by DFT calculations. Overall, we can draw a detailed picture of the lifting process, starting from the contact formation until the wire breaks off from the tip.

2.1. BPEB on Cu(110)

Polyphenyls are an interesting species for molecular wires: at small dimensions they combine high stability with good conductance through their conjugated π system. Figure 2.1 shows a structural model of 1,4-**b**is(**p**yridin-4-yl**e**thynyl)**b**enzene (BPEB). Two pyridine rings are symmetrically attached to a central phenyl, each via a linear, *sp* hybridized ethyne group. In gas phase the molecules are linear and planar (as shown in fig. 2.1). The conjugated π system extends over the whole molecule, which gives rise to high electron conductance along the molecule [78, 79]. The BPEB molecules were evaporated from a Knudsen cell, heated to ∼108 °C, onto the atomically clean, flat sample which

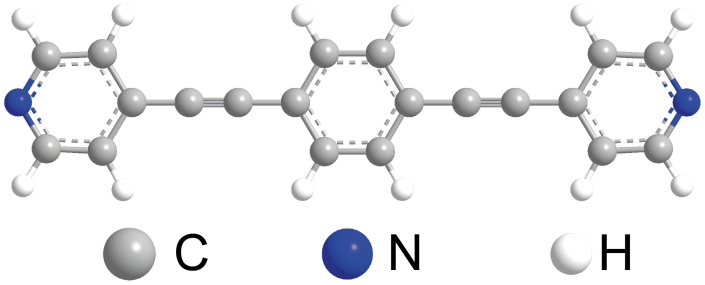

Figure 2.1.: Structural model of BPEB. Molecules were synthesized by Coral Herranz-Lancho and Mario Ruben [77].

was held at room temperature. Then the sample was cooled and transferred into the 7 K cold microscope for inspection.

Figure 2.2 a) shows a low temperature STM image of BPEB molecules adsorbed on the Cu(110) surface. A single molecule can be identified by elongated features, composed of three protrusions. Most of the molecules adsorb individually and separated from each other on the surface. A superimposed structure model in fig. 2.2 b) shows that the protrusions can be assigned to the three aromatic rings of the molecule. The position of the nitrogen atoms in fig. 2.2 b) is pointed out by red arrows. These can be identified in the STM images as dark depressions at the ends of the molecules [80, 81]. Due to the nitrogen lone pair electrons pointing away from the molecule, pyridine rings form coordination-like bonds to transition metals. Therefore the formation of a stable contact to a Cu-terminated tip seems to be feasible [81–83].

Figure 2.2 c) shows an illustration scheme of the lifting process. I) First the tip is placed on top of a nitrogen atom, the feedback switched off, and the tip vertically approached towards the molecule. II) At close enough distance the molecule binds to the tip via the nitrogen lone pair electrons. III) Last, the tip is retracted, lifting the molecule up, until one of the bonds, i.e. tip-molecule or molecule-surface, breaks. During this whole manipulation process we record tunneling current, frequency shift, tip oscillation amplitude and tuning fork driving signal (related to energy dissipation).

2.2. Conductance of a BPEB Molecular Wire

Figure 2.3 b) and c) show STM images of a BPEB molecule before and after a lifting experiment. The green circle indicates the tip's lateral position during the pulling. Figure 2.3 a) shows the corresponding conductance trace of a lifting experiment. The zero ΔZ value corresponds to the tip height where the feedback loop was opened, defined by a given tunneling setpoint ($V_s = 1$ V, $I_t = 200$ pA). From this point, the tip was approached (violet curve) 4 Å towards the molecule. The tunneling conductance increases exponential with the distance in the tunneling regime. At $\Delta Z = -3.85$ Å ('A' in the graph) the conductance increases nonlinearly by a factor of 2, indicating the contact formation between the molecule and the tip. During the retraction of the tip (red curve), the conductance shows higher values due to the additional conductance channel through the molecule [75, 84]. During the lift up process initially the conductance decreases. An overall lower slope compared to the pure vacuum tunneling can be attributed to the

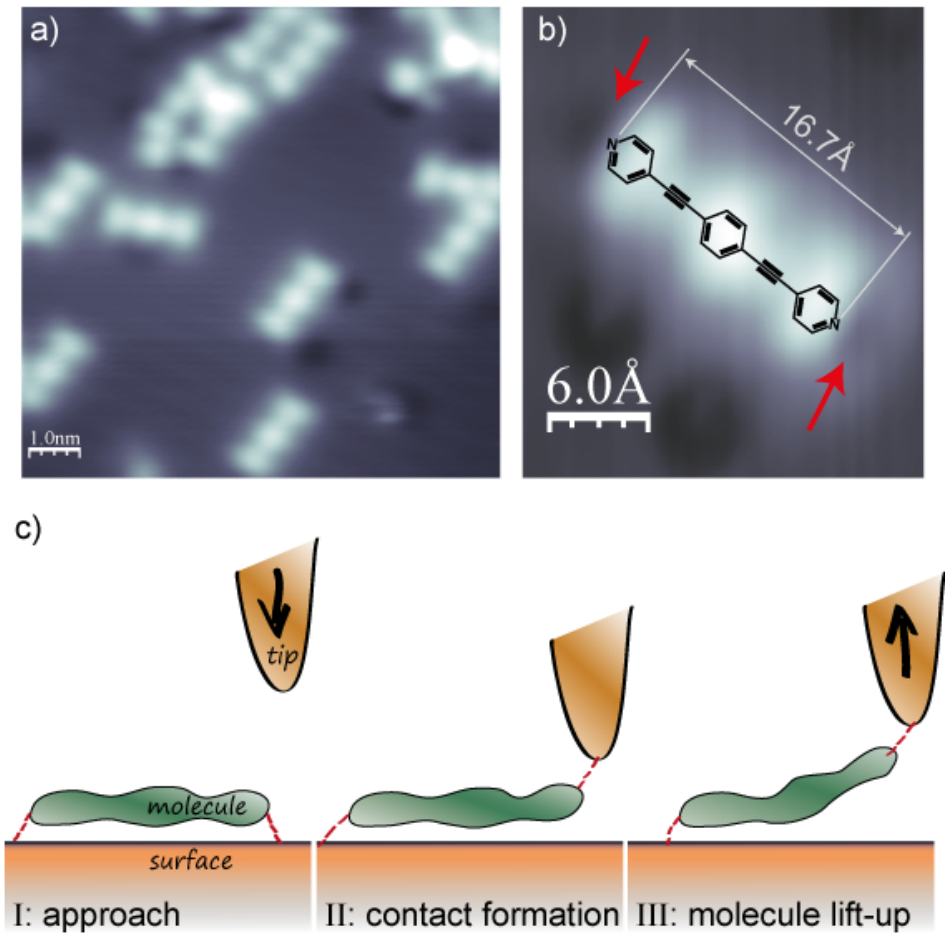

Figure 2.2.: a) BPEB on Cu(110), STM image ($V_s = 0.25$ V, $I_t = 110$ pA). **b)** STM image of a single BPEB molecule and a BPEB structure model overlay ($V_s = 0.25$ V, $I_t = 100$ pA). The red arrows point on depressions, visible in the STM images at the ends of the molecule. These indicate the positions of the Nitrogen atoms, at which the molecules can be contacted with the tip. **c)** illustration of the lift-up steps with an STM tip: *I:* the tip approaches the molecule from atop a nitrogen atom *II:* a contact between tip and molecule is formed *III:* the tip is retracted and lifts the contacted molecule up

reduced tunneling barrier through the molecule [79, 82]. The damping factor β of the exponential tunneling current decay $I_t \propto \exp(-\beta Z)$ of about $\beta = 0.8(2)$ Å^{-1} (vacuum gap: 2.05(5) Å^{-1}) is typical for organic molecules [79, 85]. Small, characteristic nonlinearities are labelled 's0', 's1' and 's2'.

2.2.1. Atypical Conductance Increase

An atypical lifting behavior of the molecular wire was observed at the feature labelled 'B' (fig. 2.3 a). Instead of the monotonic decrease, a nonlinear sudden increase in

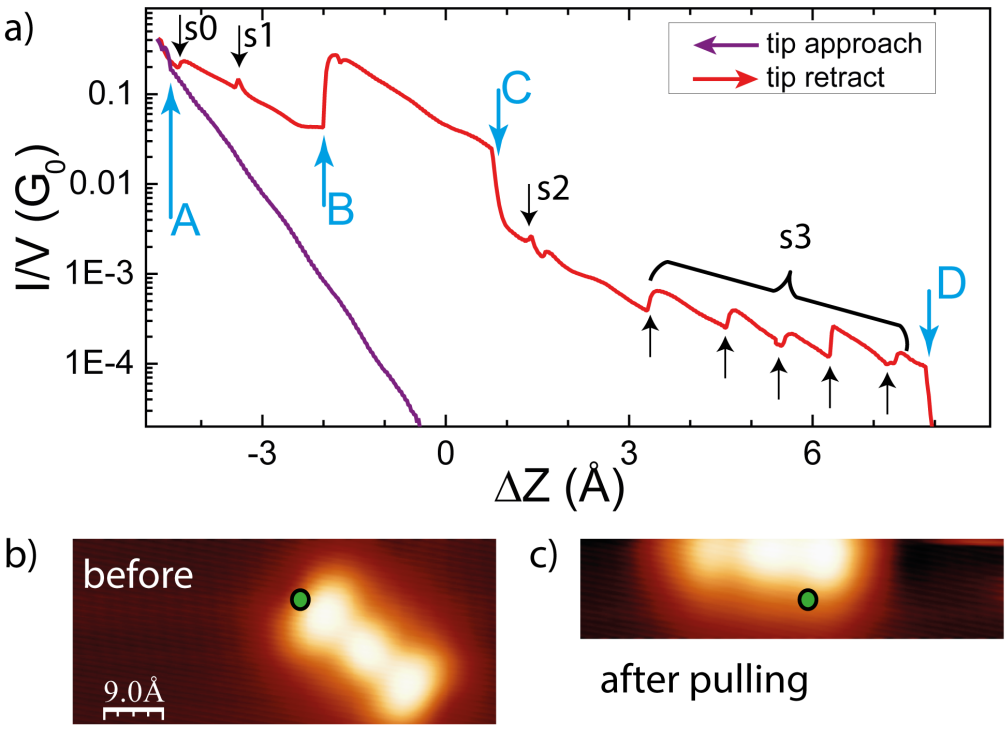

Figure 2.3.: a) BPEB lifting spectrum: conductance in $G_0 = 2e^2/h$ as a function of the tip distance from the tunneling setpoint. Indicated labels correspond to A: contact formation between molecule and tip B: atypical conductance increase during pulling and C: conductance decrease D: tip-molecule bond rupture. (tunneling setpoint: $V_s = 1$ V, $I_t = 200$ pA, sample bias during spectrum: $V_s = -0.1$ V) **b,c)** STM image of a BPEB molecule before (b) and after (c) the lift-up process. The green circle indicates the STM tip lateral position during the experiment. ($V_s = 1$ V, $I_t = 200$ pA)

the conductance by a factor of ~ 5 was observed. At about +2.8(3) Å further pulling from feature 'B' the conductance decreases again by a factor of $\sim$5, as indicated by 'C'. Conductance trace 'B' to 'C' could be reproduced with different molecules and STM tips. Its origin is revealed by DFT calculations.

Upon further pulling, more conductance increase steps (labeled 's3', G increases by a factor of $\sim$2) can be observed.

At a certain pulling distance, here about 12.5 Å from the contact formation, the tip-molecule bond breaks and the molecule falls back onto the substrate. Figure 2.3 c) shows, that the molecule has been displaced by the lifting.

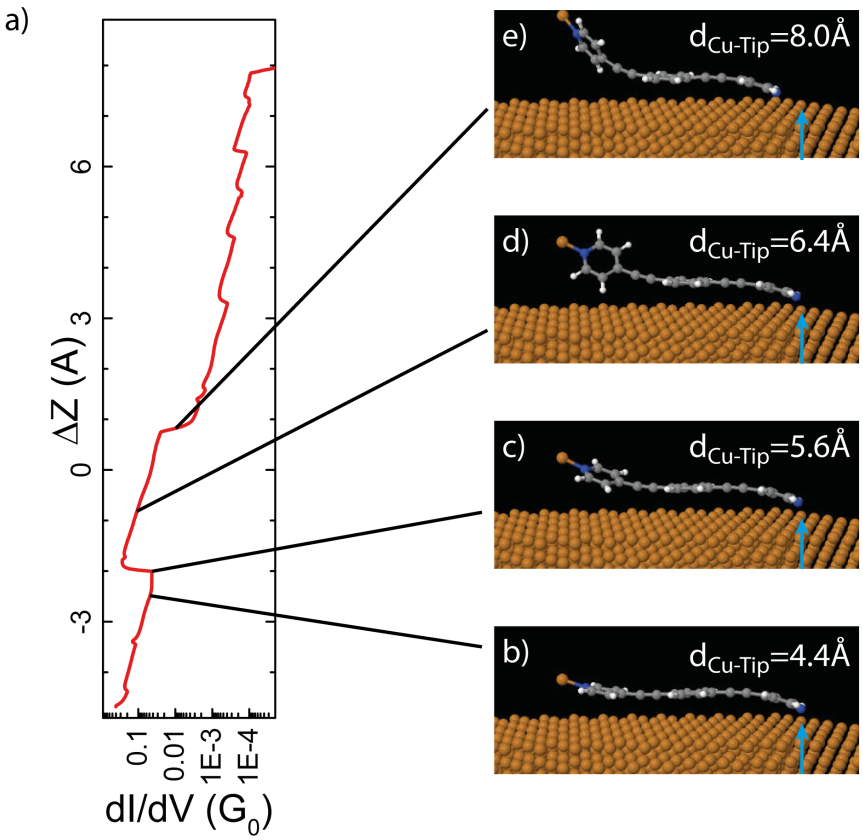

Figure 2.4.: a) BPEB conductance versus lifting distance. The lines connect the conductance states with the calculated molecule structures. **b)** to **e)** MM3 force field energy minimized structures for different distances d between Cu-surface and tip. The initial lateral position of the right nitrogen atom is indicated by the blue arrows. The rotation of the (left) pyridine ring around the Cu-N bond from images b) to d) is increasing. In e) the ring has rotated back. This is possible due to a relaxation of the molecule by a plastic change of its adsorption position on the Cu lattice.

2.3. Simulation of a BPEB Molecular Wire Lifting Process

In order to understand and interpret the conductance anomaly at 'B', reproducibly observed during the lifting of BPEB molecules, simulations of the process were conducted.

2.3.1. Structural Changes Revealed by Force Field Simulations

As a first approach we simulated the experiments by means of the MM3 force field, as implemented in the Tinker molecular mechanics and dynamics package [86–89] (for details see also Appendix A). The advantage of the force field calculations are their low computational costs, allowing to simulate the lifting process with very fine Z resolution.

A single BPEB molecule was placed on a Cu(110) slab with periodic boundary conditions. A copper atom, simulating the STM tip, was bonded to one pyridine nitrogen at a N-Cu distance of 2 Å and vertical distance of 3 Å from the Cu surface. The copper tip-atom was then lifted upward in Z direction in steps of 1.5 pm and the whole system minimized in energy at every step. The lifting and minimization steps were repeated until the molecule was finally detached from the surface.

The force field calculations revealed intramolecular structural changes that might influence the molecules conductance. Figure 2.4 b) to e) show the molecular structures for 4 different tip to Cu-surface distances correlated with the measured conductance vs. distance curve in figure 2.4 a). Up to a height value $Z = 5.6$ Å the molecule lies mainly planar on the substrate due to π-stacking of the aromatic system with the surface [90, 91]. The pyridine ring is bent upwards to follow the tip Cu-atom (b). At 5.6 Å the ring starts to rotate around the Cu-N bond axis as one can see in c). The rotation becomes more evident at further lifting; at 7.8 Å the ring is perpendicular to the Cu surface. In general aromatic ring structures prefer to adsorb planar on a metal surface. During lifting, the pyridine ring is stabilized by its π interaction with the substrate. This leads to a bending of the pyridine ring out of the surface plane, which is unfavorable for the *sp* hybridized (linear) ethyne group and supports the ring-rotated structure.

At $Z = 8.0$ Å (fig. 2.4 e) the molecule changed its adsorption position on the Cu surface in a plastic step, leading to a relaxation of the molecular structure and a partial back-rotation of the lifted pyridine ring. The distance between the starting of the ring rotation and relaxation is about 2.4 Å. This is consistent with the observed distance of 2.8(3) Å between the conductance increase and decrease, as observed in typical conductance versus distance spectra like 2.4 a).

The force field simulations depict the behavior of the molecule during the lift-up process and suggest a conformational origin for the unexpected increase of the conductance at point 'B'. A rotation of the aromatic ring would lead to an reduced overlap of the π orbitals of the ring and the -C≡C- bridge, thus reducing the conductance through the molecule [82, 92], which is in contrast to the experimental observations. But force field calculations are missing electronic structure. The latter can be obtained from density functional theory, allowing to model the system of tip, molecule and substrate.

2.3.2. Lifting Simulation by DFT: Conductance and Structure

We collaborated with Thomas Niehaus and Alessandro Pecchia, who performed the following DFT calculations. They modeled the system using the LDA functional as implemented in the SIESTA code [93–95]. For the molecule (C, N, H atoms) Troullier-Martins pseudopotentials and double-ζ basis were used; for the surface and tip pseudopotentials and basis, optimized for Cu (surfaces) as described in [96]. Calculations were performed on a slab ($\Delta X, \Delta Y = 25$ Å, $\Delta Z = 50$ Å) with periodic boundary conditions, to model the experiment.

A cluster of several copper atoms is used to model the tip (see fig. 2.5 a). All the distances in the DFT calculations refer to the point of contact between the foremost tip atom and the copper surface. The modeling started with a tip-surface distance of 1 Å

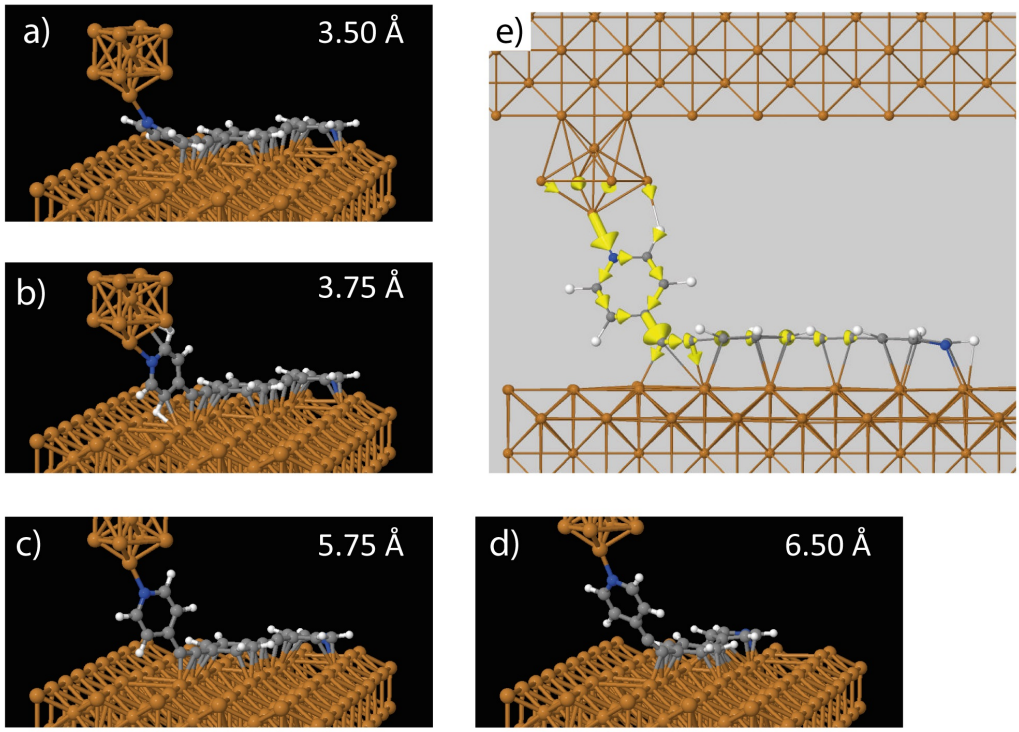

Figure 2.5.: a) - **d)** BPEB lifting DFT simulation: minimized energy structures. Between 3.75 Å and 5.75 Å the pyridine ring is rotated perpendicular to the surface. The carbon atom after the lift up pyridine is usually sp hybridized. In the ring rotated structure it is sp^2 hybridized and forms an additional covalent bond to the underlying Cu substrate atom. **e)** visualization of the local current (from Landauer-Büttiker theory) through the molecule for the ring-rotated structure. The sp^2 hybridization of the carbon atom gives rise to increased current into the underlying Cu substrate. By courtesy of Thomas Niehaus and Alessandro Pecchia.

and the frontal tip atom in a covalent bond distance to one nitrogen atom of the BPEB molecule. The tip was then lifted, with the N forming a bond to the tip, in steps of 0.25 Å followed each by a structure optimization.

Modeling BPEB Lifting by DFT

Figures 2.5 a) to d) show DFT optimized structures at different tip-sample distances from a sequence of tip lifting steps ($\Delta d = 0.25$ Å). Up to 3.5 Å (a) the molecule remains mainly planar on the surface. The lifted up pyridine is bent up slightly to follow the tip, while there is no rotation around the Cu-N bond. At 3.75 Å the lift-up pyridine ring rotates, remaining with its plane perpendicular to the Cu surface until $d = 6.25$ Å. In contrast to the force field calculation, the ring rotations are plastic steps instead of smooth transitions. This is in agreement with the sudden increase of the conductance during the pulling in the experimental conductance-distance spectra.

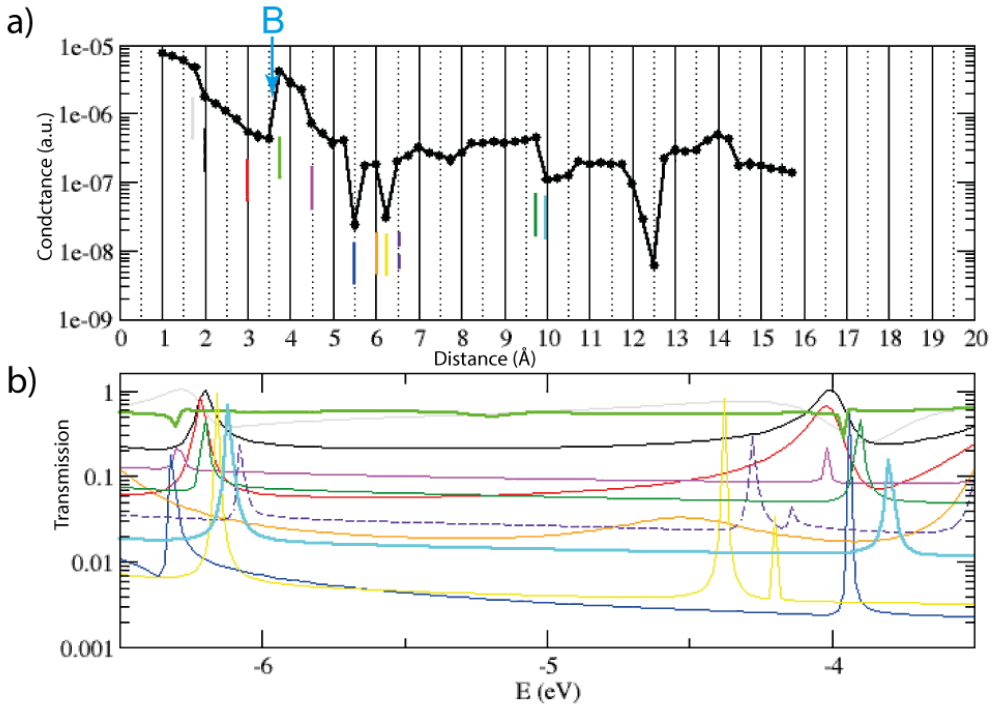

Figure 2.6.: a) DFT simulation of the BPEB lifting: conductance as a function of the tip-sample distance. At 3.75 Å the conductance increases by one order of magnitude. **b)** Transmission function vs. energy at distances given in a) (indicated by the correspondingly colored line). By courtesy of Thomas Niehaus and Alessandro Pecchia.

The preference of the sudden ring rotation over the planar structure is here due to a change of the hybridization of the one carbon atom binding to the lift-up pyridine ring: it changes from linear sp hybridization into sp^2-like hybridization, thus forming an additional bond to the Cu substrate. This is most evident in figure c): The angle between the pyridine ring and the two linear carbon atoms (Pyridine-C(Cu)=C-) is about 129 °, which is closer to the ideal trigonal-planar sp^2 bond angle of 120 ° than to an sp bond angle of 180 °. At $d = 6.5$ Å the pyridine is lifted up from the surface (figure 2.5 d) that the carbon-copper bond breaks and the carbon becomes detached from the surface.

Figure 2.5 e) shows a visualization of the local current from Landauer-Büttiker theory. The current per atom is plotted by yellow arrows on a ring-rotated molecule with sp^2 hybridized C atom, where the arrow size visualizes the fraction of the total current. The bond of the carbon atom allows direct current flow into the substrate, thus enhancing the conductance in the junction.

Simulation of Electron Transport Properties during the Lifting of a Molecular Wire

Figure 2.6 a) is a logarithmic plot of electron conductance as a function of the tip-sample distance. At a separation from 3.5 Å to 3.75 Å ('B', above green vertical line) the conduc-

tance increases by one order of magnitude, comparable to the experiment. This is exactly the position, where the ring rotation happens. The conductance decreases already ∼1 Å after the increase, much faster than experimentally observed.

In figure 2.6 b) the transmission functions for the tip-sample distances indicated by the colored vertical lines in figure 2.6 a) are plotted on a logarithmic scale as a function of the energy with respect to the vacuum level. From dI/dV spectra (not shown) we know that the lowest unoccupied orbital of the molecule lies around 1.8(1) eV above E_F, so we can assume that the fermi level in the calculation should lie around -5.5 to -5 eV. In this region the transmission curves are all flat, but differ by orders of magnitude, depending on the tip-sample distance. So the conductance increase is indeed not a feature of an electronic resonance, but attributed to an overall increase of the conductance due to the hybridization with the substrate.

In summary, it has been shown, that an intramolecular structural change can lead to a hybridization of a C atom from sp to sp^2. Being this the origin of the sudden increase in conductance, the question comes up, if these structural changes can be experimentally probed. The qPlus design AFM is a promising approach to correlate the conductance of a molecule with molecular structural changes.

2.4. Measuring the Stiffness of a BPEB Molecular Wire

The qPlus design enables us to measure, similar to fig. 2.3 a), simultaneously the conductance and the frequency shift as a function of the tip-sample distance with a molecule attached to the tip. In this experiment we operated the tuning fork at an oscillation amplitude of 10 pm. During the measurement the oscillation amplitude was kept constant. We measured also the tuning fork driving signal A_D, which is a measure for the dissipation due to tip-sample interactions. Small oscillation amplitudes and absence of dissipation allow a direct conversion from the measured frequency shift into tip-sample force gradient ([21, 41], see also sec. 1.2, eq.1.12). The typical tuning fork parameters throughout this AFM experiment were $f_0 = 28648$ Hz, $Q \approx 15000$ and $k = 1800$ N/m.

Figure 2.7 a) shows a frequency shift-distance spectrum. The zero ΔZ value corresponds to the tip height where the feedback loop was opened, defined by a tunneling setpoint value ($V_s = 0.25$ V, $I_t = 110$ pA). Before approach, the bias voltage was set to -0.2 V. From this point the tip was approached 4 Å toward the molecule, to form a tip-molecule contact. Subsequently the tip was retracted by 20 Å. The tip-molecule bond is always broken before reaching the end point of the retraction (not shown in fig. 2.7). The Δf approach curve, before contact formation, was fitted with a van der Waals force (Hamaker approach, see sec. 1.2.4), accounting for the vdW interaction between tip and sample. The fit curve was then subtracted from the retraction $\Delta f(Z)$ spectrum to remove the effect of the long-range van der Waals background of the tip. The resulting curve $\Delta f(Z) = \Delta f_{retract}(Z) - \Delta f_{approach-fit}(Z)$ is plotted in figure 2.7 a).

Figure 2.7 c) shows the simultaneously recorded tuning fork driving amplitude A_D, which is related linearly to the tip-sample energy dissipation (sec. 1.2.3, eq. 1.18). The observed values do not differ too much from the driving amplitude of the free tuning

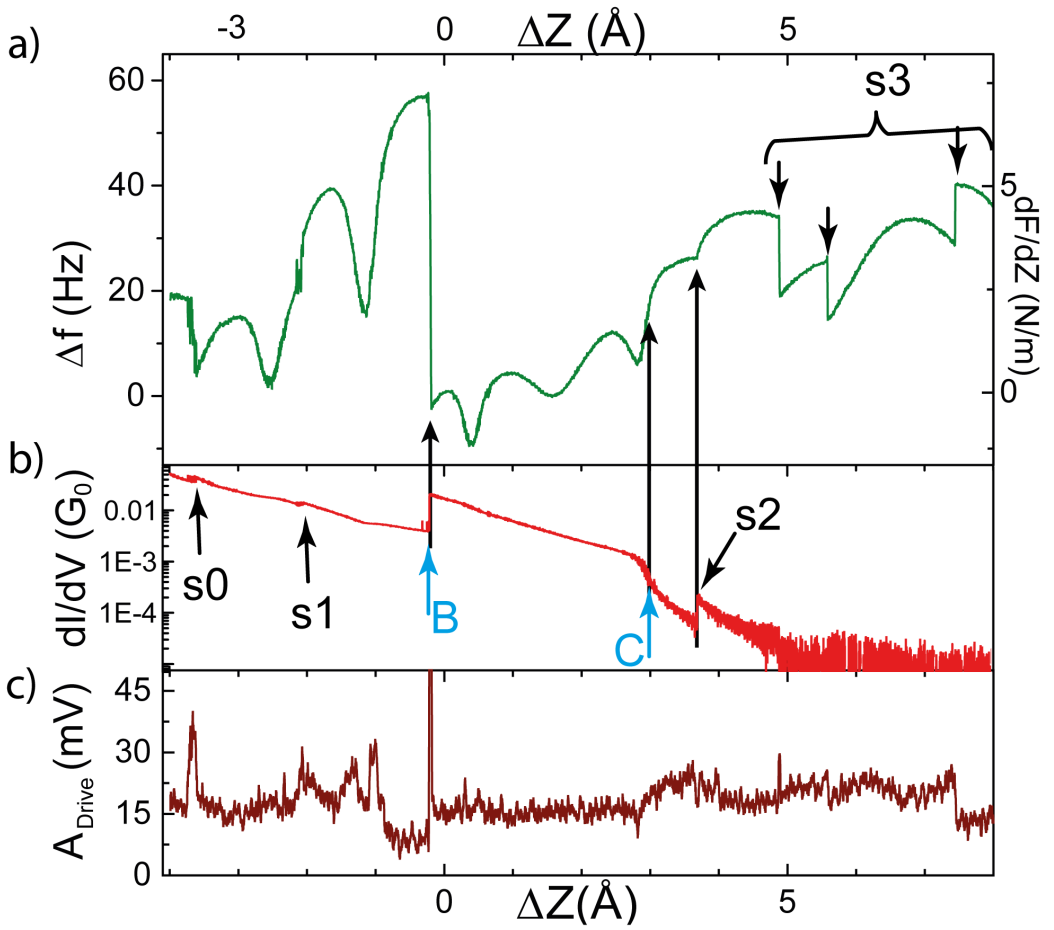

Figure 2.7.: a) BPEB $\Delta f(Z)$ lifting spectrum. **b)** simultaneously with a) recorded dI/dV. Bandwidth restrictions of the current-to-voltage converter limit the conductance resolution at combined STM-AFM operation, compared to the pure STM setup (fig. 2.3 a). **c)** Driving amplitude of the AFM tuning fork. The signal is connected with the tip-sample damping (eq. 1.18); the value for the free lever is here $A_D = 15$ mV. (tunneling setpoint: $V_s = 0.25$ V, $I_t = 110$ pA, sample bias during spectrum: $V_s = -0.2$ V)

fork of 15 mV. Under these experimental conditions - small and constant oscillation amplitude and small tip-sample dissipation - the relation between the measured frequency shift and the force gradient is given by:

$$\frac{\partial F}{\partial Z} = \frac{2k_0}{f_0}\Delta f. \tag{2.1}$$

and we can relate the measured Δf to the junction stiffness $\partial F/\partial Z$ [21, 41].

Correlation of Stiffness and Conductance

Figure 2.7 a) will be described in separate parts. The first part from $\Delta Z = -4$ Å to $\Delta Z = -0.2$ Å ('B') shows an overall linear increase of the frequency shift up to 57 Hz. This corresponds to a stiffness of 7.16 nN/nm, a typical value for molecule and metal point contacts [74, 97]. A linear increase of the stiffness corresponds to a quadratic force-distance dependence. Metallic point contacts have shown Hooks law like linear force-distance relations [97,98], while for organic molecules experiments, like unfolding of proteins, have shown also non-linear relations [99–101].

In our experiment the Δf increase can be interpreted by considering the calculation results: the backbone of the molecule stays planar adsorbed on the surface due to π-stacking and only the pyridine ring is being lifted up. The bending of the ring is unfavorable for the sp bonded ethyne carbon atoms and leads to an increasing restoring force towards the sample - and so an increase of the frequency shift.

The increase of the frequency shift is not a pure linear function but shows some significant dips. These can be only observed with very small oscillation amplitudes. This modulation could originate from the motion of the flexible molecule on the atomically corrugated surface [102–104]. The nonlinear conductance features 's0' and 's1' (compare also fig. 2.3) can be observed in the conductance (figure 2.7 b) and simultaneously in the $\Delta f(Z)$ curve figure 2.7 a), where they appear as nonlinear steps, caused by plastic changes in the molecular junction.

Relaxation and Conductance Increase

At -0.2 Å the Δf shows a sudden change from 57 Hz down to -2.6 Hz, indicating a significant plastic deformation and the relaxation of the molecular junction. We find a correlation with the conductance increase feature at 'B' in the simultaneously recorded dI/dV curve figure 2.7 b). Hence, the $\Delta f(Z)$ feature is attributed to the ring rotation, found in both, DFT and Force Field simulation, and to the sp to sp^2 rehybridization of the C atom.

In the high conductance regime ('B' to 'C' in fig. 2.7 a),b), we observe a general increase of the stiffness. It is elastic due to the absence of tip-sample dissipation (fig. 2.7 c). Along we see again a smooth modulation of the stiffness. The conductance decrease 'C' appears also elastic and rather smooth over a Z distance of $\sim$0.2 Å. An interpretation is that the pulling distorts the molecule such that the conductance decreases.

Plastic Regime

At $\Delta Z = 3.7$ Å ('s2' in the conductance spectrum fig. 2.7 b) a step-like increase of the conductance suggests the occurrence of an additional structural change in the molecular junction. In the Δf plot figure 2.7 a) we find at this position also a nonlinear change in the slope, encouraging this finding. Since this is the first observed plastic change since the initial ring rotation, 's2' should mark the point where the sp^2 C-Cu bond is broken. The observed increase in the conductance could be interpreted such, that the next carbon

atom might rehybridize from sp to sp^2 and form a bond with a Cu surface atom while the first one is detached from the surface.

On further pulling of the molecule, more plastic steps can be observed ('s3' in fig. 2.7 a). STM (without AFM) current-distance curves like in figure 2.3 a) exhibit also further steps of conductance increase (labelled 's3') at longer lifting distances up to the near upright-standing molecule. This suggests that, in analogy to the finding on feature 's2', further atoms of the molecule rehybridize from sp to sp^2 before their detachment, while the molecule is being lifted part by part from the surface.

2.4.1. Evaluation of the sp^2 Binding Energy

In the Z range of the higher conductance, from 'B' to 'C', and up to the plastic step 's2' (fig. 2.7 a) and b) the $\Delta f(Z)$ curve is free of plastic deformations and junction related energy dissipation (2.7 c). A measurement of the frequency shift (converted to dF/dZ in the right hand scale) as a function of the tip-sample distance allows us to determine the change in the force normal to the surface along this path by an integration along the Z direction (eq. 1.15, [21,41]). A further integration can yield the difference in the potential energy between the plastic steps 'B' and 's2'.

Figure 2.8 b), c) and d) show the frequency shift, the corresponding force, and the potential energy as a function of the Z distance (2.8 a), e) show TF driving amplitude and dI/dV vs. Z). Due to lack of information, all values are relative to point 'B' and under the assumption of no integration constants. But we can gain an estimation of the energy difference between the sp^2 and the sp hybridization states of the ethyne carbon (the associated molecular structures at 'B' and 's2' are shown in figure 2.8 f) and g). The energy, accumulated from the beginning at 'B' to the plastic step 's2', marks the barrier height between the two molecular structures and is hence related to the binding energy of the C-Cu bond.

Within the first ~ 1 Å the force becomes positive, thus repulsive, and the energy approaches towards a value of -9 meV. Upon further pulling the force becomes attractive and the potential energy increases. While pulling on the pyridine ring the C-Cu bond is stable until the point indicated by the vertical dashed line in figures 2.8. At this tip retraction height, the accumulated force is strong enough to break the C-Cu bond, and the structure relaxes, recovering the linear sp character in this C atom. We can estimate the bond energy from the energy difference between the local minimum and the energy at point 's2'. The bond breaks at a force of -360 pN and an energy of 150 meV. We find a total bond energy of 159 meV. This is one order of magnitude lower than the typical energy gain by metal-organic bonds [81,105,106]. However, our number is a lower limit for the bond energy and rather a value for the barrier height into the new structure.

We have shown that the measured $\Delta f(Z)$ curves exhibits characteristic nonlinearities that could be assigned to plastic changes of the molecular junction and that are correlated with the atypical increase in the conductance. From the elastic Δf regime of the lifting process we could extract values for the forces and energies of the rehybridization. In order to compare the experimental and simulated lifting processes qualitatively

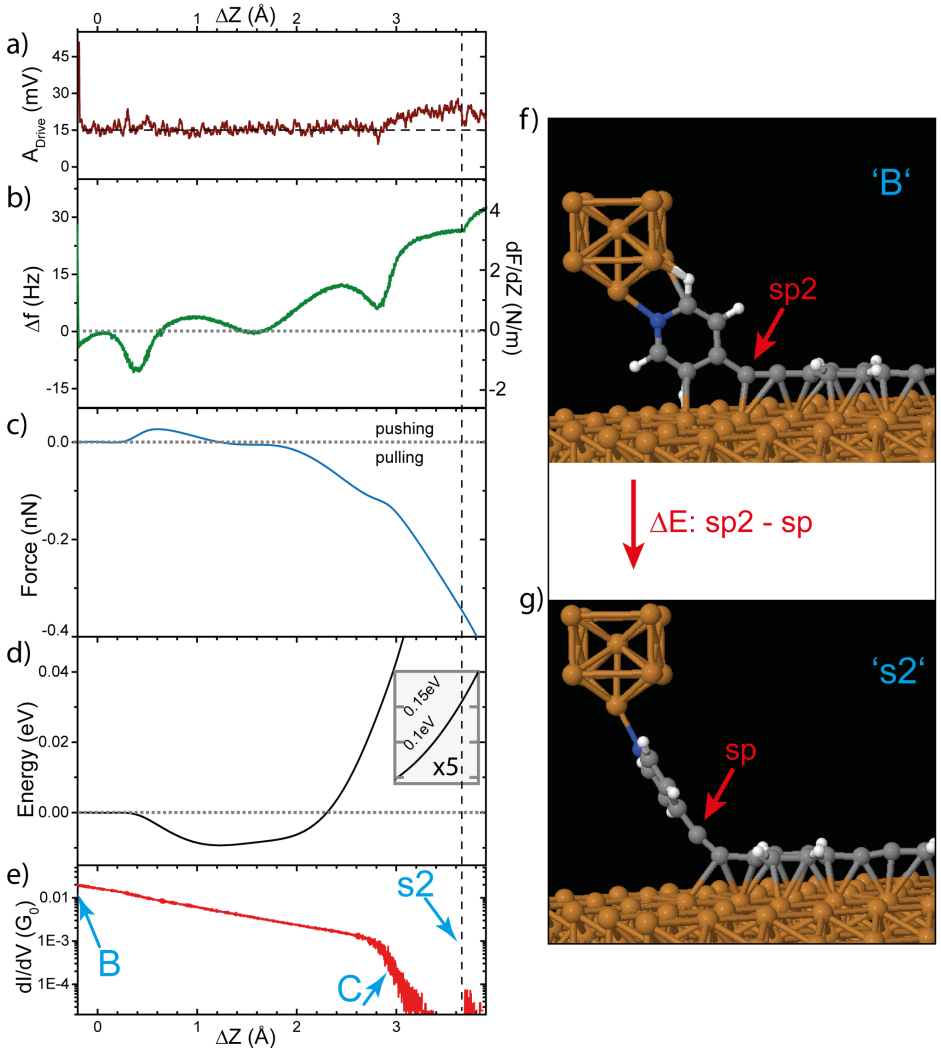

Figure 2.8.: a) Tuning fork driving amplitude. The dashed line at $A_D = 15$ mV is the tuning fork intrinsic dissipation. No significant dissipation occurs in the tip-sample junction. **b)** $\Delta f(Z)$ from BPEB lifting fig. 2.7 a), 'B' to 's2' (the right-hand axis shows the corresponding force gradient). The dashed vertical line denotes the position of the plastic step 's2'. **c)** Force(Z) from integration of $\Delta f(Z)$. Positive forces are directed away from the surface ('pushing'). The force at the bond-breaking is ~ -360 pN. **d)** Energy(Z) from integration of the Force. The energy minimum at around $\Delta Z = 1.2$ Å is -9 meV, the energy at the bond-breaking 's2' 150 meV. The inset shows a region of the graph with $\times 5$ multiplied Energy axis. The integrated values probably underestimate the real values; integration constants were assumed to be zero. **e), f)** molecular structures from DFT, illustrating the two bonding states before and after feature 's2', respectively.

and quantitatively we analyze in the following the distance dependence of the energies obtained from the force field and DFT calculations.

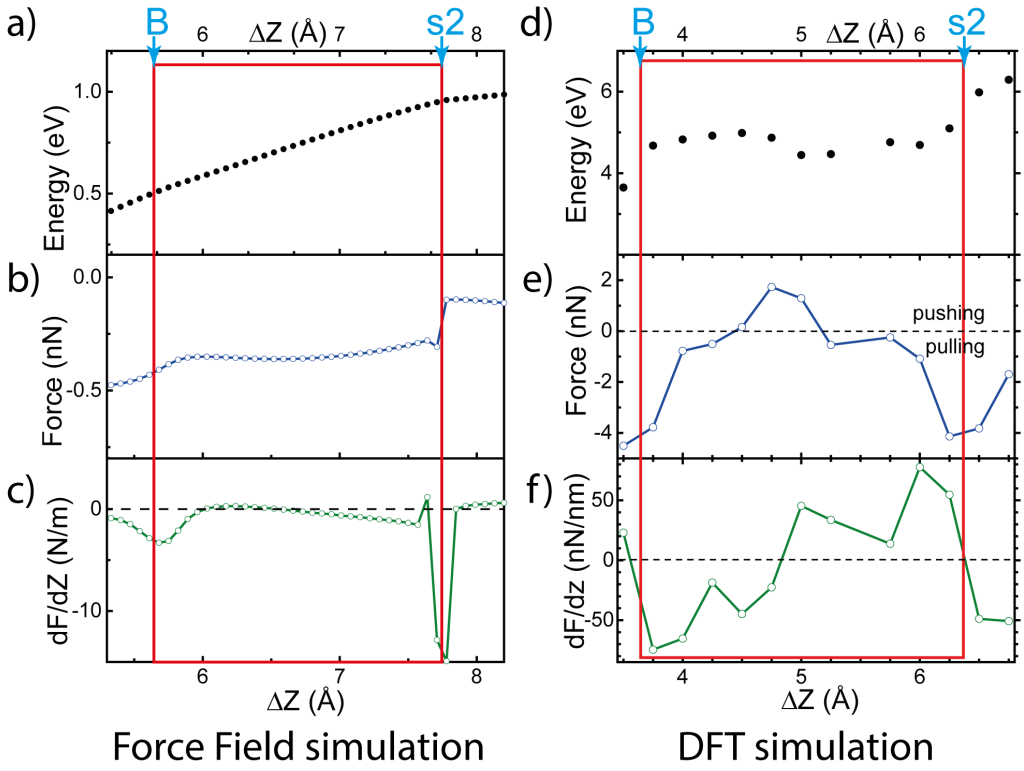

Figure 2.9.: a) Energy vs. Z, obtained from force field calculations and the derivatives in Z-direction: **b)** force and **c)** force gradient vs. tip-sample distance. **d)** Total energy from the DFT calculations as a function of the tip-sample distance and below the derivatives along the Z direction, yielding the normal component of the force (**e)** and the force gradient (**f)**. The red frames surrounds the regions from the beginning to the end of the ring rotation (features 'B' to 's2' in fig. 2.7).

2.4.2. Energy Analysis from Simulations

Computer simulations, both, force field and DFT, find the molecular structure in each lifting point by varying the atom positions, until a local energy minimum is found. So the results from fig. 2.5 and 2.6 do comprise the potential energy of the system as a function of the distance. Differentiation of the energy curves in Z direction yields directly the force along the Z direction and a second derivative yields the force gradient.

Force Field Lifting Spectra

Figure 2.9 a) - c) show energy, force and frequency shift obtained from the force field calculations. The red box marks the tip retraction range from the beginning to the end of the first ring rotation, discussed above ('B' to 's2'). Dips in the force gradient vs. Z curve originate from the ring rotation. In the calculated $dF/dZ(Z)$ curve the fine modulation of the measured Δf on the Å scale can not be produced. The stiffness does not show an

overall increase nor does it reach significant positive values between 'B' and 's2'.

Force field calculations do not consider the electronic structure and so cannot include the covalent character of the Cu-C bond observed in DFT. Thus, our force field calculation results confirm that the first principle description of the chemical structure is essential to reproduce the experimental findings.

DFT Lifting Spectra

Figure 2.9 d) - f) show energy, force and frequency shift obtained from the density functional theory calculations. The red box marks again the region from the beginning ('B') to the end ('s2') of the first ring rotation.

Due to the higher computational costs of DFT calculations, less ΔZ steps could be calculated. So the Z resolution of 25 pm is more coarse compared to the force field calculation. But we find in the force gradient vs. Z a modulation with a periodicity around 1 Å, comparable to the experiment. The general increase of dF/dZ during tip retraction is well reproduced between 'B' and 's2'. The force-distance curve exhibits a transition from repulsive to attractive forces, too.

But the quantitative comparison assigns the calculations more than an order of magnitude too big values. The force gradient varies between ± 75 N/m compared to max. ~ 4 N/m in the experiment. The bond-rupture force is ~ -4 nN, more than ten times the experimental finding. From the calculated potential energy we find an energy difference of ~ 1 eV, about 7 times the experimental value.

While the qualitative agreement in the lifting curves is very good, the deviations in the quantitative results are too high. Even though results obtained from integration can yield errors due to unknown integration constants, the derivatives (dF/dZ) should yield the same magnitudes. The connection between the stiffness changes observed in the experiment and the calculation can be related to the rehybridization of carbon atoms of the molecule, thus explaining also the conductance increase. However, standard DFT functionals like LDA fail to describe dispersive forces as the van der Waals force. Especially the LDA approach is known to overestimate binding energies and underestimates bond lengths [107, 108].

2.5. Conclusion and Outlook

We have succeeded to relate the molecular flexibility and the conductance of the molecular wire BPEB during a lifting process. This was possible by combining different methods, namely scanning tunneling microscopy, dynamic atomic force microscopy and simulations using force field and density functional theory methods.

During the lifting we observed an atypical increase in the conductance at a certain lifting distance due to an intramolecular structural change: The rotation of the lift-up pyridine ring goes with a rehybridization of a specific carbon atom from sp to sp^2. In DFT simulations could be shown that the resulting C-Cu bond formation leads to a shorter current path into the substrate and gives rise to a conductance increase. AFM $\Delta f(Z)$

spectroscopy revealed a change in the molecular junction stiffness that could be correlated with this structural change, and yielded values for the force and energy that are associated with the rehybridization process. While force field simulations could reproduce a ring rotation, the plastic character of the structural change could not be found, thus supporting the requirement of the structural change being also an electronic effect. DFT calculations could qualitatively reproduce the shape of also the force gradient-distance curves, while the quantitative disagreement leaves room for further investigations.

Chapter 3.

Driving a Macroscopic Oscillator with the Stochastic Motion of a H_2 Molecule

Nature widely uses processes that extract energy and coherence from random and noisy sources of energy. Examples of these span from mechanisms for pumping energy in cellular activity [110] to the amplification and transduction of signals [111, 112, 112, 113]. An oscillator coupled to a noisy environment can self-oscillate when the dynamics of the noise is modulated by the oscillator, and vice versa. This phenomenon, named stochastic resonance (SR) [114], predicts the enhancement of energy transfer from the noisy to the periodic sub-system. Noise at the molecular scale is ubiquitous. Stochastic molecular motion is caused by temperature or by stimuli like electrons or photons. In this chapter we show that the stochastic motion of H_2 out of thermal equilibrium induced by tunneling electrons can drive the oscillation of a mechanical oscillator of macroscopic dimensions, demonstrating the concept of energy harvesting through SRs at the molecular scale.

We investigate a molecular tunnel junction formed by H_2 enclosed between two metal electrodes, those of a copper surface and the tip of a scanning tunneling microscope (STM) at low temperatures (5 K). The H_2 molecule can lie in different adsorption states. Fluctuations between these states are triggered by the inelastic tunneling of electrons when they excite certain vibrational modes of the molecule in the cavity. The electron-driven fluctuations of the H_2 molecule are stochastic (Fig. 3.1, from [109]) [115, 116] and involve displacements of tens of picometers, as well as energies of tens of millielectronvolts: they are expected to exert forces on the electrodes of hundreds of piconewtons. The spectral distribution of the stochastic H_2 fluctuation varies with the sample bias V_s (Fig. 3.1 a) and the tunneling current (Fig. 3.1 b). There exists a regime(V_s, I_t) where the H_2 state dwell times (t_0, t_1 in Fig 3.1 b) agree with the resonance frequency $f_0 = 1/t$ of tuning fork based AFMs.

The crucial question treated here is the detection of mechanical forces exerted by the electron-induced molecular motion on the electrodes. To do so, we utilize our quartz tuning fork based AFM, acting here as a mechanical oscillator. We show that this force sensor self-oscillates in response to the fluctuating forces caused by the stochastic switching of a hydrogen molecule. The self-oscillation reveals an efficient energy transfer from the random molecular bi-stability to the periodic motion of the resonator. By theoretical modeling, we determined that the key feature is the concerted dynamics of molecular switching and oscillator motion, coupled to each other through the fluctuating electric

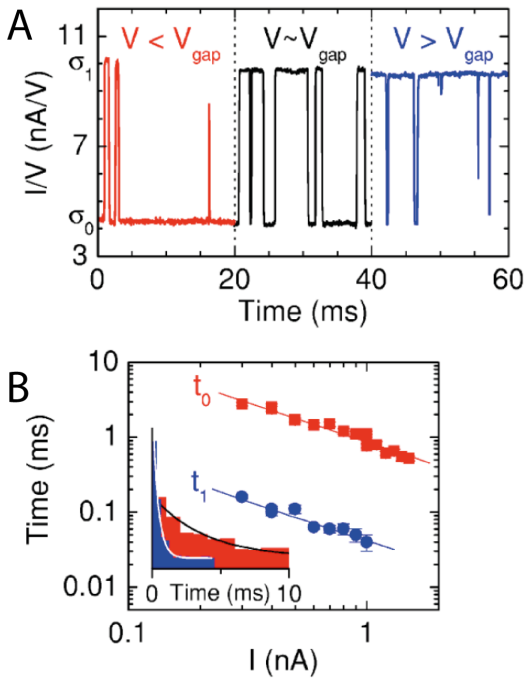

Figure 3.1.: Figure from Gupta *et al.* [109] (A) Two-state noise in a H_2 molecular junction: tunneling current as a function of time at different bias voltages V_s around the voltage threshold V_{th} (V_s = 95 mV, 109 mV, 125 mV). (B) Inset: histogram of dwell times for ground (red) and excited (blue) states at one certain tunneling setpoint (here V_s = 110 mV, I_t = 0.2 nA), along with exponential fits (solid lines). Main (log-log-scale): resultant mean dwell times t_0 and t_1 for different tunneling currents; lines are fits with slope of -1.0.

field and forces in the junction.

This chapter is based on the publication 'Driving a Macroscopic Oscillator with the Stochastic Motion of a H_2 Molecule' by Christian Lotze, Martina Corso, Katharina J. Franke, Felix von Oppen and José Ignacio Pascual, Science **338**, 779 (2012). The theoretical modeling was done by Felix von Oppen. The detailed steps can be found in the supporting online material (SOM) of the publication.

Experimental Details

To form the molecular junction, we exposed an atomically clean Cu(111) surface to a flux of H_2 molecules, at low temperature (5 K) and in ultra-high vacuum. We use a single crystal Cu(111) sample as substrate. Hydrogen molecules are deposited on the cold sample, directly placed at the LTSTM stage. We backfilled the UHV chamber with a H_2 pressure in the order of 5×10^{-7} mbar and open the access to the STM for a few minutes. By controlling the dosing pressure and time, the H_2 coverage can be controlled.

3.1. H_2 Molecular Two Level Fluctuations on Cu(111)

Adsorbed H_2 can be too mobile for imaging by STM at low surface coverages; only after high gas exposures could a H_2 monolayer be imaged as a compact hexagonal lattice (Fig. 3.2A). Nevertheless, the presence of H_2 molecules condensed on the metal surface became evident from sharp non-linearities in the current-bias (I_t-V_s) spectra of the junction (Fig. 3.2B) [109, 116, 118–121]. These features arise from the activation of fast, bistable motion of a H_2 molecule between two molecular configurations with different

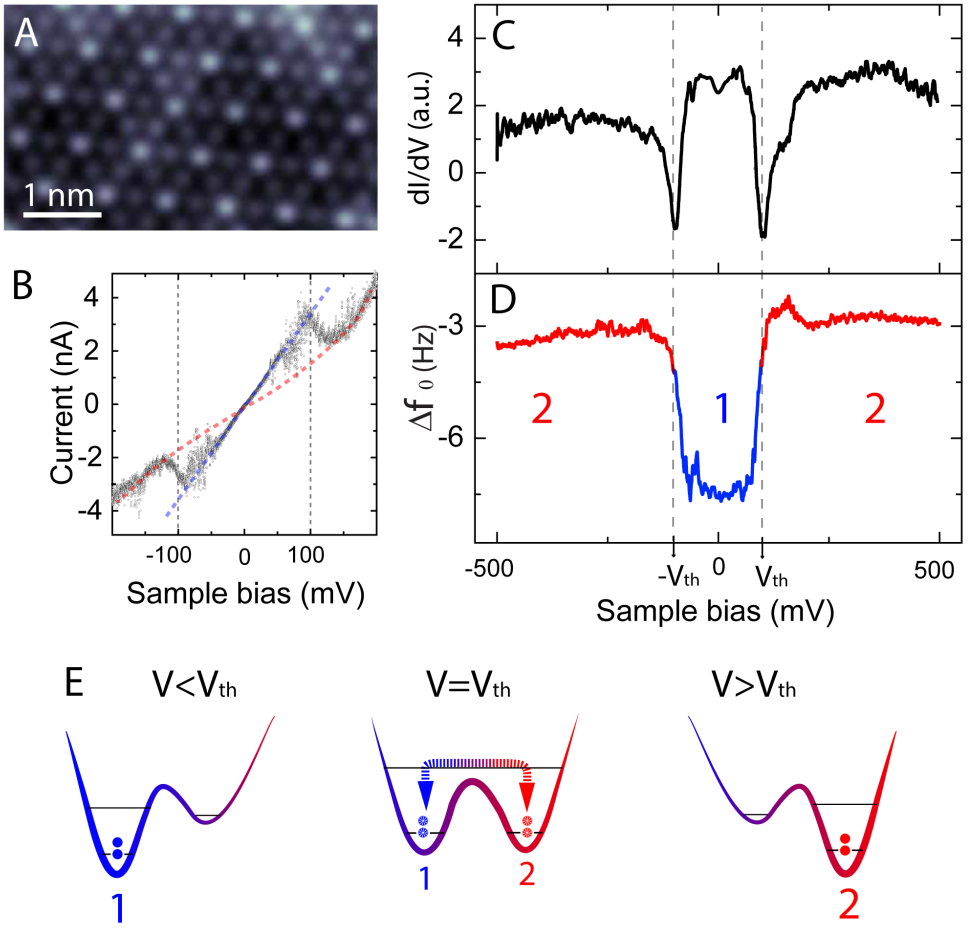

Figure 3.2.: (A) STM image of an hexagonal H_2 layer on Cu(111) (V_s= -37 mV, I_t= 200 pA), [117]. Bias spectra of the (B) tunneling current and (C) differential conductance on a Cu(111) surface with sub-monolayer H_2 coverage. The current spectrum shows two conductance regimes (marked with dashed lines) and an increased noise in the transition bias between them, at $V_{th}\sim \pm$ 100 mV. The dI_t/dV_s spectrum shows dips with negative differential conductance at the bias values $\pm V_{th}$, indicating the onset of vibrationally-induced fluctuations of a H_2 molecule between two configuration in the junction. (D) Simultaneously acquired frequency shift of the qPlus force sensor (A_{osc}= 50 pm, f_0 = 20.609 kHz). Different frequency shift above and below V_{th} reveal two states with different interaction with the STM tip. (E) Model of the bi-stable potentials and the vibrational TLFs of a H_2 molecule in the tunnel junction.

conductances. These fluctuations led to sharp dips of negative differential conductance dI_t/dV_s at the threshold bias $\pm V_{th}$ (Fig. 3.2C), which indicate the point where the stability of the two states was reversed [109]. The symmetric alignment of V_{th} with respect to zero bias is a fingerprint of a vibrationally activated process [122, 123]. In fact, the strong spectral non-linearities of a H_2 junction can be well modeled by vibrationally activated two-level fluctuations (TLFs) of the molecule between two adsorption configu-

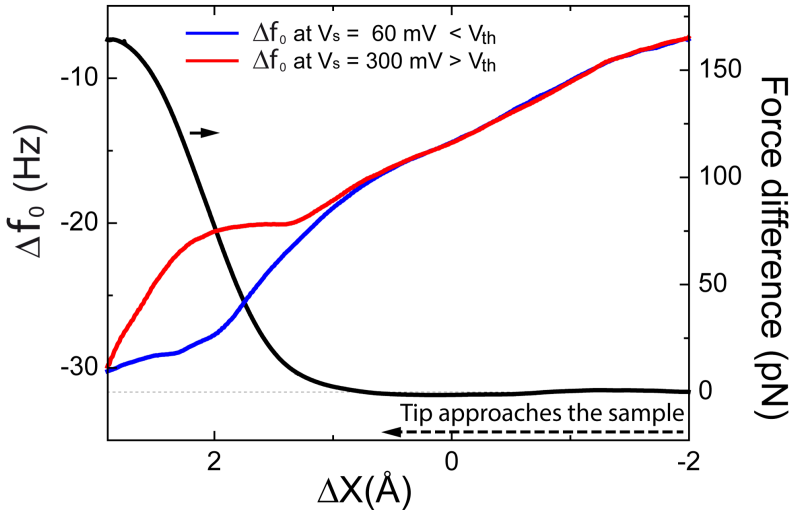

Figure 3.3.: Plot of frequency shift vs. tip approach distance measured at sample bias above (red) and below (blue) the threshold bias separating the two force regimes. The two plots show a marked difference when the tip approaches to short distances from the sample. We interpret these differences as two different force fields with distinct force gradients. The black curve plots the integrated difference in force gradients and, thus, it represents the magnitude of force difference between the two regimes.

rations [116, 118, 119].

The qPlus sensor allows us to measure its resonance frequency f_0 simultaneously with a differential conductance spectrum. Forces in the tunneling junction shift the resonance frequency by an amount Δf_0. In the limit of small tip oscillation amplitudes A_{osc} (sub-Ångstrom in our experiments) and conservative forces, Δf_0 is proportional to the gradient of the vertical forces in the tunnel junction [21], i.e. the stiffness of the junction. Figure 3.2D shows the Δf_0-V_s spectrum measured simultaneously with the spectra of Fig. 3.2B and 3.2C. The presence of H_2 induced a step-like anomaly at the threshold values $\pm V_{th}$. The steps of Δf_0 revealed that there are two bias regimes of different junction stiffness (labeled 1 and 2 in Fig. 3.2D), each associated to a different molecular configuration in the junction. Assuming that forces are conservative far from V_{th}, the larger negative value of the frequency shift (e.g. for the low bias state 1) is symptomatic of a larger attractive force.

3.1.1. The Force of a Hydrogen Molecule

We estimated the difference in force between the two states $\Delta F = F_2 - F_1$ by integrating their corresponding Δf_0 difference along the vertical direction X. Figure 3.3 compares two plots of Δf_0 as a function of the tip displacement ΔX. Before starting the tip approach at $\Delta X = -2$ Å, the bias is adjusted to 60 mV (blue) and 300 mV (red), values far from the bias threshold V_{th}=150 mV. Both $\Delta f_0 - \Delta X$ plots coincide at larger tip-sample

separations in a smooth negative Δf_0 background. This background is due to long-range attractive forces (van der Waals and electrostatic) between the mesoscopic tip apex and the surface. At close distances, however, the plots deviate from the smooth background in a different manner. For V_s<V_{th} (regime 1) the frequency shift increases more steeply. We attribute this to the presence of short-range attractive forces. For V_s>V_{th}, the frequency shift tends to decrease, denoting a slight compensation of the background attractive forces. We estimate the force difference between the two states $\Delta F = F_2 - F_1$ by deconvoluting both Δf_0 signals using the method by Sader and Jarvis [41] and integrating their difference along the tip-sample distance X. ΔF grows as the tip approaches, reaching more than 150 pN at the closest position inspected.

3.1.2. Distance Dependence of H_2 molecular TLFs

At the transition bias $\pm V_{th}$, stochastic fluctuations between the two molecular states [109] would inevitably result in fluctuations of the force sensed by the tip. Because the amplitude of the fluctuations is ΔF, their effect on the tip motion became more important as the tip approaches.

Figure 3.4 shows the evolution of conductance and Δf_0 spectra as the STM tip approached $\Delta X = 1.5$ Å toward the surface, with respect to an initial position with junction conductance of 5 nS. The set of spectra shows a monotonous decrease of the bias V_{th} with tip approach [109]. This evidences that the narrowing of the junction and the increase of the electric field reduce the energy required for driving the TLFs [124]. This effect turned out to be crucial because it caused the periodic motion of the tip at $V_s \sim V_{th}$ to change the relative stability of the two H_2 states. At approach distances $\Delta X > 0.75$ Å the negative dI_t/dV_s dips became more pronounced (Fig. 3.4, A and B) and the Δf_0 signal exhibited sharp peaks at the same bias value (Fig. 3.4, C and D).

3.1.3. Effect of TLFs on the Dissipation

The stochastic switching of H_2 in the vicinity of the threshold voltage makes the forces non-conservative and non-linear. To resolve their effect on the tip oscillation, we analyzed the mechanical energy dissipated during the tip oscillation. This magnitude captures the effect of non-conservative dynamics by tracking changes of the energy per cycle required to maintain a constant oscillating amplitude A_{osc}. In our experiment, this was quantified through the amplitude of the external signal required to drive the motion, A_D (ref. [21], details in sec 1.2.3).

The dissipation-bias spectrum of a H_2 junction shows pronounced minima at the bias $\pm V_{th}$ (Fig. 3.4E, F), that were absent on clean surfaces. The minima revealed that the H_2 fluctuations contributed to driving the motion of the tuning fork and diminished the demand for external driving. Most strikingly, the dips in the dissipation signal became gradually sharper as the tip approached the sample and reached negative values, as shown in Fig. 3.4, E and F, at $\Delta X > 0.75$ Å. A negative dissipation signal is a fingerprint of the system entering into a regime of self-oscillation (SO). Here, the phase of the external

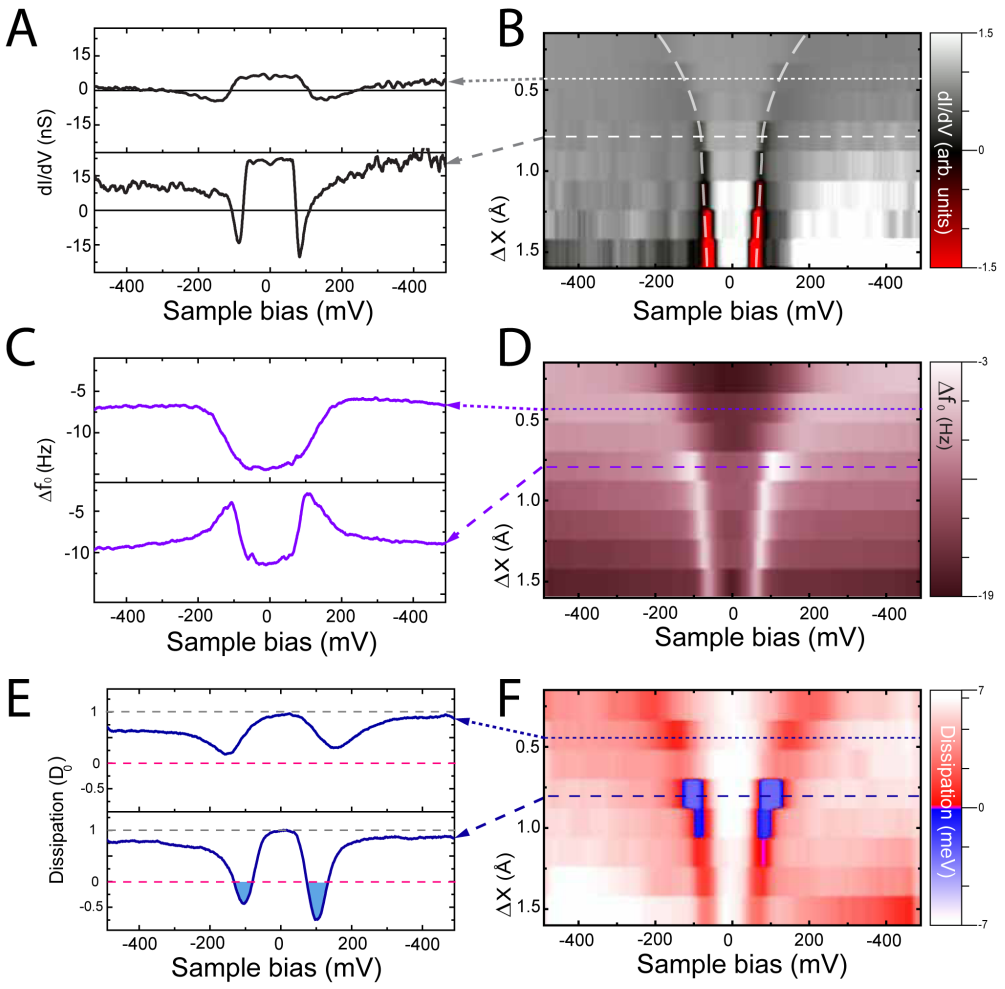

Figure 3.4.: Bias spectra of (A,B) the differential conductance, (C,D) the frequency shift, and (E,F) the dissipation signal of a H_2 molecular junction measured at eight different tip-sample distances. The color maps picture the corresponding magnitude vs. bias and approaching distance Δ X respects to an initial position with tunneling conductance 5 nS. The curved dashed lines in Fig. 3.4B indicate the reduction in the bias V_{th} with the tip-sample distance. The energy dissipation is monitored by the amplitude of the external signal driving the tip to oscillate with constant amplitude, and is plotted in units of the intrinsic dissipation of the free lever (measured previous to the experiments to amount $D_0 = 7$ meV/cycle).

driving signal is inverted with respect to the tip oscillation in order to counteract the growing amplitude of the tip motion. In this situation, the fluctuating H_2 molecule drives the motion of the tip-oscillator against the external load.

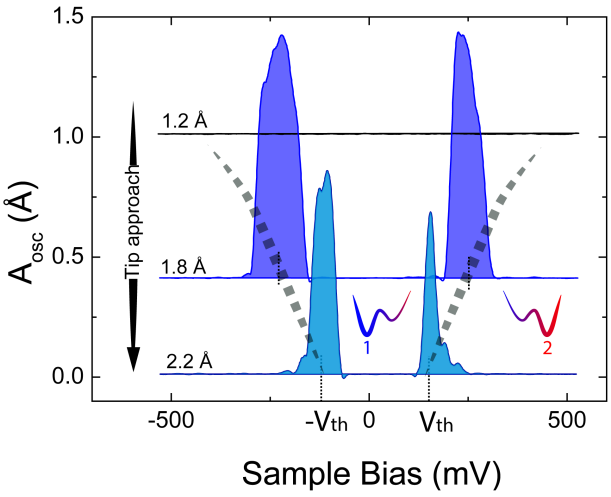

Figure 3.5.:
Oscillation amplitude A_{osc} vs. sample bias in the absence of external driving forces. Each spectrum is measured at the indicated approach distances with respect to an initial position at junction conductance 22 nS, and shifted to lower values for clarity. Peaks of tip oscillation signal A_{osc} are identified at $\pm V_{th}$. The dashed lines picture the gradual decrease of V_{th} with the tip-sample distance.

3.1.4. Self Oscillation of a Macroscopic Oscillator

Further proof that the tip SO was driven by fluctuations of a H_2 molecule could be obtained by measuring the bias dependence of the amplitude of tip oscillation A_{osc} in the absence of any external driving force (A_D=0 mV). Figure 3.5 shows that A_{osc} was zero for most bias voltages, except near the threshold bias V_{th}, where the tip started to self-oscillate with A_{osc}~1 Å. As in Fig. 3.4, the value of V_{th} decreased with the tip approach and the SO regime appeared for junction conductances of the order of 10 nS. In certain cases, the SO amplitude could reach several Ångstroms - i.e., greater than the size of H_2. These results demonstrate that the local forces associated with the electron-induced fluctuations of the H_2 molecule were remarkably efficient in driving the motion of the macroscopic oscillator. These forces compensated the intrinsic energy dissipation of the tuning fork (for the case of Fig. 3.4, ~ 7 meV/cycle) by providing mechanical energy of tens of millielectronvolts per cycle.

Figure 3.6 shows spectra of a H_2 junction obtained by allowing only positive values of the driving signal ($A_D > 0$). The self oscillation of the tuning fork at $\pm V_{th}$ causes the suppression of A_D near this bias (shown in Fig. 3.6A converted to applied power $D = D_0 \frac{A_D}{A_D^{free}}$) and the increase of the oscillation amplitude beyond the 50 pm setpoint. The tip reaches oscillation amplitudes of more than 1.5 Å driven solely by the fluctuation of the H_2 molecule. The driving power produced by the fluctuation of the H_2 molecule can be estimated using the expression $D_{H_2} = \frac{\pi k}{Q} A_{osc}^2 - D$ (see sec. 1.2.3, [21]), which is plotted in Fig. 3.6C. The H_2 molecule produces more than 50 meV per cycle, a factor of ten larger than the intrinsic dissipation of the tuning fork (at $A_{osc} \sim 50$ pm).

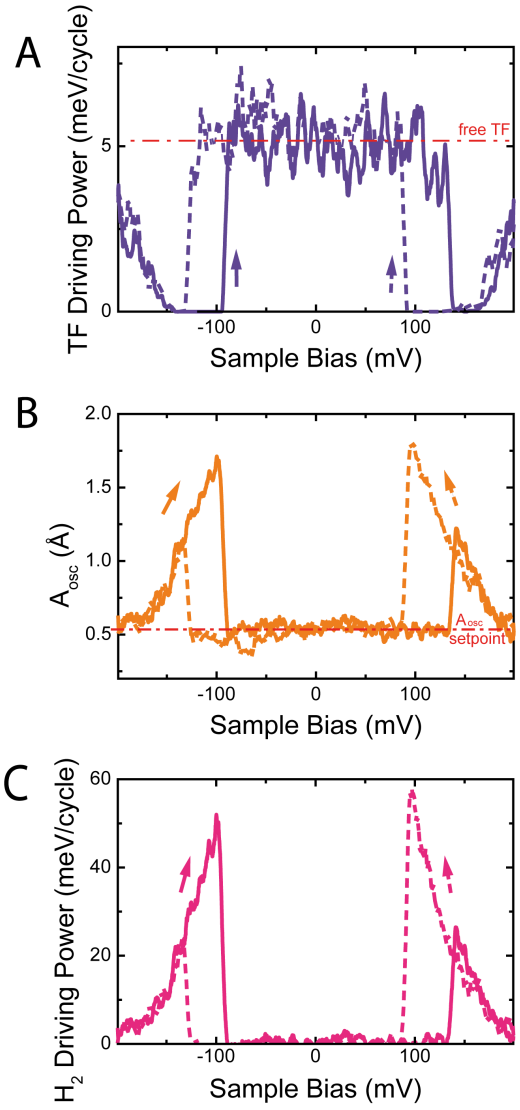

Figure 3.6.:
Bias dependence of (A) the driving power (obtained from A_D, using the method described in the text) and (B) the amplitude of tip oscillation for a H_2 junction. During the acquisition only positive values of the driving amplitude were allowed. This results in an increase of A_{osc} beyond the setpoint value of 50 pm when the self-oscillation appears, around V_{th} ($f_0 = 23.920$ kHz). (C) Plot of the corresponding power generated by the H_2 molecule to drive the tuning fork self oscillation. The spectra show a pronounced hysteresis because the increase in oscillation amplitude also affects the onset for TLFs.

3.2. Theoretical Modeling and Interpretation of the Self Oscillation

Current-induced TLFs are stochastic in nature, so that the corresponding force fluctuations acting on the cantilever have a broad power spectrum in the frequency domain. When the power spectrum has appreciable weight near the resonance frequency of the cantilever, the force fluctuations can resonantly excite the oscillator to reach a stationary state. In the limit of a weakly damped oscillator $Q \gg 1$ one can show that the amplitude becomes

$$\langle (X(t))^2 \rangle \simeq \frac{\Delta F^2}{8\omega_0^2 \gamma M^2} \frac{2\Gamma_2\Gamma_1/(\Gamma_2+\Gamma_1)}{\omega_0^2 + (\Gamma_2+\Gamma_1)^2}, \tag{3.1}$$

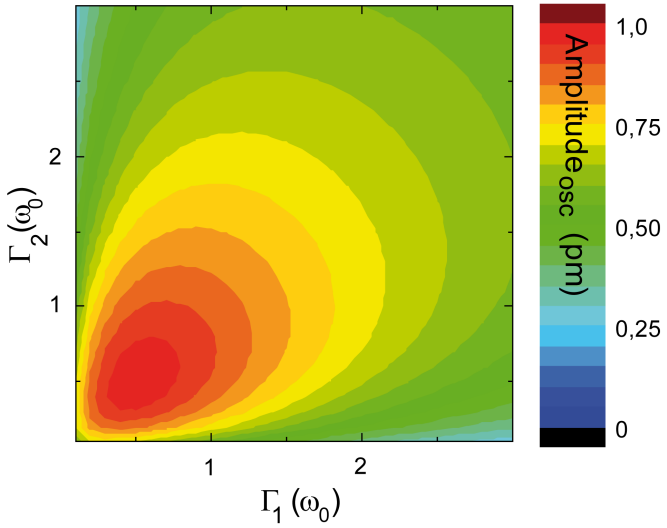

Figure 3.7.:
Plot of the amplitude of oscillation as a function of the rates of molecular motion out of state 1 and 2, Γ_1 and Γ_2, respectively, following equation 3.1. The maximum oscillation occurs for $\Gamma_{1,2} = \omega_0/2$.

where Γ_i denotes the inverse dwell times of the H_2 molecules in the states $i = 1, 2$. The amplitude $\langle (X(t))^2 \rangle^{1/2}$ is plotted in Fig. 3.7 as a function of Γ_1 and Γ_2. It has a maximum for $\Gamma_1 = \Gamma_2 = \Gamma/2$ and $\Gamma = \omega_0$, with $\Gamma = \Gamma_1 + \Gamma_2$. Under optimal conditions, this mechanism causes an oscillation amplitude of the order of

$$\langle (X(t))^2 \rangle^{1/2} \simeq |\Delta F|/4\sqrt{2}\omega_0^{3/2}\gamma^{1/2}M. \tag{3.2}$$

Using the values of our experimental set-up ($\Delta F = F_2 - F_1 \sim 100$ pN, and $\gamma \sim 10s^{-1}$, $\omega_0 \sim 10^5 s^{-1}$, and M$\sim$ 0.1 mg for the intrinsic damping coefficient, resonance frequency and mass of the cantilever, respectively) we obtain oscillation amplitudes of the order of 1 pm, far smaller than the values observed in our experiment.

3.2.1. Stochastic Resonance and Self-Oscillations

To explain the experimental results, a crucial aspect must be considered: the switching rates between the two molecular states depended on the distance between tip and surface, i.e., they were tuned by the periodic oscillation of the tip. There are two possible causes for this: i) the tunneling current and, with it, the switching rates varied with tip-substrate distance; ii) at fixed bias, the tip displacement $X(t)$ shifted the threshold bias V_{th} and, hence, the relative stability of the two states [109]. This last effect turned out to be crucial because it changed the switching rates Γ_1 and Γ_2 in opposite directions (described in Fig. 3.8B) and caused an appreciable modulation of the occupations $n_1(t)$ and $n_2(t)$ of the two switching states of H_2 with the periodic motion of the tip.

The effect of the force modulation $F(t)$ can be described analytically when assuming a linear variation of the switching rates Γ_i with cantilever displacement $X(t)$ (valid for small displacements),

$$\Gamma_i(t) \simeq \Gamma_i + \Gamma_i' X(t), \tag{3.3}$$

where $\Gamma_i' = d\Gamma_i/dX$. This yields a Markovian Master equation with oscillatory switching rates, a problem which is known in the literature as *stochastic resonance* [114].

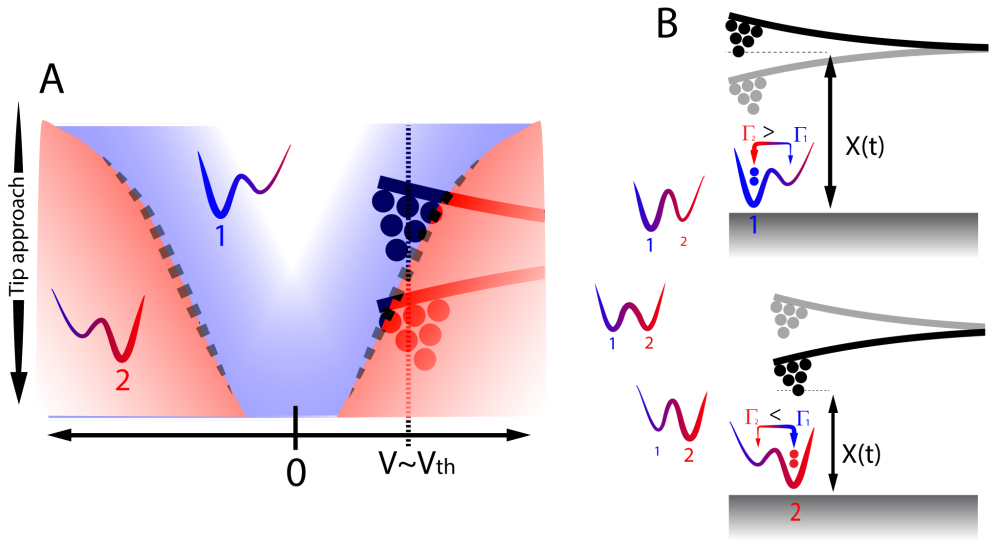

Figure 3.8.: Sketch of the concerted dynamics of H_2 molecule fluctuations and tip periodic motion. (A) Bias-distance phase diagram of the population of the two states of the hydrogen molecule, summarizing the behavior depicted in Fig. 3.4. The tip motion at a bias V_{th} drives the system from the more attractive state (1) to the more repulsive state (2). (B) Diagram illustrating the tuning of the bi-stable potential of the H_2 molecule by the tip oscillation. When the tip is close (far), the state 2 (1) is more stable, and the rate Γ_2 (Γ_1), the switching out of state 2 (1), smaller. The switching rates Γ_2 and Γ_1 have the opposite behavior with the tip distance X(t).

Remarkably, we found that by this mechanism the average force $\langle F(t)\rangle$ acquired components proportional to the tip's displacement $X(t)$ and to its velocity $\dot{X}(t)$, which affect the renormalizations of both, the restoring force and the friction coefficient of the cantilever. The former merely caused a shift in the resonance frequency of the tip's oscillation, thus accounting for the Δf_0 peaks observed in our experiments at V_{th}(Fig. 3.4C,D). The most interesting prediction of this feedback model comes from the renormalization of the damping coefficient, so that the cantilever becomes subject to the effective damping coefficient

$$\gamma_{\text{eff}}(\omega) = \gamma + \frac{(\Delta F)}{M}\frac{\Gamma_2'\Gamma_1 - \Gamma_1'\Gamma_2}{2\Gamma}\frac{1}{\omega^2+\Gamma^2}. \tag{3.4}$$

Indeed, the second term of the right-hand side of eq. 3.4, the switching-induced "dissipative" contribution to the damping, is *negative* in our setup. We define X such that it increases with increasing tip-sample distance. The cantilever is attracted to the sample, so that $F_1, F_2 < 0$. Experimentally (Fig. 3.3) we found the force in the H_2 low voltage state 1 larger in magnitude, so that $\Delta F = F_1 - F_2 < 0$. Since the low voltage state 1 is more stable at larger X (as illustrated in Fig. 3.8A), we conclude that $\Gamma_2' > 0$ and $\Gamma_1' < 0$.

When this current-induced "dissipative" force overcompensates the intrinsic damping γ, the cantilever equilibrium position ($\langle X\rangle$ in absence of switching) becomes unstable and the overall renormalized damping γ_{eff} becomes *negative*. In line with the experimental observations, this is most likely to occur when the cantilever frequency ω_0 is of the

order of the total switching rate Γ. In fact, we estimated that the switching induced renormalization of the damping coefficient was of the order of $\Delta\gamma_{\text{eff}} \sim -10\ \text{s}^{-1}$ which could overcompensate the intrinsic friction $\gamma \sim 10\ \text{s}^{-1}$ of the high-Q cantilever and cause overall negative friction. In this case, the equilibrium position of the oscillator would become unstable, entering into self oscillations.

The conditions for reaching the regime of negative friction are a set of switching rates Γ_i not too different from ω_0, and a modulated force $F(t)$ that becomes less attractive (or more repulsive) at the closest tip position $X(t)$. This condition was fulfilled in the H_2 molecular junction for bias values near V_{th}. Because of the monotonous reduction of V_{th} with the tip-surface distance, the state with a less attractive force (regime 2) became more frequent in the part of the cycle with smaller tip-sample distances (Fig. 3.8).

In the regime of SOs, the oscillation amplitude was ultimately controlled by nonlinearities of the restoring forces. The stationary limits for the oscillation amplitude are $A = 0$ and

$$A = \left(\frac{4\delta\omega_0}{3\alpha}\right)^{1/2} \tag{3.5}$$

where α is the nonlinearity parameter of a cubic Duffing force and δ the *negative damping coefficient*. The nonlinearities are dominated by the tip-substrate forces rather than the intrinsic nonlinearities of the oscillator, as we could show (appendix B). We estimate the nonlinearity parameter

$$\alpha \sim \frac{\text{typical force}}{\text{typical mass} \cdot (\text{typical length})^3} \sim 10^{24}\ \text{N}/(\text{kg m}^3), \tag{3.6}$$

where we assume 100 pN for the typical force, M∼0.1 mg and the typical length scale on the order of 1 nm. If we assume that the negative damping is of the same order as the positive intrinsic damping of the cantilever, i.e. $\delta \sim 10\ \text{s}^{-1}$, and use the resonance frequency $\omega_0 \sim 10^5 \text{s}^{-1}$, we find the amplitude of the self-oscillations to be of the order of ~ 1 nm, consistent with our experimental observations.

3.3. Conclusion and Outlook

Despite the large difference in mass and size, the motion of H_2 molecule and tuning fork require similar energies due to the high quality factor of the qPlus sensor. Therefore, the tens of millielectronvolts involved in the H_2 switching were sufficient to feed an oscillation cycle of the tip with amplitudes of Ångstroms. However, the incoherent character of the random energy source usually would inhibit an efficient energy transfer to the oscillator. Here, the stochastic resonance played a crucial role. The concerted dynamics of molecular bi-stability and tip oscillation created a coherent pathway for transferring energy from the noisy source into the periodic motion. In this case, the harvested energy originated from inelastic tunneling of electrons. Such a mechanism might also generalize to other energy sources or more complex molecular junctions [9, 10, 125–128]. We envision that appropriately designed intrinsic mechanisms of SR feedback could be a way for

enhancing the energy transfer in molecular motors transforming Brownian motion into directional motion.

Chapter 4.

(Dis)Charging of Charge Transfer Complexes Investigated by NC-AFM

Atomic force microscopy is sensitive to forces on the atomic scale. It is for instance possible to determine the charge state of individual atoms [23]. The charge redistribution induced by noble metal adatoms adsorbed on NaCl/Cu(111) has shown to modify the local electrostatic potential ($LCPD$) in a way, that the measured electrostatic potential shifts to smaller (larger) values, if the atomic charge is positive (negative). Gross *et al.* observed also a larger attractive force at the sample bias V_s matching the $LCPD$ when atoms were charged by one electron or hole, compared to the respective uncharged atoms. The latter effect they ascribed to an induced charge in the tip, originating from an ionic or anionic metal adatom (see sec. 1.2.6) [51].

In chapter 3 we showed that the stochastic motion of a hydrogen molecule can drive the motion of the macroscopic AFM tuning fork. The fluctuations between two different states of the H_2 molecules, associated each with a different tip-molecule force, couple resonantly with the motion of the tuning fork and lead to a self-maintained concerted motion with negative dissipation. Tekiel *et al.* observed that the quantized charging of nanoscopic quantum dots leads to dissipative interaction with the tip of a dynamic force microscope [129]. A bias voltage, applied between the tip of an AFM and a Fe surface led to charging and discharging of Au nanoparticles on an insulating NaCl film in between tip and surface, in concert with the tip motion. The charging and discharging occurred through electron tunneling between the Au nanoparticle and the Fe surface. Due to the NaCl film, the tunneling rate was greatly reduced, compared to nanoparticles adsorbed directly on a metal substrate. In this way they could tune the tunneling rate by the applied bias and tip-sample distance to values in the order of the cantilever resonance frequency and observed a maximum in the damping of the cantilever motion when the tunneling rate was matched with the cantilever resonance frequency.

In this chapter we show that the charging and discharging of a single molecule can couple to the motion of an AFM tuning fork. The electron acceptor molecule TCNQ embedded into a charge transfer compound could be (dis)charged by integers of e through gating with the electric field between an STM tip and the surface [130]. Here, the critical field determining the molecular (dis)charging could be tuned with the sample bias voltage or the tip-molecule distance. The latter changes periodically at an oscillating AFM tip. By coupling of the (dis)charging resonantly with the motion of the AFM tip, we

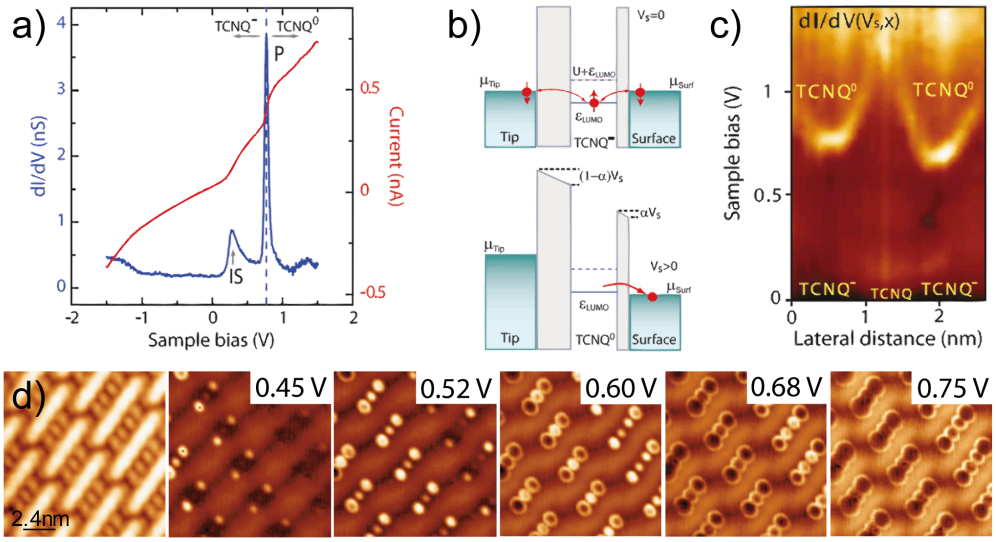

Figure 4.1.: Gating the charge state of TCNQ molecules embedded in TMTTF-TCNQ domains (Figures from Torrente *et al.* [130]). **a)** dI/dV spectrum taken on a TCNQ molecule: the sharp resonance 'P' indicates the discharging of the singly charged $TCNQ^-$ into a neutral $TCNQ^0$. The peak in the dI/dV curve indicated '*IS*' is due to a molecular interface state. **b)** Double barrier tunneling junction (DBTJ) model of the discharging process: a fraction αV of the electric potential drops in the TCNQ-surface interface. In the singly charged $TCNQ^-$ a single electron charge resides on the TCNQ molecule. With applied external electric field, the molecular orbitals, e.g. the SOMO, shift also with respect to the surface chemical potential, as sketched in the lower image. When the SOMO is lifted above the surface Fermi level it is emptied and the molecule becomes neutral. This reduces the blockade of the current, giving rise to a step-like increase in the tunneling current and a peak in the dI/dV (fig. a). **c)** Spectral map of a series of dI/dV vs. V_s and $lateral\ distance$ spectra. As the tip approaches the center of a molecule, the discharging peak '*P*' shifts to lower sample bias. **d)** Constant current dI/dV maps at different bias voltages show the 2d lateral evolution of the discharging equipotential contour.

hoped to find an influence on the dissipation of the AFM tuning fork.

Indeed we find and characterize an effect of the dynamic (dis)charging of molecules on the measured Δf. We can not observe any (dis)charging related dissipation between tip molecule. We attribute this to the (dis)charging process being too fast. Extensive Δf and dI/dV spectroscopy mapping will help us to reveal a *mutual charge gating* effect between neighbor molecules.

4.1. Gating the Charge State of Single Molecules by Local Electric Fields

In a recent study, Torrente *et al.* [130] found that the electron acceptor molecule tetracyanoquinodimethane (TCNQ) mixed with the electron donor molecule tetramethyltetrathiafulvalene (TMTTF) forms a charge transfer complex with an interesting distance- and sample bias-dependent (dis)charging behavior. Here we investigate the (dynamic) behavior of this charging effect by dynamic force microscopy.

Co-deposition of both species on a Au(111) surface leads to stoichiometrically ordered (1:1) islands. A high degree of charge localization on the TCNQ molecules can be observed, leaving the TCNQ in different ground states with integer charge occupation: either anionic (called 'type I') or neutral ('type II'). Figure 4.1 a) shows a spectrum of dI/dV and tunneling current versus sample bias of an anionic molecule (from Torrente *et al.*: [130]). The anionic ground state was determined by the existence of a zero-bias peak (ZBP, not shown here) in the $dI/dV(V_s)$, an indication for the Kondo effect, revealing the singly occupation of the lowest unoccupied molecular orbital (LUMO). Peak '*P*' in figure 4.1 a) indicates a discharging of the anionic molecule. Its energetic position shifts to lower values as the distance to the molecule is reduced and the electric field at the molecule increases (fig. 4.1 c).

Torrente *et al.* explained this behavior with a double barrier tunneling junction (DBTJ) model (figure 4.1 b). In the TMTTF-TCNQ charge transfer complex, the TCNQ is decoupled electronically from the surface in a way that a fraction αV_s of the applied bias V_s drops between the TCNQ molecule and the gold surface. This allows the molecular levels (e.g. the SOMO) to shift by an amount of αV_s with respect to the Fermi level of the surface. When a sufficiently high positive bias voltage is applied to shift the SOMO of the anionic TCNQ molecules above the surface Fermi level, the SOMO is emptied and the molecule becomes neutral. This sudden discharging produces a step-wise increase of the tunneling current (figure 4.1 a) and as a result the sharp peak '*P*' in the dI/dV spectrum.

Figure 4.1 c) shows spectral dI/dV vs. V_s, *lateral distance* maps. The parabola-like bright lines correspond to the position of the discharging peak '*P*' in fig. 4.1 a). When the tip-molecule distance increases also the bias voltage needs to increase to maintain the electric field that is required for the molecular discharging. Figure 4.1 d) shows constant current maps of the differential conductance at different sample bias. The elliptic contours around the TCNQ molecules correspond to the position of the discharging peak '*P*' as the tip approaches the molecules and the electric field increases. Both show that the charge state can be modified by a change of the sample bias or by changing the tip-sample distance. In this way one can picture the control of the charge state by tuning the tip-molecule distance in analogy to the gate electrode in a three-terminal quantum dot device [131].

On the type II TCNQ molecules, those being in a neutral ground state, a charging dip in the $dI/dV(V_s)$ was observed at negative sample bias. By the charging, an interface dipole is created by the anion and its image charge. This results in an increase of the local work function and blockades partially the tunneling current, giving rise to a dip in the

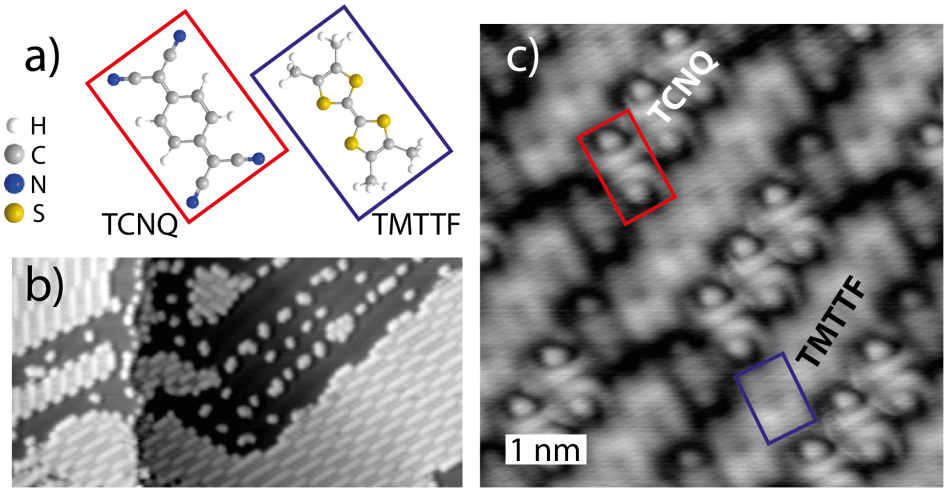

Figure 4.2.: a) Molecular structure models of TCNQ (acceptor) and TMTTF (donor). The colored boxes are used to identify the single molecules in the STM image. **b)** STM topography overview image of the charge transfer complex TMTTF-TCNQ on Au(111). ($V_s = 0.71$ V, $I_t = 95$ pA) **c)** Detailed STM topography image with functionalized tip. The colored boxes indicate single molecules (see also a), red: TCNQ, blue: TMTTF) within the molecular islands. The shape of the TCNQ molecules resembles the lowest unoccupied molecular orbitals of TCNQ. ($V_s = 1.2$ V, $I_t = 140$ pA)

differential conductance. The general observations concerning the AFM measurements are similar for type I and type II TCNQ molecules, so we focus later mainly on type I molecules.

The dependence of the (dis)charging on the electric field results in a very sharp defined onset of the effect with respect to the tip-sample distance, as seen in the dI/dV spectral maps and the constant current dI/dV maps figure 4.1 c) and d). In the following experiments we will investigate the bias-induced discharging by means of combined STM and dynamic force microscopy.

4.2. TMTTF-TCNQ (Dis)Charging Investigated by Dynamic AFM

The electron acceptor tetracyanoquinodimethane (TCNQ) mixed with the electron donor tetramethyltetrathiafulvalene (TMTTF) forms, upon adsorption on a Au(111) surface, a two-dimensional charge-transfer complex, comparable to the prototype charge-transfer compound TTF-TCNQ [132]. Structural models of the two molecules are shown in figure 4.2 a). TMTTF is a methylated TTF molecule, thus reducing the interaction with the substrate compared to the compound TTF-TCNQ [133]. TMTTF and TCNQ were evaporated from Knudsen cells held at 63 °C and 101 °C, respectively, onto the sample at room temperature

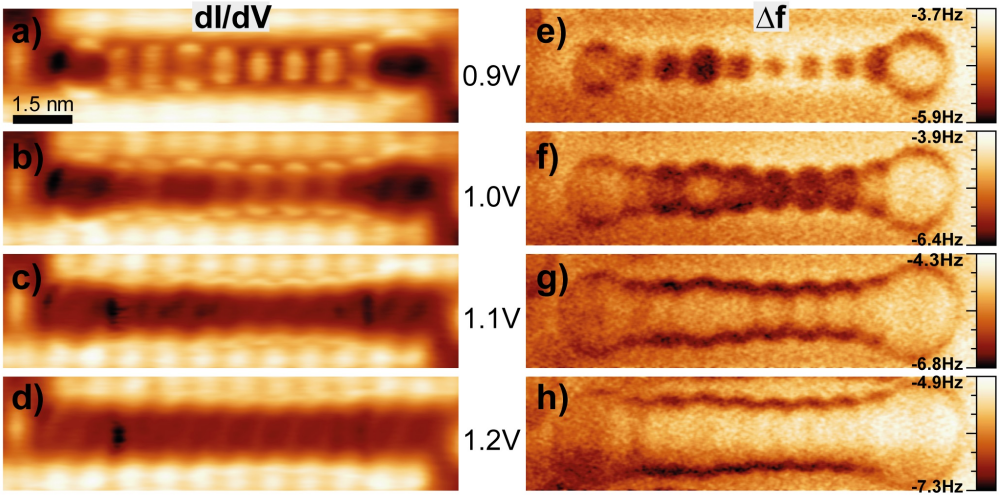

Figure 4.3.: Type I $TCNQ^-$ chain. **a) - d)** Constant height dI/dV maps at different sample bias voltages, as indicated. **e) - h)** Constant height Δf maps, recorded simultaneously with the maps a) - d). (tunneling setpoint: $V_s = 0.75$ V, $I_t = 250$ pA)

STM images of self-assembled TMTTF-TCNQ islands are shown in figure 4.2 b) and c). The red and blue frame in the high resolution STM image 4.2 b) indicate the structure, that can be assigned to an individual TCNQ and TMTTF molecule, respectively. The STM images picture the $TCNQ^-$ molecules with the shape of the lowest unoccupied molecular orbital (LUMO), a nodal planes appears at the center and two maxima at each of the C-$(cyano)_2$ sides. Molecular islands consist of alternating rows of TMTTF-TCNQ maintaining a 1 : 1 stoichiometry.

4.2.1. Spectroscopic Imaging of $TCNQ^-$ Molecules

In order to investigate the charging we recorded constant height maps at different sample bias voltages of both, differential conductance and frequency shift. Figure 4.3 a)-d) shows dI/dV maps on a type I $TCNQ^-$ molecular chain at different sample bias voltages. We can identify the elliptic contours of the discharging around the molecules and observe their evolution to larger perimeters at higher V_s.

Figure 4.3 e)-h) show the frequency shift signal, recorded simultaneously with the maps a)-d). Also here we observe elliptic contours around the molecules, evolving to larger perimeters for higher sample bias. The correlation between the Δf and the dI/dV iso contour lines shows that the contours in the Δf maps are indeed due to the discharging of the $TCNQ^-$ molecules.

In figure 4.3 g), h) we see that the discharging rings exhibit a more negative frequency shift at the contour line, while inside the ring the frequency shift values are comparable to outside the charging region. This is in contrast to the observations of Gross *et al.* [23] for Au and Ag adatoms on NaCl. They observed a significant shift of the $\Delta f(V_s)$ parabola

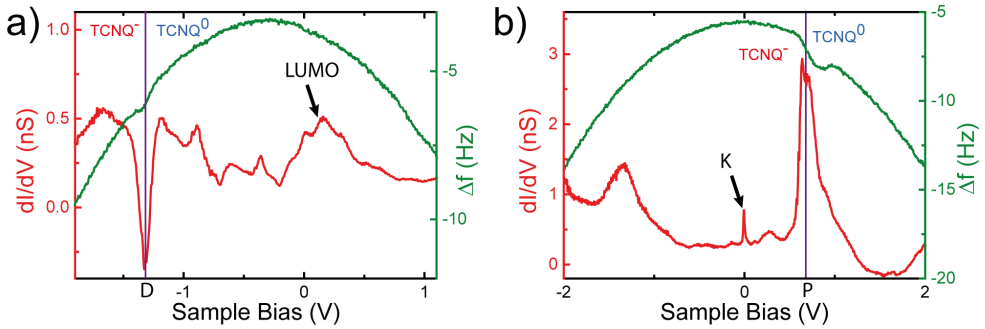

Figure 4.4.: Correlation between $dI/dV(V_s)$ and $\Delta f(V_s)$ spectra. **a)** $dI/dV(V_s)$ and $\Delta f(V_s)$ spectra measured simultaneously on a type II $TCNQ^0$. The LUMO is found above the Fermi level, the molecule is in a neutral ground state. The dip in the dI/dV at 'D' is due to the charging of the initially neutral TCNQ at bias voltages $V_s \leq D$. In the Δf parabola a nonlinearity - a dip - can be observed at 'D'. ($V_s = 0.74$ V, $I_t = 274$ pA) **b)** $dI/dV(V_s)$ and $\Delta f(V_s)$ spectra of a type I $TCNQ^-$ molecule. The discharging peak at 'P' goes with a dip in the $\Delta f(V_s)$ curve. An additional zero bias peak labelled 'K' identifies this molecule as a singly charged type I $TCNQ^-$. ($V_s = 0.60$ V, $I_t = 300$ pA) Both spectra were measured with different tips, thus the $LCPD$ positions (the sample bias where $\Delta f(V_s)$ has a maximum) cannot be directly compared.

(along V_s but also a shift of the parabola maximum at $V_s = LCPD$ to lower Δf) when an atom was charged by an electron (Au) or hole (Ag), compared to the respective neutral atom (see also sec. 1.2.6). The discharging of a $TCNQ^-$ molecule should lead to different electrostatic forces, thus a change of the frequency shift all over the area within the discharging contour. So the observed Δf decrease is more related to the discharging event, but not to the charge state itself. We will understand the cause for the Δf decrease on the discharging contours after the following experiments.

At certain (bigger) sample bias voltages (figure 4.3 c) and g) the contour lines of neighbor molecules overlap in the dI/dV and Δf maps. An overlapping means that at those points the electrostatic potential is the same for the discharging of two neighboring molecules, which will give rise to phenomena of mutual molecular influence.

4.2.2. Correlation of Discharging Features in Conductance and Frequency Shift Spectra

Figure 4.4 a) shows $dI/dV(V_s)$ and $\Delta f(V_s)$ spectra measured above a type II $TCNQ^0$ molecule. This molecule is in a neutral ground state [130], reflected in the LUMO level lying above the Fermi level. The dip in the dI/dV curve at negative bias, labelled 'D', indicates the charging of the molecule ($TCNQ^0 \rightarrow TCNQ^-$). At bias voltages below D the field shifts the LUMO level below E_F and allows for the charging.

We measured the frequency shift simultaneously with the differential conductance as a function of the sample bias voltage. The overall shape is parabolic, following the

expression $\Delta f \propto (V_s - LCPD)^2$, where $LCPD$ is the local contact potential difference (for details see sec. 1.2.5, 1.2.6, [134]). At a sample bias voltage of $LCPD$ the electrostatic forces in the junction are minimized. Thus, the $LCPD$ is related to the local electrostatic potential at the tip position caused by differences in the electrostatics properties of tip and sample (e.g. work function, dipole, charges). The presence of a positive (negative) charge underneath the tip shifts the $LCPD$ to more negative (positive) values. Also, the frequency shift at $V_s = LCPD$ decreases if more charge is localized below the tip [23].

Based on these arguments, the two charge states of TCNQ molecules should appear in figure 4.4 a) as two parabolas, side by side, with a transition between them at the charging voltage D. Indeed, we observe a dip in the $\Delta f(V_s)$ curve at $V_s = D$, which we interpret as originated by the alteration in the charge state. However, we do not directly see a significant change of the parabolas curvature or a significant shift of the curves to a different LCPD.

A similar behavior occurs for type I $TCNQ^-$ molecules, shown in figure 4.4 b). A peak in the dI/dV, denoted 'P' indicates the discharging of the $TCNQ^-$ ground state ($\rightarrow TCNQ^0$). The peak is also correlated with a dip in the simultaneously measured $\Delta f(V_s)$ curve, but no obvious deviation between the two sides of the parabola, left and right from 'P', can visually be observed. The feature in the dI/dV spectrum labelled 'K' is a zero bias peak due to the spin Kondo effect, thus confirming the singly charged ground state of this molecule.

The manifestation of the charging and discharging feature in the Δf spectra is a decrease in the frequency shift, in agreement with the elliptic contours around the molecules in the constant height Δf maps (figure 4.3 e)-h). In order to determine an effect of the charge state on the parabolic shape of the $\Delta f(V_s)$ curves we have to develop a fitting procedure. Later on we will also develop an interpretation of the physical origin to account for the dip in the frequency shift curve.

4.2.3. Identification of the Charge State by AFM

Since a single or even two parabolas can not fit the measured $\Delta f(V_s)$ spectra, nor the dip at the transition bias, we apply a phenomenological model to produce a fitting function that accounts for two charge states.

The basis of this fit function are two parabolas representing the different charge states. The whole fitting function, developed by Fabian Schulz in his master's thesis [135], is as follows:

$$\begin{aligned}\Delta f(V_s) = [A_0(V_s - V_{LCPD\ 0})^2 + C_0] \cdot \Theta_0(D_0(x - E_0)) + \\ + [A_-(V_s - V_{LCPD\ -})^2 + C_-] \cdot \Theta_{-1}(D_-(x - E_-))\end{aligned} \tag{4.1}$$

where A_n, $V_{LCPD\ n}$ and C_n are the parabola fitting parameters [curvature, horizontal position (=$LCPD$) and vertical offset (= Δf) due to non-electrostatic tip-sample forces].

In order to account for the dip when fitting the experimental $\Delta f(V_s)$ curve, we introduce broadened step functions Θ_n, plotted in figure 4.5 b). These take the value 1 or 0, at opposite sides from the discharging voltage (E_0, E_-) and multiply the respective

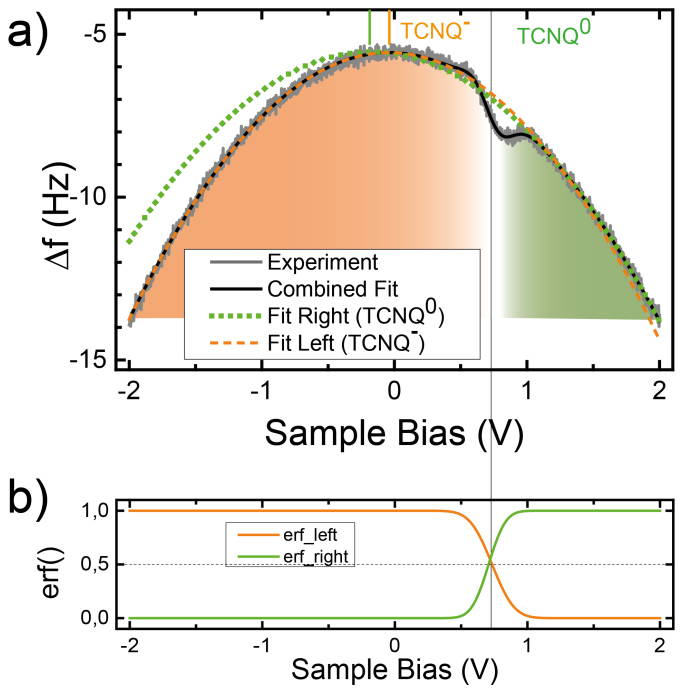

Figure 4.5.:
a) $\Delta f(V_s)$ spectrum of a type I $TCNQ^-$ molecule. Experimentally obtained data (gray line 'Experiment') and the corresponding fit from the fit model eq. 4.1 (black line 'Combined Fit'). The green dotted (orange dashed) line corresponds to the single $\Delta f(V_s)$ parabola of the neutral (anionic) TCNQ molecule, as obtained from the fit. **b)** Broadened step functions used in the fit function to account for the dip in the $\Delta f(V_s)$ curve.

fit-parabola. In a transition region through the discharging voltage, the broadening parameters D_n and the overlap E_n of the step functions account for the finite width of the discharging dip.

Figure 4.5 a) shows a measured $\Delta f(V_s)$ curve (gray, labelled 'Experiment') conducted on a type I TCNQ molecule. The curve was fitted with the fitting function eq. 4.1 (black line, labelled 'Combined Fit') which reproduced the experimental curve. From the fitting coefficients we obtain two individual parabolas, accounting for the two TCNQ molecular charge states. The green, dotted line represents the $\Delta f(V_s)$ parabola of the discharged type I $TCNQ^0$, while the orange, dashed line represents the singly charged type I $TCNQ^-$ molecule. From the fit we find that the $LCPD$ of the neutral $TCNQ^0$ molecule is lower (here by $\sim$ 140 mV, LCPD value indicated by the orange and green vertical line in fig. 4.5 a), which agrees with the expected direction of the $LCPD$ shift [23].

The frequency shift value at $LCPD$ of the singly charged $TCNQ^-$ molecule, obtained from the fit, is only about 20 mHz lower than the value of the neutral $TCNQ^0$ molecule. Also the lower $\Delta f(LCPD)$ due to a negative charge was expected [23].

With this phenomenological approach we could fit the experimentally obtained $\Delta f(V_s)$ curves and extracted the parameters (LCPD, Δf shift), which support the charge states of the TCNQ molecules.

4.2.4. Origin and Quantification of the Discharging Force

In order to understand the nature behind the dip in the $\Delta f(V_s)$ parabolas, we investigate the tip-sample distance dependence of the discharging feature with the oscillating

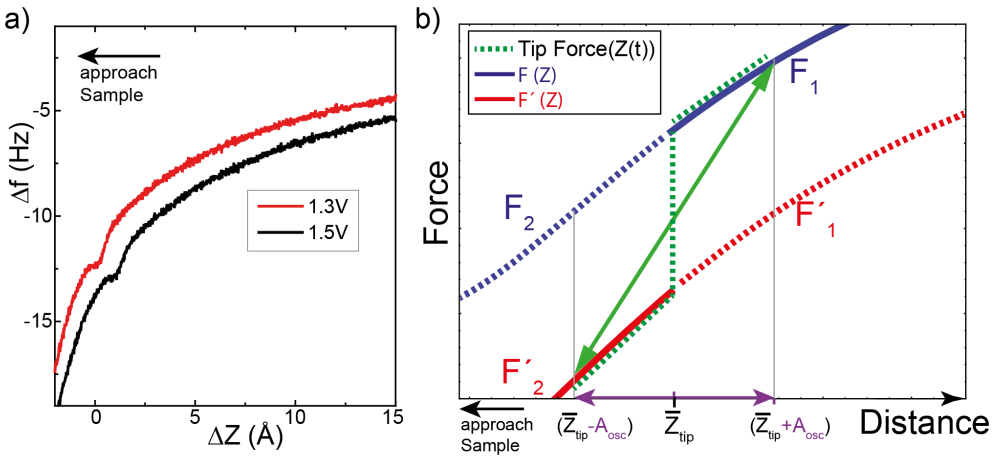

Figure 4.6.: a) Experimentally obtained Δf-Z distance curves (red and black) above a type I TCNQ molecule at different sample bias voltages. At larger sample bias voltage the position of the discharging dip shifts to higher Z values and the whole $\Delta f(Z)$ curve is shifted to more negative Δf values, due to the higher attractive electrostatic forces at $V_s = 1.5$ V, compared to 1.3 V. $\Delta Z = 0$ refers to the vertical position above the molecule with the tunneling setpoint $V_s = 0.75$ V, $I_t = 250$ pA. **b)** Sketch of two simulated Force-distance curves for differently charged samples, the sample is on the left hand side. The overall Force-distance slope is determined mainly by the Lennard-Jones force, the different charge state shift the curves force up or down on the Force axis.

AFM tip. Figure 4.6 a) shows two measured frequency shift-Z distance curves (red and black) measured at different sample bias voltages, 1.3 V and 1.5 V, above a type I TCNQ molecule. The Δf discharging feature appears also as a dip in the $\Delta f(Z)$ curve. From previous studies [130] and our observations in figure 4.3 we expected the discharging ($TCNQ^- \rightarrow TCNQ^0$) feature to appear at larger Z distances when a larger bias voltage is applied. We find this confirmed in figure 4.6 a). In addition, a larger applied bias of 1.5 V leads also to more attractive electrostatic forces between tip and sample and shifts the whole black curve to lower Δf values [136]. The full width of the discharging dip in the $\Delta f(Z)$ curves is about $\Delta Z = 1$ Å. This corresponds to the peak-to-peak amplitude of the tip oscillation. Thus, the discharging feature is related to the distance dependent discharging process coupled to the periodic vertical motion of the AFM tip in both, $\Delta f(V_s)$ spectra and $\Delta f(Z)$ approach curves.

In order to understand the origin of the Δf dip, we sketch a model in figure 4.6 b). Plotted are sections of two force-Z distance curves, simulated using the equation of an empirical Lennard-Jones potential (see sec. 1.2.4, [57]). The blue curve represents the molecule in one state, the red curve was offset vertically to simulate a more attractive molecular state. $\overline{Z}_{tip}$ denotes the tip equilibrium position at the point of discharging and A_{osc} the amplitude of the tip oscillation. If there was no change in the molecular state,

the tip would move as a function of time along Z between $\overline{Z}_{tip} \pm A_{osc}$ as

$$Z(t) = A_{osc} \cdot sin(2\pi f_0 t) + \overline{Z}_{tip}. \tag{4.2}$$

The force acting on the tip during its motion would follow the blue $F(Z(t))$ curve between F_1 and F_2, and the resulting force gradient (frequency shift), in a linear approximation (valid in the limit of small A_{osc}), is then given by:

$$\Delta f(\overline{Z}_{tip}) \propto -\frac{\Delta F}{\Delta Z} = -\frac{F_1 - F_2}{2 \cdot A_{osc}}. \tag{4.3}$$

The same is valid for the lower $F(Z)$ plot (red in fig. 4.6 b). In this model we illustrate that the force gradient of both plots can be similar.

If the molecular state changes during the motion of the tip at a certain Z position - here at $\overline{Z}_{tip}$ - then also the force acting on the tip will change in a sudden step at $\overline{Z}_{tip}$. This force-Z trace is sketched by a green dashed line in figure 4.6 b). In a linear approximation the effectively measured frequency shift is then:

$$\Delta f(\overline{Z}_{tip}) \propto -\frac{F_1 - F_2'}{2 \cdot A_{osc}}. \tag{4.4}$$

The measured Δf at the point of discharging should be significantly larger than the force gradient values of each individual molecular state. A smaller oscillation amplitude will lead to larger apparent Δf in the plots. Furthermore, the sign of the feature in Δf i.e. whether it is a peak or a dip, is a consequence of the change occurring to higher or lower forces, respectively.

We conclude that the dip in the $\Delta f(V_s)$ plots is due to the tip oscillating between two position with different charge state, and justifies the validity of the fit function in equation 4.1.

With the insight given by this model we can estimate a value for the force difference between the two charge states. The Δf dip depth is $\sim$ 1 Hz which corresponds (see eq. 1.12) to an apparent force gradient decrease of $\Delta F/\Delta Z \sim 13$ pN/Å. By insertion of the oscillation amplitude $\Delta Z = 2A_{osc} = 1$ Å we find a force difference of $\Delta F \sim 13$ pN. This value is based on a linear approximation and, thus, represents an estimation of the magnitude of the force difference between neutral and anionic TCNQ. But these forces can become larger for smaller tip-molecule distances. The distance dependence of the electrostatic potential is $\propto 1/r$, if we assume a molecular point charge. The difference of the $LCPD$ values of neutral and anionic molecule will increase upon closer tip-molecule distances and larger force differences become possible. Even though the obtained force difference is one order of magnitude smaller than the values observed in a hydrogen junction (chapter 3), resonant coupling of the force changes with the tip motion should allow a directed energy transfer between the tuning fork oscillator and the molecule.

In the following we will investigate the effect of the force fluctuations on the energy dissipation of the tuning fork.

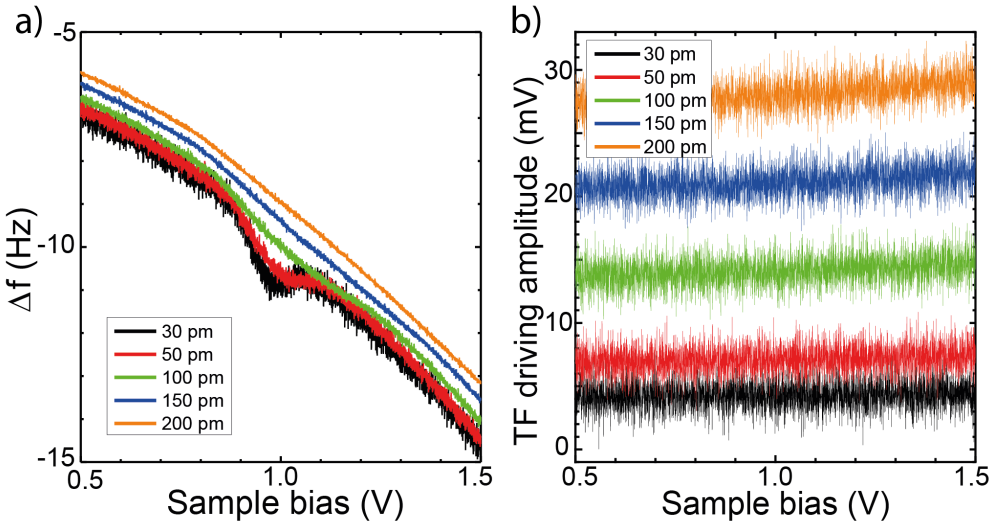

Figure 4.7.: Discharging dissipation measurement **a)** $\Delta f(V_s)$ measured over a type I TCNQ molecule, with different tip oscillation amplitudes. The discharging dip at $V_s = 0.95$ V becomes apparent at oscillation amplitudes $A_{osc} \leq 100$ pm. **b)** Tuning fork driving amplitudes as a function of the bias voltage, simultaneously measured with a). The flatness denotes the absence of dissipation from tip-sample interactions.

4.2.5. Investigation of Dissipation Effects upon Dynamic Discharging of $TCNQ^-$

We have shown before (chapter 3) that the motion of a tuning fork can be driven by fluctuations of the force at the tunneling junction. In the $TCNQ^-$ molecular discharging we investigate a comparable situation: Due to the tip-molecule distance dependence of the charging, the oscillating tip causes fluctuations between the two charge states. As we could see in the previous section 4.2.4, the different molecular charge states are associated with different tip-molecule interaction forces, causing the dip feature in the $\Delta f(V_s)$ and $\Delta f(Z)$ curves. So the periodic motion of the tip is coupled to a periodic fluctuation in the force. We investigate now the effect of the force fluctuations on the tip-molecule energy dissipation.

Figure 4.7 a) compares $\Delta f(V_s)$ curves measured with different oscillation amplitudes over a type I $TCNQ^-$ molecule. A discharging dip in these Δf curve appears at a sample bias voltage of 0.95 V. As expected for a step-like change of the electrostatic force (model fig. 4.6 b), smaller oscillation amplitudes (here: ≤ 100 pm) enhance the effect of the discharging dip in the frequency shift. At larger amplitudes the effect of the step-like force change is averaged out.

Smaller oscillation amplitudes make it also easier to resolve dissipation effects. The energy dissipated due to friction within the tuning fork is in each oscillation cycle $D_0 = \pi k A_{osc}^2/Q$, where k is the tuning fork stiffness, A_{osc} the oscillation amplitude and Q the quality factor of the tuning fork (see also section 1.2.3).

For the tuning fork used in this experiment ($Q = 14000 \pm 500$), this means that the dissipation per oscillation cycle to oscillate the tip with an amplitude of 200 pm is 100 meV. If the oscillation amplitude were only 30 pm the dissipation per oscillation cycle is 2.3 meV what allows us to detect smaller changes of dissipation due to tip-sample interactions.

As mentioned before, the energy dissipated has to be provided externally with a driving signal. Figure 4.7 b) shows the tuning fork driving amplitude as function of the sample bias voltage at different tip oscillation amplitudes, which were recorded simultaneously with the $\Delta f(V_s)$ curves figure 4.7 a). The driving amplitude A'_{drive} is connected to the tip-sample dissipation D_{TS} by the following expression (see sec. 1.2.3) [21]:

$$D_{TS} = D_0 \left(\frac{A'_D}{A_D} - 1 \right) \tag{4.5}$$

where A'_D and A_D are the tuning fork driving amplitudes of the interacting and the free tuning fork, respectively.

The curves are obviously all flat ($D_{TS} = 0$) over the measured bias voltage range. That implies a pure conservative tip-sample interaction and neither damping nor driving of the tuning fork.

Dissipationless Force Fluctuation

In this section we explain the absence of dissipation even in the presence of coupled tip-motion and force fluctuations.

Figure 4.8 a) shows a sketch of the principle of dissipation in atomic force microscopy [137, 138]. The blue and the red curve represent two molecular states with different force-distance dependence. A continuous oscillatory motion of the tip is indicated by the green arrows, forming a closed hysteresis loop. The change from one force-distance curve onto the other happens at different tip-sample distances, depending on the direction of the motion. The gray area between the two force curves and the vertical green arrows corresponds to the amount of energy dissipated in each oscillation cycle:

$$D_{TS} = \int_{Z_{down}}^{Z_{up}} F(z')\,\mathrm{d}z' \tag{4.6}$$

If the transition between the two force curves occurs at the same distance Z, then the integral becomes zero and no dissipation occurs.

Figure 4.8 b) shows a sketch of the tip motion (thick green line) as a function of time. The colored areas below the curve correspond to the time and distance, where the tip moves under either the blue or red force curve from figure 4.8 a). The distance ΔZ between the tip equilibrium position $\overline{Z}$ and the switching events is connected to a delay time $\Delta\tau$, (assuming a symmetric switching with respect to the equilibrium tip position $\overline{Z}$) such:

$$\Delta\tau = \sin^{-1}(\Delta Z / A_{osc})/(2\pi f_0) \tag{4.7}$$

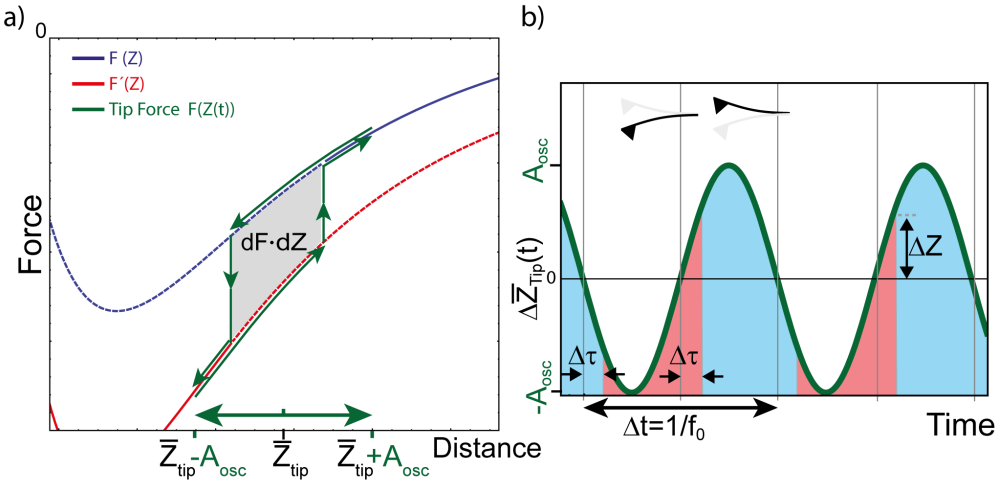

Figure 4.8.: a) Sketch of two simulated Force-distance curves for differently charged samples, the sample is on the left hand side. The overall Force-distance slope is determined mainly by the Lennard-Jones force, the different charge state shifts the force curve of the charged sample to lower Δf values. Hysteresis during the oscillation is necessary for dissipation. **b)** Sketch of the tip motion as a function of time (green line). The motion from $\Delta Z_{tip}(t) = 0$ to $\Delta Z_{tip}(t + \Delta t)$, over one oscillation period, corresponds to one loop along the green arrow path in figure a). For reasons of simplicity a situation, symmetric with respect to $\overline{Z}_{tip}$, is sketched.

where f_0 is the resonance frequency of the tuning fork.

In order to observe a dissipation energy of $D_{TS} = 1$ meV per oscillation cycle with a force difference $\Delta F = 13$ pN (as estimated in section 4.2.4), the ΔZ displacement (between the charge state changes with respect to $\overline{Z}$) needs to be $\Delta Z \sim D_{TS}/(2\Delta F) = 6.7$ pm. Inserting into equation 4.7, with $A_{osc} = 30$ pm and $f_0 = 28.648kHz$, delivers a necessary delay time $\Delta\tau = 1.2 \cdot 10^{-6}$ s.

The fact that we see no dissipation effects in the AFM upon the dynamic discharging of $TCNQ^-$ molecules leaves two conclusions:

I: The discharging is a very fast process, meaning that it occurs immediately (in timescales of the tip motion) as soon as the electric field between tip and molecule is large enough. Thus, there is no hysteresis during an oscillation cycle in the force-distance curve and, hence, also no dissipation. A short estimation of the timescales of the charging makes this plausible: Typical tunneling currents during the discharging process are in the order of 10^{-10} A, so the time between two tunneling events is on the order of $\Delta t = e/I \sim 10^{-9}$ s. The tunneling barrier between substrate and molecule is in this experiment smaller than in other experiments with insulating layer (e.g. NaCL), meaning that the additional electron of the $TCNQ^-$ can tunnel faster from the molecule into the substrate. For a maximum dissipation, the discharging rate should match with the resonance frequency of the AFM lever [129, 139]. The discharging rate is in the experiment too large to observe significant dissipation.

II: The discharging of the molecules could lead to a rearrangement of the molecular

structure. A modified molecular structure could require a different electric field to reverse the charge state and, hence, lead to hysteresis. Obviously this is not the case in the TMTTF-TCNQ charge transfer complex.

The force fluctuations do affect the motion of the tuning fork, observable as a dip in the $\Delta f(V_s)$ and $\Delta f(Z)$ spectra. But because of a too fast charging-discharging process, the interaction with the AFM tip is conservative within the resolution of our experiment.

4.3. Evolution of the Discharging Process upon Discharging of Neighbor-Molecules

In the beginning of this chapter we noted that when the tip is placed above one molecule also the neighbor molecules can become (dis)charged if the bias voltage is large enough. The question we want to ask here is how the discharging of one $TCNQ^-$ molecule affects to its neighbor molecules. Mutual interactions between charged Ag-doping centers in a monolayer of C_{60} molecules have been investigated by Nazin *et al.* [140]. They observed that the Ag-doping center could be charged when its ionization level was shifted up by applying a large enough bias [141]. The charging affected the conduction through C_{60} located around the doping centers. For a pair of doping centers interacting electrostatically, the ionisation of one led to an increase in the ionisation energy of the second, resembling an 'avoided crossing' of the (non-intersecting) charging contours lines.

At certain sample bias voltages (figure 4.3 c), d), g) and h) the contour lines of discharged neighbor $TCNQ^-$ molecules should overlap. In the dI/dV and Δf maps no clear intersecting lines could be observed. Between the TCNQ molecules the dI/dV and Δf patterns become more complex, suggesting a mutual influence of the neighboring molecules charge states [140]. In this section we analyze this effect.

Discharging $dI/dV(V_s)$ Spectral Map of Neighboring $TCNQ^-$ Molecules

In order to characterize the influence of the molecules on each other, we measured simultaneously differential conductance and frequency shift versus bias voltage spectra along a type I $TCNQ^-$ molecular chain.

Figure 4.9 b) shows a $dI/dV(V_s)$ spectral map, measured along the molecular chain indicated in the STM topography inset. A single TCNQ molecule is indicated by a red frame. Brighter colors mean a higher differential conductance, darker corresponds to negative differential conductance. At a sample bias voltage (vertical axis of the map) of 0.25 V we see an increase in the dI/dV due to the molecular interface state, extended over the whole chain. The discharging of the anionic molecules appears as bright spots, centered on top of the molecules at $\sim$ 0.9 V. At higher bias voltages a complex $dI/dV(V_s,X)$ pattern shows up in the spectral map.

Dark spots at bias voltages above show negative differential resistance (NDR) and are due to a decreasing current upon an increasing bias. They are centered in X direction on top of the molecules. These dark spots evolve into dark contour lines and follow a

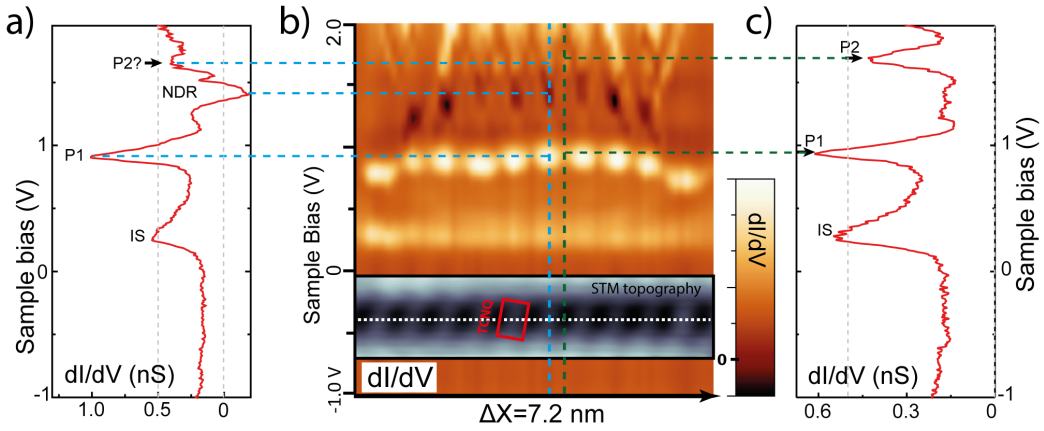

Figure 4.9.: b) $dI/dV(V_s)$ spectral map along a type I $TCNQ^-$ molecular chain. The inset shows an STM image of the $TCNQ^-$ chain, the red frame indicates a single molecule. **a)** and **c)** Single $dI/dV(V_s)$ spectra from the map b) taken as indicated by the vertical dashed lines in b): a) on top of a molecule, c) in between two molecules. The horizontal lines connect features in the spectra with the corresponding feature in the spectral map. ($V_s = 0.75$ V, $I_t = 250$ pA)

linear $V_s(X)$ relation at increasing bias voltage. In between the dark dI/dV contours, some regions show an increased dI/dV.

Figure 4.9 a) and c) show single $dI/dV(V_s)$ spectra from the map b), taken on top of a molecule (a) and in between two molecules (c), respectively. In both spectra the molecular interface state 'IS' is found at the same energy and with the same dI/dV intensity. The discharging peak 'P1', also found in both spectra, has a significantly higher dI/dV value on top of the molecule. At higher bias voltages the two spectra 4.9 a) and c) are significantly different. Negative differential conductance shows up on top of the molecule (a). A second peak 'P2' appears between two molecules. A discussion of these observations is more conclusive in combination withe the $\Delta f(V_s,X)$ map and will be done after the following.

Discharging $\Delta f(V_s)$ Spectral Map of Neighboring $TCNQ^-$ Molecules

Figure 4.10 b) shows a $\Delta f(V_s)$ spectral map, measured simultaneously with the dI/dV map in figure 4.9 b). A single TCNQ molecule is indicated by a red frame. The individual Δf curves were all background corrected by subtraction of a $\Delta f(V_s) \propto (V_s - LCPD)^2$ parabola. Thus, the color code of the map shows Δf values below the background parabola with darker color.

In general, less features appear, compared to the dI/dV spectral map figure 4.9 b). The discharging peak in the dI/dV map appears here as a dip 'P1' in the Δf map. A second dip-feature can be found in the Δf map 4.10 b) at bias voltages 'P2' between the molecules. It appears to be correlated with the peak 'P2' of the dI/dV map fig. 4.9 b). The Δf feature evolves ~linearly along $V_s \propto X$ (for bias voltages ≥'P2'). No further

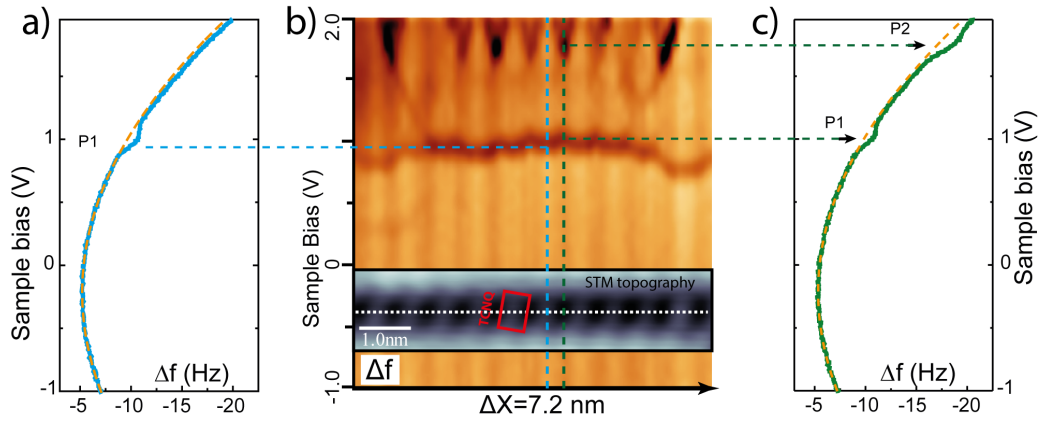

Figure 4.10.: b) $\Delta f(V_s)$ spectral map along a type I $TCNQ^-$ molecular chain. The inset shows an STM image of the $TCNQ^-$ chain, the red frame indicates a single molecule. **a)** and **c)** Single $\Delta f(V_s)$ spectra from the map b) as indicated by the vertical dashed line in b) taken on: a) on top of a molecule, c) in between two molecules. ($V_s = 0.75$ V, $I_t = 250$ pA)

features can be observed on top of the center of the molecules, within the scanned sample bias interval.

In the following we will discuss the observation from the spectral maps, and present an interpretation and model.

4.3.1. Gating the Charge State through Charging of a Neighboring Molecule

We will now discuss the mutual influence of the charge state of $TCNQ^-$ molecules and the charge state of their neighboring molecules, based on the $dI/dV(V_s)$ and $\Delta f(V_s)$ spectral maps figure 4.9 b) and 4.10 b). Figure 4.11 a) and d) show a section from the previous maps. Grey dashed parabola-like lines superimposed to the figures indicate a set of discharging lines, analog to the dI/dV discharging lines in figure 4.1 c). Figure 4.11 b) and c) show a model of the charge state of 3 (and 4, respectively) neighboring $TCNQ^-$ molecules with the tip above one molecule (b) and between two molecules (c), each representing the molecular charge states at the different spectroscopy features ('P1', 'NDR' and 'P2').

At bias voltages below 'P1' the molecule below the tip and its neighbors lay in an anionic charge state. When the sample bias reaches the value 'P1', the $TCNQ^-$ molecule becomes discharged - from anionic to neutral (fig. 4.11 b). The tunneling current increases stepwise what causes the peak 'P1' in the differential conductance and a faint dip in $\Delta f(V_s)$ spectra. Between two molecules 'P1' shifts to larger bias values, due to a larger distance to the molecule. At the position where the discharging lines 'P1' of two direct neighbor molecule cross (above 'P1' at the red vertical lines in fig. 4.11 a) and d) we expect the simultaneous discharging of two neighboring molecules (4.11 c). Within

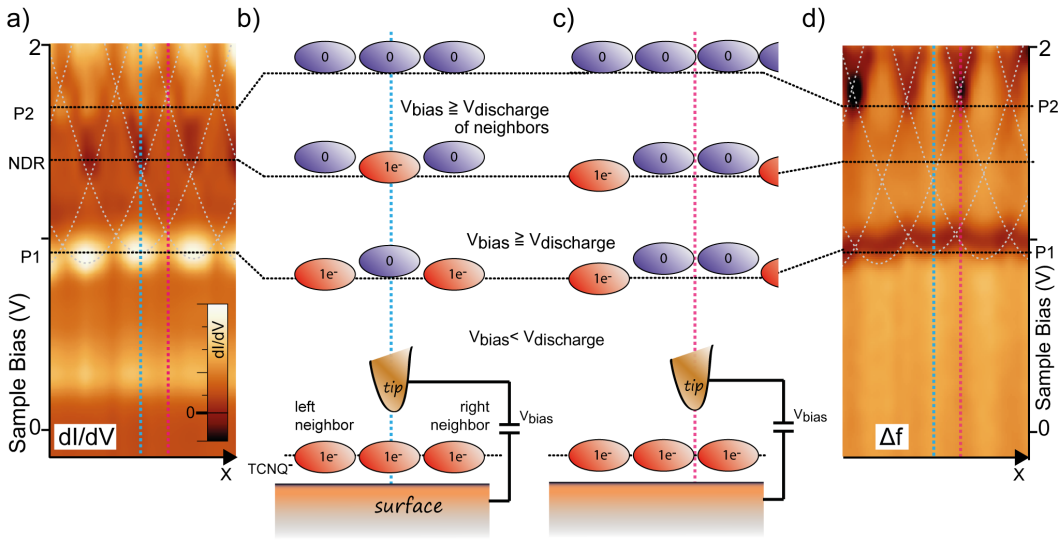

Figure 4.11.: a) dI/dV, $f(V_s)$ spectral map from figure 4.9 b), cut-out on three molecules. The horizontal lines indicate the positions of the features 'P1', NDR and 'P2'. The grey parabola-like curves follow the expected discharging contours of the molecules. **b)** Model of the evolution of type I $TCNQ^-$ molecular charge states with the sample bias voltage, if the tip is placed on top of a molecule. Horizontal dashed lines in the figures a) and d) connect the model to the features observed in the $dI/dV(V_s)$ and $\Delta f(V_s)$ spectra. Red (blue) ovals represent the molecule in an anionic (neutral) charge state. The height relative to the horizontal lines shall visualize the alignment of the involved molecular level (LUMO/SOMO) with respect to the surface fermi level. **c)** Model, similar to b), but the tip is placed in between two molecule (bridge position). The position of 'P1' and 'P2' is indicated by horizontal lines. The grey parabola-like curves follow the expected charging contours of the molecules. **d)** $\Delta f(V_s)$ spectral map from figure 4.10 b), zoom in on 3 molecules. ($V_s = 0.75$ V, $I_t = 250$ pA)

our resolution we observe no significant dI/dV or Δf feature at the crossing point. The constant height Δf maps fig. 4.3 g,h) exhibit faint features along the molecular chain, that could be attributed to the simultaneous discharging. However, for a final conclusion Δf and dI/dV spectral maps with higher resolution in X will be needed.

At larger bias voltages, we observe negative differential conductance labeled 'NDR' in figure 4.11 a) and d) above $TCNQ^-$ molecules. It is caused by a current decrease at V_s ='NDR' (not shown here). The 'NDR' feature occurs where the discharging lines of the neighbor molecules are crossing (at the intersection of horizontal 'NDR' line and vertical blue line in fig. 4.11 a). In the Δf in fig. 4.11 d) we observe no feature dedicated to 'NDR'. We interpret this as a charge inversion on the $TCNQ^-$ below the tip and its neighbor molecules (sketched in fig. 4.11 b) at the 'NDR' line). The crossing of the neighbor $TCNQ^-$ charging lines allows for discharging of the neighbor molecules. The discharged neighbor $TCNQ^-$ modifies the electric field at the central molecule such, that it becomes re-charged. This finding is supported by the absence of Δf features. The net change in the force is too small because the electrostatic force of the two neighbor

molecules cancels with the effect of the re-charging of the closer central $TCNQ^-$.

The feature 'P2' appears as a peak in dI/dV (fig. 4.9 a)-c). It emerges at positions, centered above a $TCNQ^-$ molecule and between two molecules. In fig. 4.11 a) this corresponds to the intersections of the horizontal line 'P2' with the vertical green line and the vertical red line, respectively. In the corresponding Δf map we only observe at this energy a dip located between two molecules. As one can see there, these sites correspond to the crossing of the discharging lines of the two next-neighbors (and crossing the vertical red line, in fig. 4.11 d). This feature evolves into a half-diamond shape at larger bias, defined by the discharging lines, suggesting an electric field induced effect. Our interpretation is the following: when the tip is between two molecules, the next-neighbor $TCNQ^-$ become discharged simultaneously at this bias (see model at 'P2' line in fig. 4.11 c). The effect on the Δf (a dip, see also fig. 4.10 c) and the dI/dV (a sharp peak, see fig. 4.9 c) is comparable to the first discharging of one molecule at 'P1'.

The origin of the peak in dI/dV at 'P2' (fig. 4.11 a) above the center of the $TCNQ^-$ molecules is related to simultaneously discharging this molecule and its direct neighbors into a neutral state. No features appear in the Δf above the molecule center (fig. 4.11 d) which weakens our interpretation. However, this is the simplest of all models which relates the effects to the evolution of the electric field. More complicated models may also be considered but remain speculative at this point.

To summarize the model, we observe indications for a controllable manipulation of the charge state of up to 4 type I $TCNQ^-$ molecules near the tip by choice of the parameters $lateral\ tip\ position$ and applied $bias\ voltage$. The 'NDR' feature is indicative for a mutual influence of neighboring molecules on their charge state. It is comparable to a three-terminal quantum dot device: With the tip as the source, the surface as drain and the molecule as a quantum dot, the neighbor molecule acts as a third, quantized gate. However, further investigations are needed to confirm or improve the presented model. Two ways towards this goal are $dI/dV(V_s)$ and $\Delta f(V_s)$ spectral maps with higher lateral resolution and DFT simulations of the system.

4.4. Conclusion and Outlook

We have investigated the charge transfer complex TMTTF-TCNQ, adsorbed on Au(111), in stoichiometrically mixed islands by means of STM and dynamic AFM. We could observe the (dis)charging of the (anionic) neutral molecules by AFM as a dip in the $\Delta f(Z)$ and $\Delta f(V_s)$ spectra. By fitting of Δf vs. bias voltage parabolas, we could reveal a difference in the molecular electrostatic potential between the two charge states of a type I $TCNQ^-$ molecule and, thus, identify the molecular charge states.

Frequency shift versus Z-distance curves helped to reveal the physical origin of the observed dip in the Δf spectra as a sudden change of the electrostatic force (due to discharging) in concert with the periodic motion of the AFM tip. With this model, a force difference between the two charge states in the order of 10 pN could be obtained.

An initial aim of the project was to find a system, that, by resonant coupling to the tuning fork-tip oscillation, shows energy dissipation. We found no resonant back-acting of

the tip-induced force fluctuations on the tip, thus the (dis)charging process is, within our energy resolution, purely conservative. This can be explained by the small tunneling barrier between molecule and substrate, allowing the molecular (dis)charging at timescales much faster than a tuning fork oscillation period. The proper tuning of the (dis)charging rate - close to the tuning fork resonance frequency - is crucial. A way into that direction would be further decoupling of the charge-transfer complex, e.g. by oxide or NaCl films grown on noble metal surfaces.

In $dI/dV(V_s,X)$ and $\Delta f(V_s,X)$ spectral maps we found complex feature patterns, originating from (dis)charging and interacting charge states of the molecules. So a molecule, discharged upon exposure to a certain electric field, can be recharged at even bigger electric fields due to a gating by the charging of neighbor molecules. Since the last part is still in progress we consider further measurements of dI/dV and $\Delta f(V_s)$ maps with higher lateral resolution and DFT simulations of the system.

Chapter 5.

Charge Localization in a Zwitterionic Molecule by NC-AFM

While the stochastic switching dynamics of hydrogen molecules can be used to couple to and drive a macroscopic oscillator (chapter 3), reversibly controllable bi-stability is desired in molecular switches. A large variety of molecular switches is known to date. Many of them belong to the class of photo switches like azobenzene, diarylethene and their derivatives [142–144]. These can be switched in solution between different conformational states when they are exposed to light of the proper wavelength. Due to modifications in the electronic structure, along with the conformational change the light absorption properties may also alter. This makes it possible to switch into a desired state by choosing the proper light color.

However, when a (conformational) molecular switch is brought onto a surface, there is a high chance that the switch is not able to change between its conformational states [25, 81]. Upon adsorption the molecule may be bound too strong to the surface, steric hinderance may occur and/or the electronic structure can become modified, so that switching often is a one way process or even completely blocked. In order to get functional switches on the surface, one must understand the mechanisms blocking the switching process.

Low temperature scanning tunneling microscopy has become close to a routine tool to characterize molecular switches on surfaces. Its high spatial resolution allows to get not only understanding of the adsorption structure, but also on the electronic structure at the single molecule scale [145, 146]. Additional information can be gained by using tuning fork based dynamic force microscopy. First, it allows to get a more complete picture of the molecular structure and arrangement, since it is not limited to imaging of electron densities but has shown to deliver intramolecular resolution on molecules [22, 147–149]. Second, with $\Delta f(V_s)$ spectroscopy one can determine variations in the electrostatic potential with submolecular resolution and construct a 3-dimensional picture of the electrostatic potential, which allows us to identify intramolecular charge redistribution [23, 50].

In this chapter we extend our understanding and get a deeper insight on the open merocyanine (MC) form of the ring opening-closing switch 1,3,3-Trimethylindolino-6'nitrobenzopyrylospiran. We would like to know, if the molecular dipole remains when the molecule is adsorbed on a Au(111) surface. Here, we use tuning fork based atomic force microscopy to map the charge distribution within the molecules [50] and confirm

the existence of an intramolecular dipole-like charge distribution. But we find also an effective screening of the intramolecular charges by the metal surface and a mutual charge cancellation between neighboring molecules. Correlating the topographic STM with Δf features as well as a comparison between the AFM charge mapping and the charge distribution obtained from DFT will help us to improve the MC dimer chain structural model. We investigate an unexpected inversion of the molecular electrostatic potential when the tip is approached into contact with the molecule. From $LCPD(Z)$ spectroscopy we resolve the evolution of the electrostatic potential also in the 3rd dimension (Z) and $\Delta f(Z)$ spectroscopy is used to identify the interaction regimes between tip and MC molecules. Correlations in the spectroscopy maps allow us to develop a model that explains the inversion of the electrostatic potential.

Spiropyran Revisited

The ring opening-closing switch 1,3,3-Trimethylindolino-6'nitrobenzopyrylospiran (in the following called spiropyran, SP) on Au(111) was investigated within the framework of the Sfb 658 'Molecular Switches on Surfaces' with different techniques, e.g. LT-STM, X-ray photoelectron spectroscopy (XPS), near-edge X-ray absorption fine structure spectroscopy (NEXAFS) and high-resolution electron energy loss spectroscopy (HREELS) [15, 82, 151].

Spiropyran can be converted by thermal and optical excitation reversibly into another isomeric configuration, the merocyanine (MC) form. The skeletal formulas of both isomers are shown in figure 5.1 c) and d), respectively. In gas phase and solution the three dimensional spiropyran can be isomerized into the planar merocyanine form by irradiation with UV light [152]. The back-reaction to the more stable spiropyran form can be induced by illumination with visible light [153]. Thermal isomerisation is also possible; in solution and solvents at room temperature an SP $\rightleftarrows$ MC photostationary state is achieved. Due to the zwitterionic character of the MC form, the ratio MC/SP increases with the solvents polarity.

However, upon adsorption on a surface the gas phase stability of SP over the MC isomer is reversed [82]. Schulze *et al.* found that molecules evaporated onto a cold Au(111) (or Bi(111)) surface do adsorb in the SP form, but when the sample is annealed to room temperature, or above, the molecules are converted irreversibly to the MC form.

Merocyanine Structure

Merocyanine is a rather planar and prochiral molecule: The molecule consists of two main parts, an indoline side (figure 5.1 a) and a nitrobenzopyran group (figure 5.1 b). They share the same carbon atom, indicated by the red circle in figure 5.1 a) to d), to form the SP/MC molecule. For the conversion from the spiropyran into the merocyanine isomer, the nitrobenzopyran group is opened by breaking a bond in the pyran ring, indicated by the red arrow in figure 5.1 d). The pyran oxygen stays attached to the nitrobenzene group and becomes a carbonyl, thus the former nitrobenzopyran group becomes a *nitrophenolate* as we will refer to it in the following. The indoline and the ni-

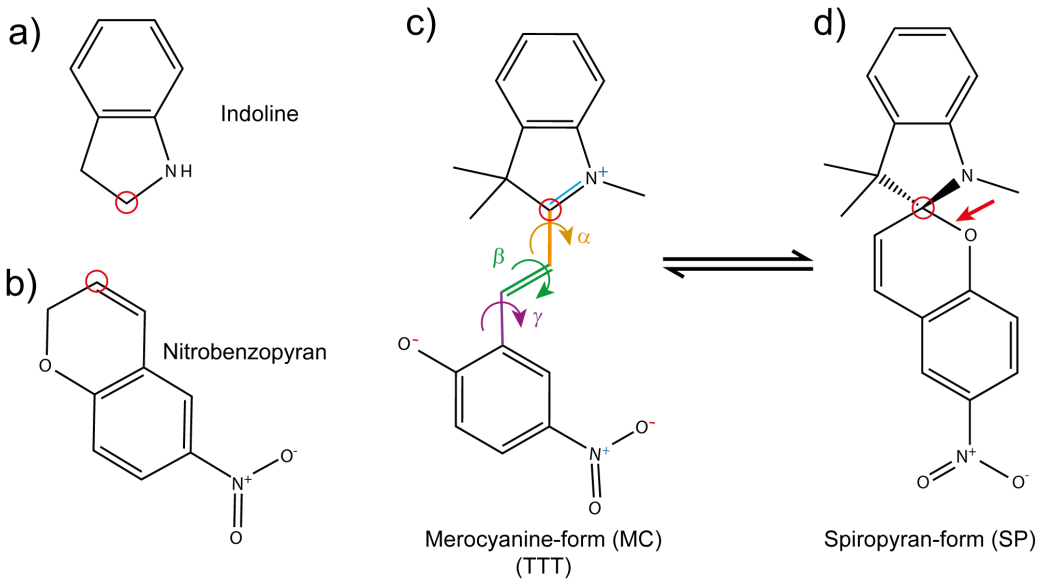

e)

System	E (eV)	α	β	γ
SP	−0.9651	120.3	0.7	0
MC rotamers:				
TTC	−0.9560	180	180	0
TTT	−0.9533	180	180	180
CTC	−0.9525	11.9	179.2	1.8
CTT	−0.9513	9.1	179.9	178.5

Figure 5.1.: Merocyanine and Spiropyran structure. The two building blocks for spiropyran are **a)** indoline and **b)** nitrobenzopyran. The planar merocyanine form **c)** can be converted to the three dimensional spiropyran form **d)** by a bond formation from the carbonyl (left in c) with the indoline, the bond is indicated in d) by the red arrow. The red circles in a), b) c) and d) show the shared carbon atom of the indoline and the nitrobenzopyran group. By rotation around the bond angles α, β and γ, indicated in c), also different merocyanine isomers exist. Table **e)** lists the minimum energies of the spiropyran (SP) form and different planar merocyanine isomers and the corresponding angles, from [150], gas phase DFT.

trophenolate group stay connected via an ethylene -C=C- bridge. At a fixed orientation of the indoline group one has two possibilities to arrange the S-shaped ethylene bridge and two possibilities how the nitrophenolate group is attached, by rotation around the angles α and γ as shown in figure 5.1 c). This gives a total of 4 chiral rotamers in gas phase which are shown in figure 5.2 and labelled *TTC, TTT, CTC* and *CTT* - upon adsorption on a surface there add up the 4 mirror forms due to the molecules prochirality. DFT calculations (see fig. 5.1 e), from [150]) show that the 4 structures are relative close in energy with the TTC being slightly more favorable. However, this situation could change

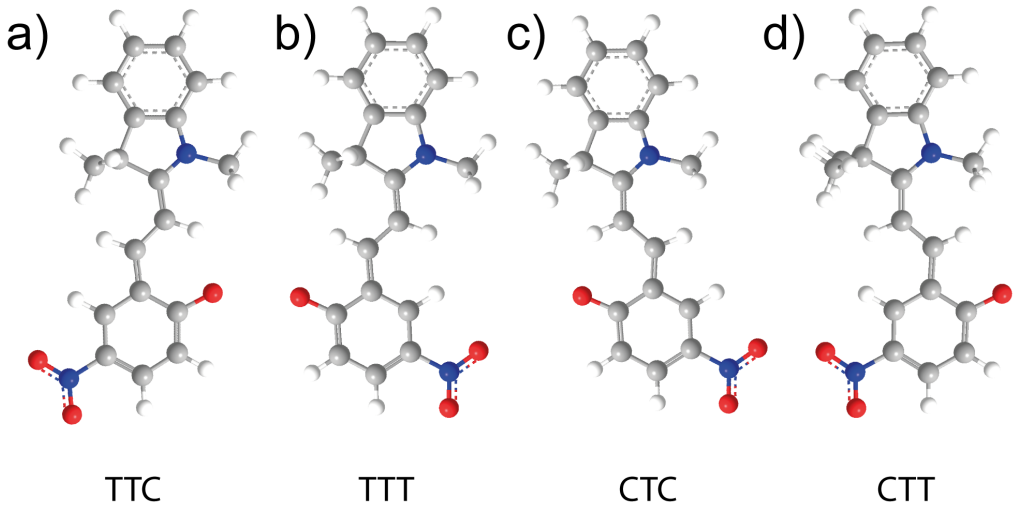

Figure 5.2.: Merocyanine planar isomers. The structures a) to d) correspond to the minimum energy structures listed in 5.1 e).

upon adsorption on the surface, as the stability inversion of MC over SP shows.

5.1. Localizing Charges in a Zwitterionic MC Molecule

In our experiment, we followed the preparation steps from Schulze [82]: The molecules were evaporated from a Knudsen cell, held at ∼348 K, onto the atomically clean Au(111) sample and then annealed to room temperature. After molecular deposition, the sample was transferred into the cold STM for inspection. Figure 5.3 shows an STM overview image (a) and detailed images (b), (c) depicting the typical merocyanine dimer chains.

In c) a molecular model of the structure proposed by Schulze *et al.* [15, 82] is overlaid to the constant current STM topography image. By a combination of different techniques - LT-STM, XPS, NEXAFS and HREELS - it had been confirmed that the molecules adsorb with both benzene rings planar on the surface. Other findings also supported that the observed chain structure could be finally assigned to the planar MC form, arranging in molecular dimers.

However, the bonding structure of the MC planar isomers within the dimer chains could not be resolved definitely. MM2 force field [154] molecular mechanics simulations performed by Schulze supported the structure shown in figure 5.3. The high protrusion in the STM images was assigned to the localization of the indoline nitrogen. In the MC form this nitrogen donates charge to the conjugated π-system of the molecule. The positive localized charge could then lead to an effective reduction of the tunneling barrier, which might let the molecule appear locally higher at this point. While a positive charge would be located around the indoline nitrogen, the oxygens at the nitrobenzene side of the molecule tend to accumulate electrons. This charge distribution results in a zwitterionic

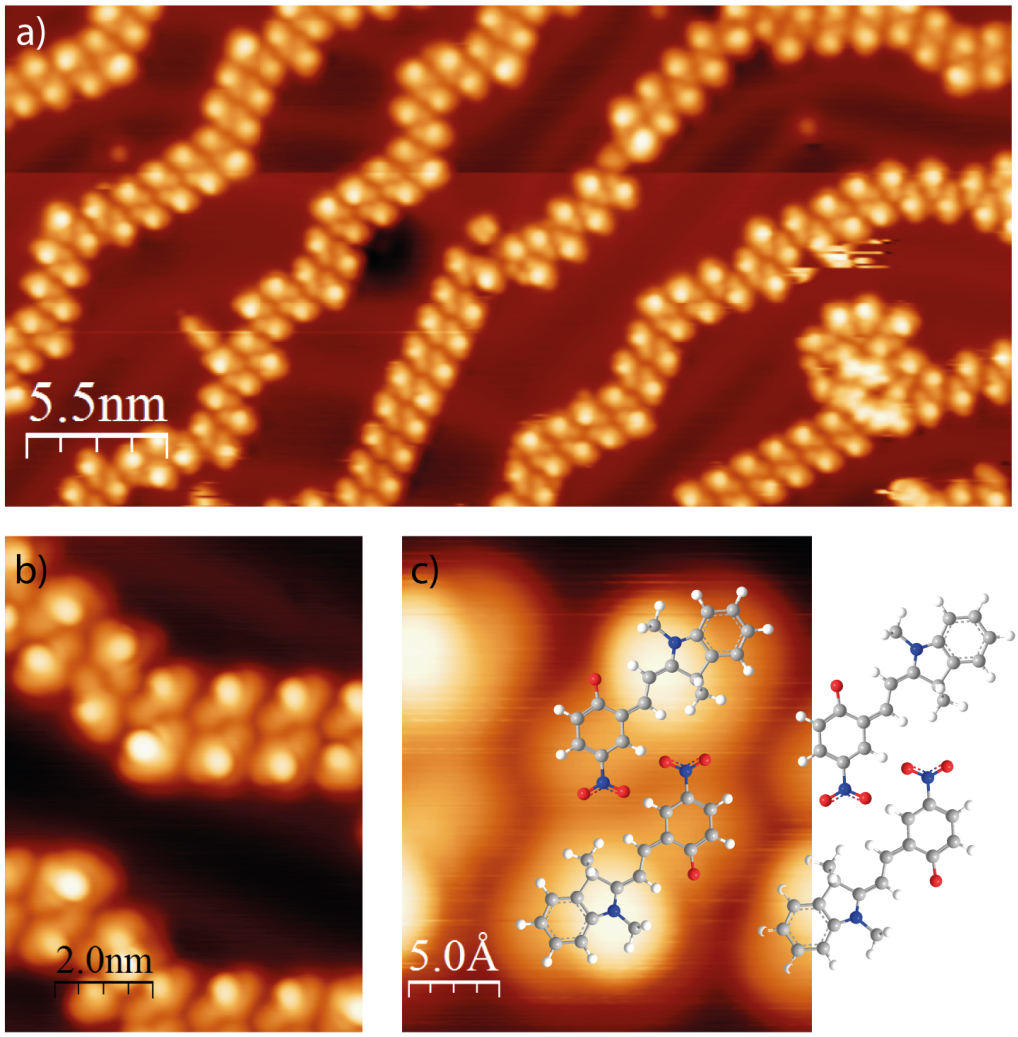

Figure 5.3.: Merocyanine STM topography images. STM overview image **a)** ($V_s = 1.025$ V, $I_t = 185$ pA) and detailed images **b)** ($V_s = 1.07$ V, $I_t = 391$ pA) and **c)** ($V_s = 1.025$ V, $I_t = 116$ pA) show the dimer chain structure of MC on Au(111). A model of the structure proposed by Schulze *et al.* [15, 82] is superimposed to (c).

form with an electrical dipole moment of 12 Debye [155, 156]. On the surface, the survival of such dipole remains to be probed. The formation of dimer chains separated from each other was interpreted as a sign speaking for its survival. In the proposed structure (figure 5.3 c) positive charges would be localized at the outer rim of the dimer chains and repel each other.

The aim of the following experiment is to localize the charge within the merocyanine molecules using $\Delta f(V_s)$ spectroscopy. As it has been shown in recent publications, dynamic AFM is capable of measuring differences in the local electrostatic potential (also: local contact potential difference, LCPD) with submolecular and even atomic resolu-

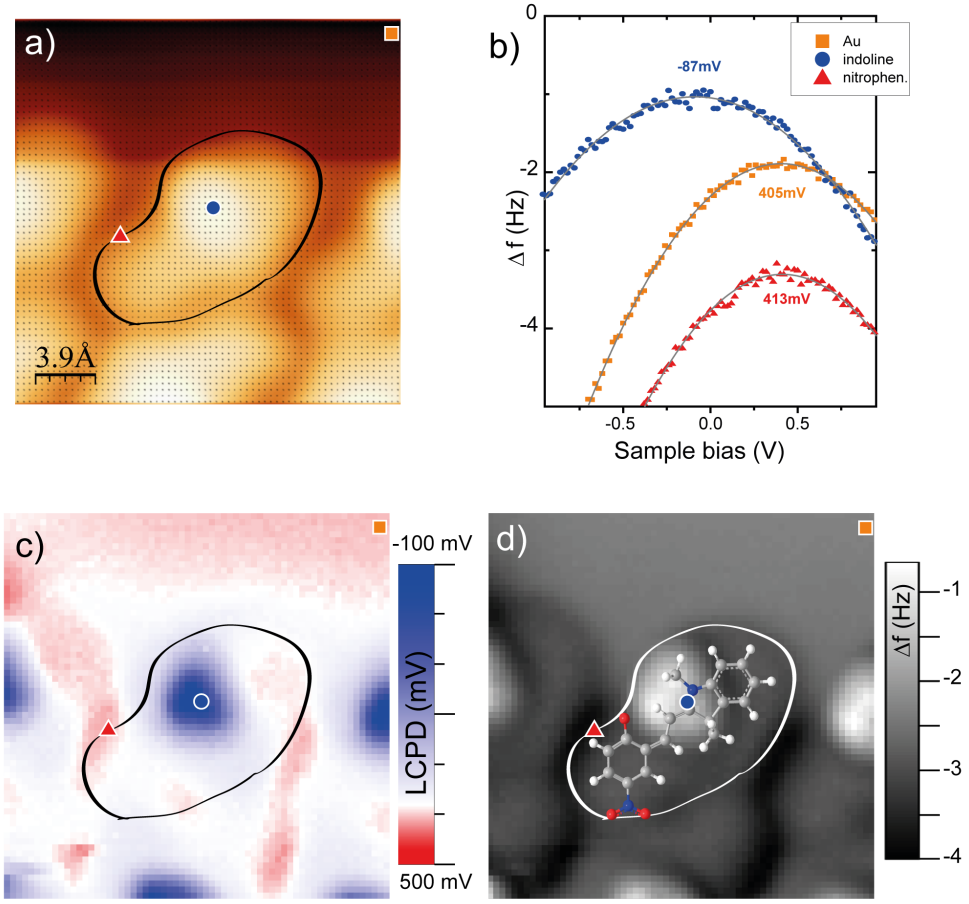

Figure 5.4.: Merocyanine constant current $LCPD$ map **a)** STM image of the 64×64 grid area (25 Å^2). In each dot one $\Delta f(V_s)$ spectrum was taken. The line around the topography iso-contour is also overlaid to the other figures c) and d) for better comparison. **b)** 3 $LCPD$ spectra from the spectra grid. The icons plotted on the figures a), c) and d) indicate the positions where the spectra were taken. **c)** $LCPD(X,Y)$ map. Red: electron accumulation. Blue: electron depletion. **d)** $\Delta f(LCPD,X,Y)$ map. Setpoint: $I_t = 110$ pA, $V_s = 0.74$ V

tion [23, 50, 157] on insulating NaCl films. The procedure is comparable to the spectroscopy we performed on the TMTTF-TCNQ molecules (chapter 4).

At a fixed tip-sample distance the sample bias is varied while the frequency shift is recorded. The frequency shift depends quadratically on the voltage:
$\Delta f(V_s) \propto -(V_s - LCPD)^2$. Due to the attractive character of the electrostatic forces in a capacitor like junction, the frequency shift becomes more negative for stronger electrostatic forces. At the voltage $V_s = LCPD$ the external applied electrical field minimizes the electrostatic forces between tip and sample. From a simple quadratic fit one gets directly the local contact potential difference between tip and sample (for details see also sec. 1.2.6). A more positive $LCPD$ means in our setup, that either a more

negative charge distribution, or a dipole pointing towards the sample, is present at the sample. These measurements were performed on a grid over a sample area. Of course the tip must not change during such a measurement, since all potential differences have to be related to the tip to make them comparable. In this way we could get maps of the electrostatic potential and localize intramolecular charges on MC dimer chains.

5.1.1. $LCPD$ Maps of MC on Au(111)

A map of the local contact potential difference $LCPD(X,Y)$ is shown in figure 5.4 c). It consists of 64×64 $LCPD$ values obtained on a 25×25 Å^2 large grid. The grid points are superimposed to the simultaneously recorded topography image 5.4 a). At each grid point, the tip position was stabilized with a setpoint current of 0.11 nA and a sample bias of 0.74 V. In each of the grid points one $\Delta f(V_s)$ spectrum was recorded. Each spectrum consists of 100 $\Delta f(V_s)$ data points and the bias was swept from $+1$ V to -1 V in 5 seconds.

Single $\Delta f(V_s)$ spectra taken on the different spots, where indicated by the symbols in figure 5.4 a), c) and d), are plotted in figure 5.4 b). Each of the curves can be fitted with a parabola of the form $\Delta f(V) = A + B(V_s - C)^2$, where the fitting parameter C is the actual local contact potential difference ($LCPD$) (plotted in 5.4 c), A corresponds to the frequency shift at $V_s = LCPD$ (plotted in 5.4 d) and B is a prefactor containing the tip-sample capacitance (see also section 1.2.5).

The $\Delta f(V)$ curves in figure 5.4 b) are obviously very different. First, the frequency shift at the maximum of the curves $\Delta f(LCPD)$ is more negative on the nitrophenolate side than on the Au(111). This is typical on molecules [22]: Due to the lower conductance of the molecule compared to Au, the distance tip-molecule is closer than the distance tip-Au at the tunneling setpoint. The higher attractive short range forces lead to a more negative frequency shift. Unexpected was the relative higher $\Delta f(LCPD)$ at the indoline side of the molecule: Significant contributions from short range repulsive forces lead here to a change towards positive frequency shifts, as we will also see later (see figure 5.10).

The Δf parabola measured on the indoline side of the molecule is centered at a more negative sample bias, thus represents a more negative $LCPD$, than the one on the Au surface. This shift in the electrostatic potential can be attributed to an electron depletion. In the nitrophenolate side we find the parabola shifted to more positive $LCPD$, thus electron accumulation in comparison to the Au substrate. Such strong contrast in the $LCPD$ of up to 500 mV has, to our knowledge, not yet been reported within one single molecule [23, 50]. Moreover, the shifts follow different sign with respect to the Au(111) background on the two parts of the molecule.

Partially, the large $LCPD$ contrast can be explained by the choice of the substrate. If we assume that inside the molecule localized charges can be treated as point charges, then the electrostatic potential decays with $1/z^n$, where $n = 1$ describes the potential decay of a single point charge. On a metal surface a point charge induces an image charge which

causes the potential to decay faster, with $n \sim 2$. This means that, the closer one gets with the tip to probe a charge, the higher the observed $LCPD$ will be (see sec. 1.2.7). Since the experiments by Gross *et al.* were performed on molecules adsorbed on a NaCl double layer [23], they could not approach the tip as close as we could do it for the MC dimer chains adsorbed on the more reactive Au(111) surface, thus explaining our larger $LCPD$ contrast.

The $LCPD$ values are plotted color coded in figure 5.4 c), where we interpret red areas corresponding to more electron accumulation and blue to electron depletion. For easier comparison of the MC molecule position, the molecular contour in the topography image 5.4 a) is superimposed also to the $LCPD$ (c) and $\Delta f(LCPD)$ image (d). The resulting $LCPD$ map fits the expected behavior from the gas-phase molecule, thus the zwitterionic character of the molecules can be confirmed also upon adsorption on a surface. A more negative charge (reddish) is located at the nitrophenolate side while a more positive charge is located around the indoline part of the molecule, where we had expected the nitrogen from the previous experiments. But in previous works a protrusion in the topography image at this site was assumed to be an electronic effect rather than a topographic effect: due to the positive charge accumulation at this site an effective local reduction of the tunneling barrier might lead to higher conductance, and therefore apparently higher topography. This is in contradiction with the following observations.

MC Structure: New Findings for a New Model

A closer look to the $\Delta f(LCPD)$ map figure 5.4 d) shows that at this site the frequency shift has the highest values - even higher than on bare gold. This tells us that we are already in a regime of significant repulsive interaction [22, 158]. The findings are also supported by later experiments, where $\Delta f(Z)$ was measured as a function of the tip-sample distance (sec. 5.2.2). This site is the highest part of the molecule and therefore the constant current topography image does indeed reflect the molecular topography.

Therefore we must assume that the indoline side of the molecule is mirrored through the molecular axis; the protrusion then comes from the two methyl groups which lie on top of each other upon planar adsorption of the MC molecule. The orientation of the upper methyl group seems to be even nearly perpendicular to the surface as suggests the triangular shape of both, the $\Delta f(LCPD)$ protrusion and the positive charge localization in the $LCPD$ map.

A closer look to the charge distribution on the nitrophenolate site, e.g. close to the spot marked with the red triangle in figure 5.4 c), shows confined regions of electron accumulation. These can not be matched with the oxygen positions of the structural model figure 5.3 c), where one would assume electron accumulation. On the other hand a rotation of the nitrophenolate around γ (see figure 5.1) fits better with the observed $LCPD$ variations. Since this is still speculative at this point, we performed DFT calculations to find out which of the dimer structure models would fit better with the experimental observations.

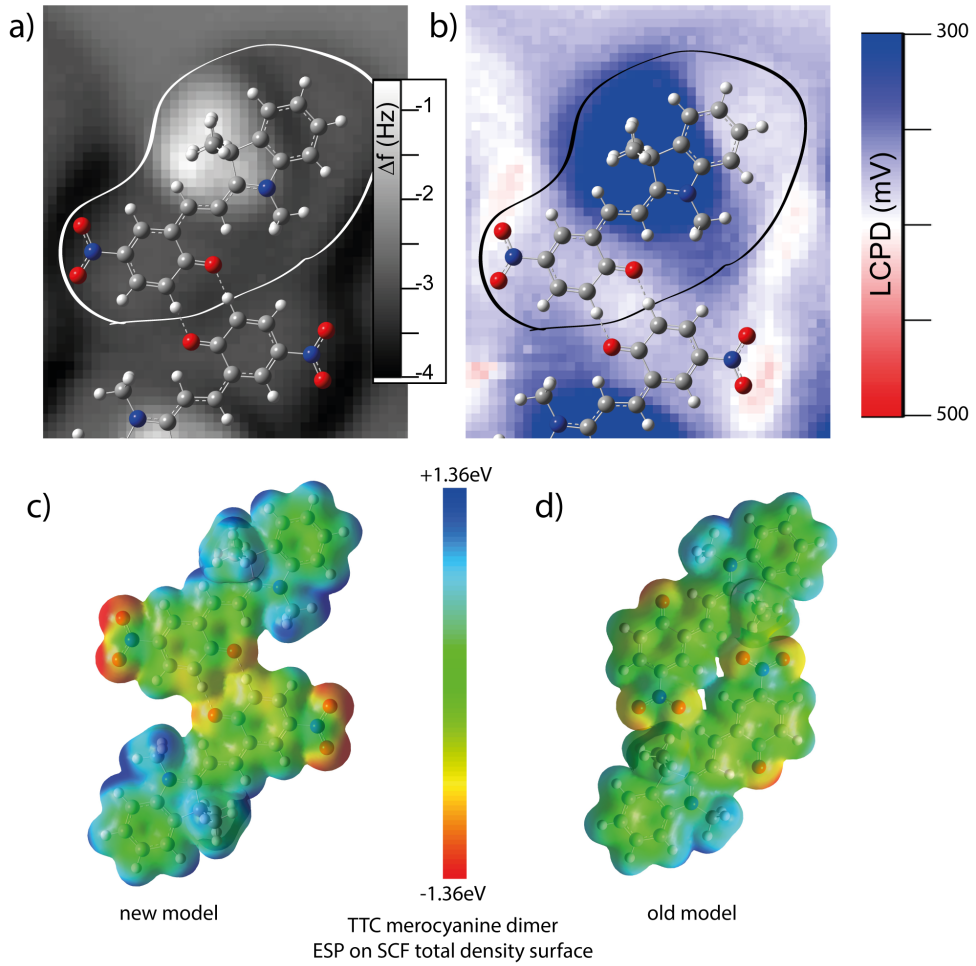

Figure 5.5.: a) Constant current $\Delta f(LCPD,X,Y)$ map (same as fig. 5.4 d). **b)** $LCPD(X,Y)$ map (same as fig. 5.4 c), but with different color scale range). Red: electron accumulation. Blue: electron depletion. The new dimer structure model c) is superimposed to figures a) and b). (Setpoint: $I_t = 110$ pA, $V_s = 0.74$ V) **c)**, **d)** DFT obtained gas phase minimum energy dimer structures. An iso surface of a total electron density of 4 $me^-/\text{Å}^3$ is plotted onto the structures, the density surface was mapped with the electrostatic potential energy felt by an electron moved over this surface. The ESP energy color code corresponds to red (blue) for electron accumulation (depletion).

5.1.2. Density Functional Theory Calculations of Free MC Dimer Structures

Density functional theory (DFT) calculations were performed with the commercial software package Gaussian 09 [159] on the high performance computing cluster of the FU Berlin [160]. The initial setup was a dimer of two molecules, arranged in a way close to the expected structures. A structure optimization was performed using the hybrid

functional B3LYP with the STO-3G basis set. A surface was not included.

Figure 5.5 c) and d) show the minimum energy structures of two dimer arrangements obtained from DFT calculation. In approach to correlate these structures with the charge distribution, we generate electrostatic potential energy maps from the DFT results as following. From the self consistent field (SCF) density matrix an iso surface of a total electron density of 4 $me^{-}/\,\mathring{A}^{3}$ was generated and plotted onto the molecular structures. This is a simplified approach to simulate a topography surface comparable to an STM topography image, which is an image of a surface of constant density of states. This SCF iso surface was then mapped with the electrostatic potential (ESP) energy (also obtained from the SCF density matrix) felt by an electron being moved over this surface. The color code of the mapping uses blue to visualize electron depletion, red for electron accumulation and green in between.

Figure 5.5 d) corresponds to the structure model from figure 5.4 d) while figure 5.5 c) is an alternative structure model approach. The difference between figure 5.5 c) and d) is that they use either of the two prochiral forms. A rotation of the MC molecules by 180 ° each around an axis in the surface plane changes between the old and the new model. For the old model there is no agreement between the $LCPD$ map and the calculated ESP energy surface. We find a very good agreement between calculated charge distribution with the measured $LCPD$ map for the new model figure 5.5 c). The oxygen sites carrying the electron accumulation fit well with the reddish regions within the molecular chain of the $LCPD$ map b). There is also a significant accumulation of positive charge on all three methyl groups of the indoline side, in agreement with the blue regions of the $LCPD$ maps.

Figures 5.5 a) and b) show the new structural model superimposed to the maps of $\Delta f(LCPD)$ and $LCPD$, respectively, and are in very good agreement with the maps. With the orientation of the indoline side determined by the methyl groups height and the orientation of the nitrophenolate side determined by comparison between $LCPD$ map and DFT calculation, we still cannot conclude if the observed structures are formed by TTC or CTT isomers (fig. 5.2). Since the TTC isomer is about 47 meV more stable in gas phase [150] we propose this structure as the most favorable one. However, from our data we cannot exclude also the CTT isomer.

In conclusion, we can confirm the zwitterionic character of the MC molecules with intramolecular resolved charge distribution. Moreover, the new techniques, AFM and $\Delta f(V_s)$ spectroscopy by AFM in combination with DFT helped us to improve the structural model of the MC chains.

5.2. $LCPD$ Contrast Inversion

In the constant current $\Delta f(LCPD)$ map 5.4 d) we found that the tip is interacting in different force-distance regimes with the molecule, especially on the regions of highest charge accumulation. For example on the indoline side in the region of electron depletion, significant contributions of repulsive force indicate that the tip is very close to the molecule. In order to understand the MC molecules topographic influence on the $LCPD$,

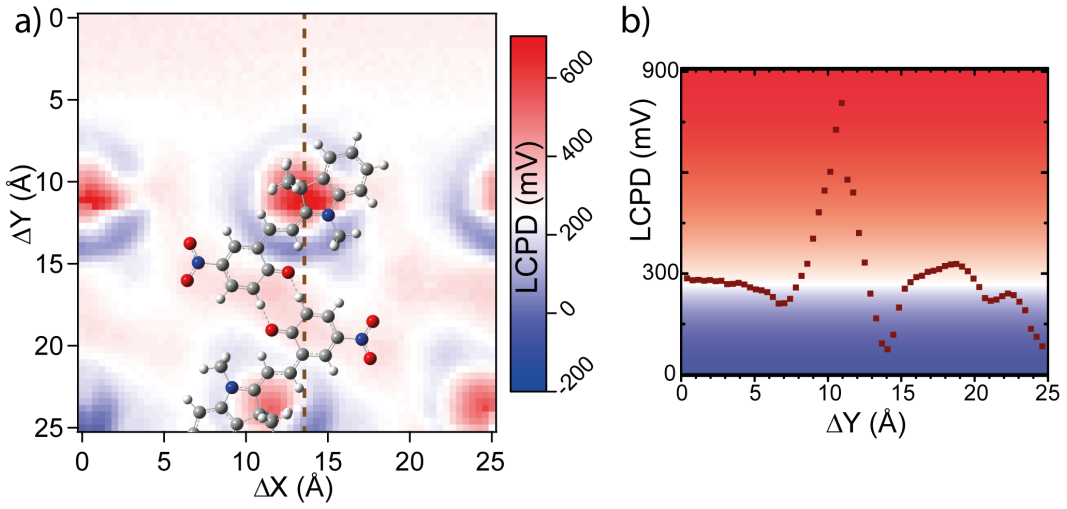

Figure 5.6.: $LCPD$ contrast inversion **a)** constant height $LCPD$ map. Blue (red) color corresponds to electron depletion (accumulation). A dimer structural model (from fig. 5.5 c) is superimposed to the image. Z position of the grid plane determined by tunneling setpoint at the coordinates $\Delta X = 12.5$ Å, $\Delta Y = 25$ Å: $I_t = 517$ pA, $V_s = 1.04$ V. **b)** $LCPD$(Y) profile of the map a) at $\Delta X = 13.5$ Å as indicated by the dashed line. The background is colorized same as in figure a).

we mapped the $LCPD$ as a function of the lateral position on a constant height plane parallel above the Au(111) surface. This is just done in analogy to the constant current $LCPD$ maps (figure 5.4), but the $\Delta f(V)$ spectra on the grid are all taken at the same Z distance with respect to the underlying Au(111).

Previous findings regarding the localized charges of the zwitterionic molecule can in general be confirmed. But we observe an unexpected $LCPD$ contrast inversion on top of the di-methyl sites of the molecules indoline side. Figure 5.6 a) shows a 64×64 constant height grid of the $LCPD$ on a merocyanine dimer chain. We see again the electron accumulation (red) on the oxygen sites of the nitrophenolate group. A circular feature of electron depletion (blue) around the di-methyl and a faint feature on the single methyl of the indoline side of the molecule confirm the previous findings. But at closer lateral distance to the di-methyl site the $LCPD$ contrast is inverted: It changes from negative values to positive values, much larger than on the nitrophenolate group.

Figure 5.6 b) shows a $LCPD(Y)$ profile at $\Delta X = 13.5$ Å as indicated by the dashed line in figure 5.6 a). The inversion occurs smoothly from the $LCPD$ maximum at $\Delta Y = 11$ Å within 3 Å to a $LCPD$ minimum at $\Delta Y = 14$ Å . This $LCPD$ contrast inversion can not simply be explained with the present picture of charge distribution and needs further investigations.

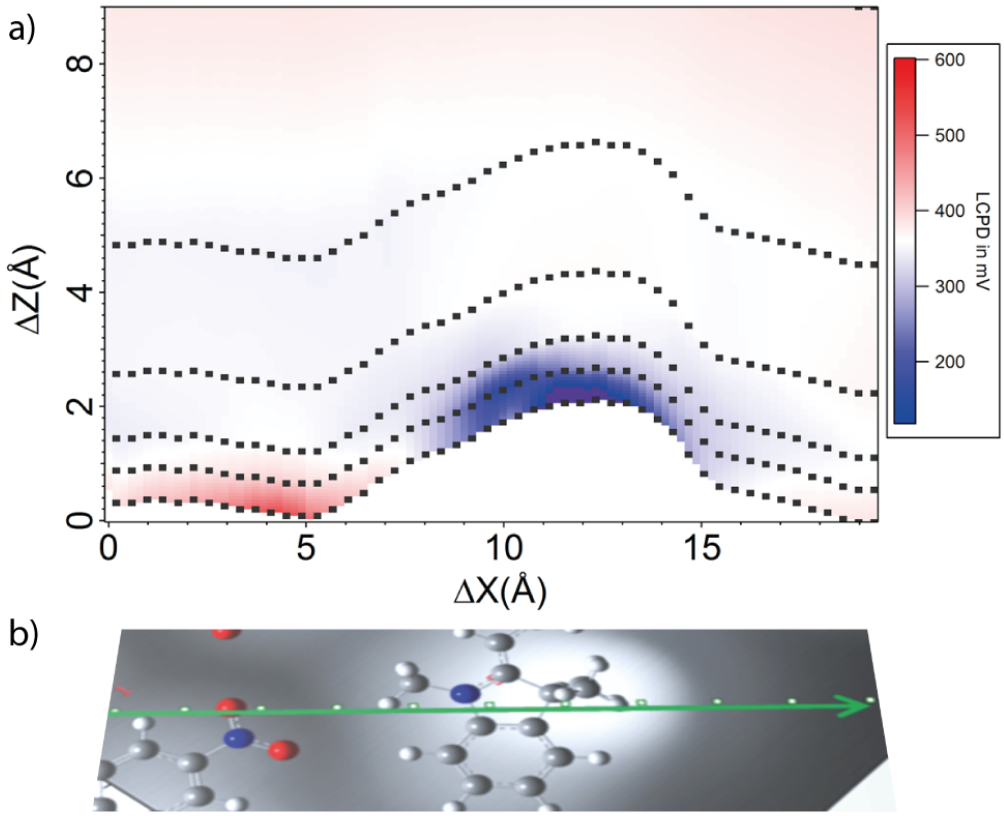

Figure 5.7.: $LCPD(X,Z)$ line profile **a)** Constant current line profiles over a merocyanine dimer. The $LCPD$ was determined in each point along the profile at different Z offsets from the tunneling setpoint, indicated by the dotted lines. For better visualization the $LCPD$ values are interpolated in Z direction. **b)** STM image of the MC dimer with the profile (green line) and the structural model superimposed. ($I_t = 520$ pA, $V_s = 1.02$ V)

5.2.1. $LCPD$ Profiles: Lateral and Vertical Evolution of the Electrostatic Potential along a MC Dimer

In order to understand the influence of the topography on the $LCPD$, we recorded $\Delta f(V_s)$ spectra at different vertical tip-sample distances along a constant current line profile over a molecular dimer. Figure 5.7 b) shows the $LCPD$ measured on a line profile along a merocyanine dimer as a function of the tip-sample distance. An STM image with superimposed molecular structural models visualizes the profile's path. In each of 100 equidistant points $\Delta f(V_s)$ spectra were measured at 7 different tip heights ΔZ (0, 0.5, 1, 2, 4, 8, 16 Å), with respect to the tunneling setpoint. For each $\Delta f(V_s)$ spectrum the $LCPD$ was determined by a fit. The resulting $LCPD(Z,X)$ map is shown in figure 5.7 a). The individual $LCPD$ values are offset vertically to reflect the height of the tip above the Au(111) surface, indicated by the dotted lines.

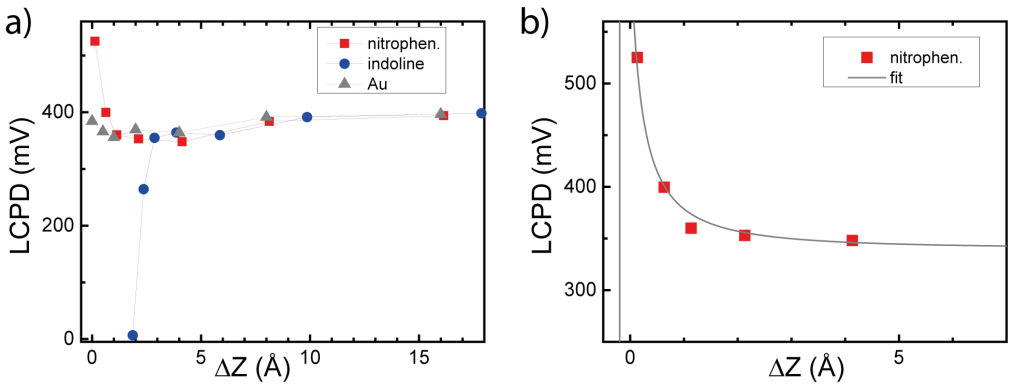

Figure 5.8.: a) $LCPD$ as a function of relative tip-sample distance, measured on Au(111) (triangles), the indoline (circles) and the nitrophenolate group (squares). Data extracted from the profile figure 5.7 a). **b)** magnification of the $LCPD(Z)$ curve on the nitrophenolate (squares) in a). The line was obtained from a 'fit' with an electric dipole point charge model.

Far from the surface at $Z_{offset} = 16$ Å (not shown in the figure) a homogenous background CPD of ~ 400 mV is observed, this is associated with the overall contact potential difference, which is related to the work functions of the molecule covered sample and tip (see sec 1.2.6, 1.2.7). As the tip approaches closer to the molecule to a vertical Z offset of 4 Å, the $LCPD$ decreases to 360 mV, further away from the molecule, on the Au(111), this decrease is lower (see also figure 5.8 a).

While approaching closer on the MC molecule one can see the localization of the negative charge (colored red) at the nitro site of the nitrophenolate group. The $LCPD$ values are significantly higher than the overall CPD background. The positive charge (blue) within the molecule is distributed over a large region around the indoline group. We observed this already in the $LCPD(X,Y)$ maps (figures 5.4 c) and 5.6 a) and find it also in the ESP maps of the calculation results from DFT in figure 5.5 c). Within the indoline group the positive charge appears distributed mainly over the bulky methyl groups. Here we find $LCPD$ values much smaller than the overall CPD background. Because the positive charge is distributed over the bulky indoline groups, which are located on the outer sides of the dimer chains, the negative charge located at the nitrophenolate group is cloaked. This explains the chain's tendency to stay separated from each other, as reported by G. Schulze [82]. The equal positive charge on the outside of the MC chains leads to coulomb repulsion between chains next to each other.

Z-Dependence of the Electrostatic Potential of an Intramolecular Charge Accumulation

Figure 5.8 a) compares $LCPD$ values as a function of the tip-sample distance, obtained on the oxygen site of the nitrophenolate group, and on the di-methyl of the indoline group and on Au(111). The distance dependence on the nitrophenolate site (5.8 b)

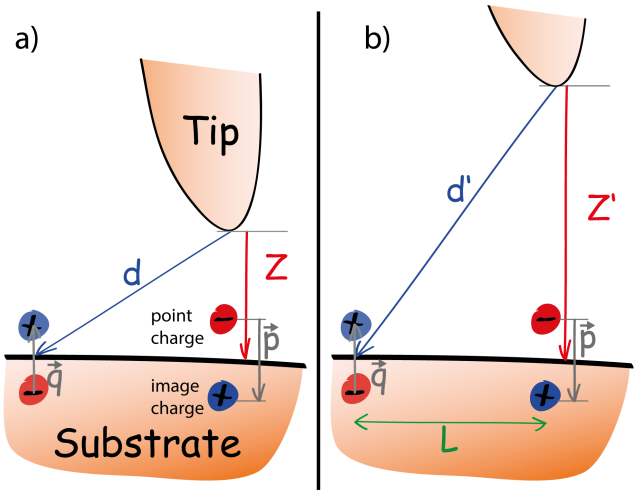

Figure 5.9.: Sketch: Effect of neighbor dipoles on the electrostatic potential at the tip. **a)** at small distances Z is $d \sim const.$ but the potential of the dipole $\vec{\mathbf{p}}$ changes a lot on small changes of Z due to $V_{\vec{\mathbf{p}}}(Z) \propto 1/Z^2$. **b)** at larger Z the dipole $\vec{\mathbf{q}}$ matters also due to $d' \sim Z'$; a multipole approach is needed to describe the potential.

follows a $\propto 1/z^n$-like behavior with an exponent n larger than 1. We interpret this as a strong screening of the charge by induced image charges in the substrate. A dipole model with $n = 2$ can not fit the data with reasonable charge and distance coefficients. The general form of a dipole potential is given by the expression

$$V(Z) = V_0 + \frac{q}{4\pi\epsilon_0}\left[\frac{1}{(Z - Z_0 + d/2)} - \frac{1}{(Z - Z_0 - d/2)}\right], \tag{5.1}$$

where d is the distance of the charge and its image charge, Z_0 is the offset from the image plane, q the electron charge and V_0 background potential. A sample of a vertical dipole potential (grey line) is plotted into figure 5.8 b): The dipole far field approximation $Z \gg d$ does not hold here anymore. Assumptions for the plotted model, fitting well through the first 5 data points are: $d = 3$ Å, $Z_0 = -1.7$ Å, $q = -4.5 \cdot 10^{-3} e^-$, $V_0 = 340$ mV. The curve represents a test and not a fit, two parameters, e.g. d and Z_0, had to be fixed to allow for a 'fitting' of q and V_0.

The chosen parameters for the plot-model of figure 5.8 b), e.g. the resulting distances between the Au surface and the negative charge $d/2 = d(\text{O-Au}) = 1.5$ Å, seem too small (on alkoxide O-Au bonds ~ 2 Å are typical bond lengths, similar also with metal amide bonds (N-Cu) [81, 161, 162]). Also the resulting tip-oxygen distance of ~ 0.3 Å is smaller than the experimentally observed tunneling and Δf values suggest (see sec. 5.2.2). Choosing larger distances, the effective charge would have to be chosen smaller, which is not reasonable - or the exponent n of the $(Z - Zo \pm d/2)^n$ term would have to be chosen (much) larger than one. Unfortunately we do not yet have enough data points at close distances to allow a real fit and conclude what the distance dependence is exactly like, but an *LCPD* decay faster than that of a monopole or dipole is reasonable. At the tip-sample distances of these results, the complex distribution of charge from the indoline group and the neighbor molecules reduces the validity of the simple fitting model in fig. 5.8 b). This can be explained by the following consideration.

Figure 5.9 shows a scheme of the two situations, the tip at close distance Z (a) and the tip at farther distance Z' (b) from the dipole $\vec{\mathbf{p}}$. Another dipole $\vec{\mathbf{q}}$ is located at a distance

d from the tip. In the first case (figure 5.9 a) the distance to dipole $\vec{\mathbf{p}}$ is much smaller than to $\vec{\mathbf{q}}$ ($Z < d$). For small distances Z one can assume $d \sim L$, where L is the distance between the dipoles (shown in fig. 5.9 b). Small changes in the Z distance have a large influence on the measured dipole potential value of the dipole $\vec{\mathbf{p}}$ due to $V_{\vec{\mathbf{p}}} \propto\sim 1/Z^2$, while the value of the potential from $\vec{\mathbf{q}}$ changes much less.

In figure 5.9 b) the tip distance Z' to the dipole $\vec{\mathbf{p}}$ is larger, so that it is comparable to the distance d' to dipole $\vec{\mathbf{q}}$. Now both dipole potentials change by comparable amounts on the same Z' scale, thus both have to be considered (and would partially cancel each other in the sketched situation with opposite directed dipoles). This geometric consideration explains the high resolution on the atomic scale for this experimental method at small (average) tip-sample distances.

The real charge distribution among the merocyanine dimer chains is far more complex than the simplified model of figure 5.9 a) and b). The assumption of point charges within the molecule is too much simplified on small Z distances. Moreover, within a radius of 10 Å (lateral) around the nitrophenolate group are already three positively charged indoline groups and two more negatively charged nitrophenolate groups. The charges of the neighboring molecules give rise to higher order (multipolar) electrostatic terms whose effects become more important as the tip is retracting. An additional approximation of this fitting model can be attributed to the fact that we had to neglect the shape of the tip. It has also been reported that image charges (and dipoles) in the tip may play an important role for the $LCPD$ and $\Delta f(LCPD)$ at small average tip-sample distances (see sec. 1.2.6, [51, 163]).

These results clearly demonstrate that we are able to map the localized charge densities within a single molecule. Their short range decay (in the order of $\Delta Z \leq 5$ Å in figure 5.8 b) suggests an effective screening by the substrate, but also the mutual cancellation of charges of opposite sign. The observed intramolecular charge localization does confirm the survival of the intramolecular dipole. But due to the dimer chain's structural arrangement, the molecular dipoles cancel each other and an overall smaller positive charge of the chains remains effective outside the dimer chains.

Due to the non-uniform distribution of positive charge all over the bulky methyl groups of the indoline side of the molecule (figure 5.7 a) a fit of the electrostatic potential would be even more difficult than for the previously discussed nitrophenolate group. Unfortunately we could not observe an $LCPD$ inversion like in figure 5.6 a) on top of the di-methyl group, even though the $\Delta f(LCPD)$ values (not shown) were reaching positive values, which indicates repulsive forces between tip and the di-methyl.

5.2.2. Correlation Between Tip-Molecule Distance and $LCPD$ Contrast Inversion

In order to understand the $LCPD$ contrast inversion, we correlate the constant height data with the constant current data. To connect them, we look for the line of intersection between the constant height map 5.6 a) and the constant current profile 5.7 a). The AFM is a perfect tool to investigate tip-molecule interactions as a function of the distance. We

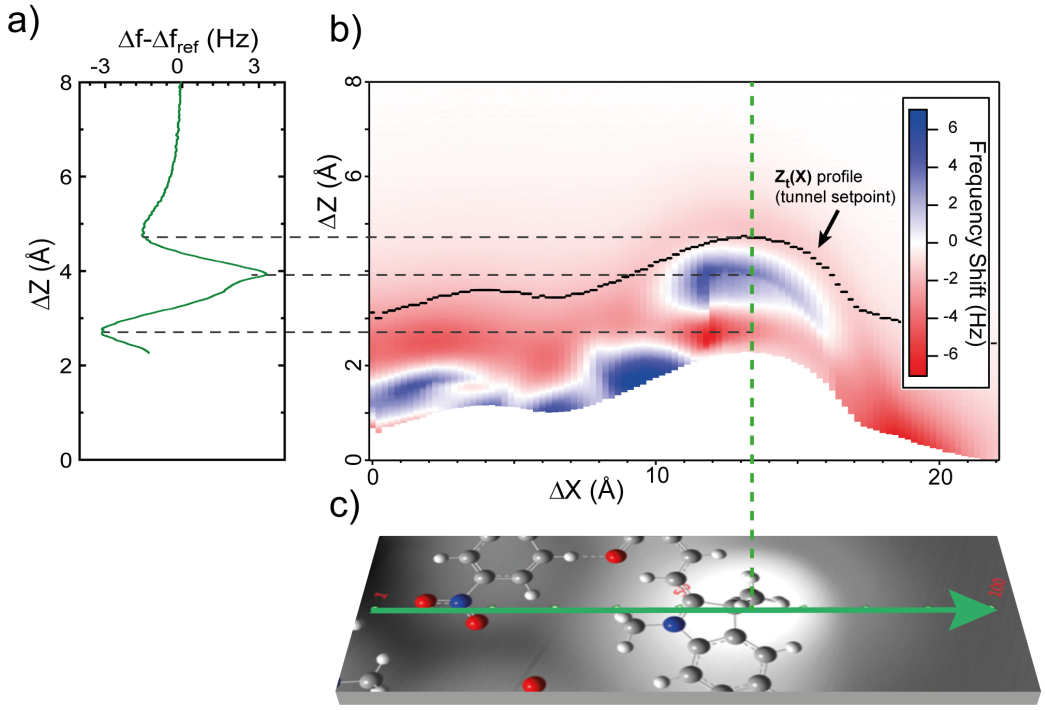

Figure 5.10.: a) Single $\Delta f(Z)$ spectra, extracted from the spectral map (b) at the vertical dashed green line. **b)** $\Delta f(Z)$ spectral map along a constant current line profile over a merocyanine dimer. The black line "$Z_t(X)$" indicates the constant current profile of the tip motion over the dimer at the given setpoint ($V_s = 1.02$ V, $I_t = 220$ pA). **c)** STM image of the MC dimer with the $\Delta f(Z)$ profile (green line) and the structural model superimposed.

measured the frequency shift as a function of the tip-sample distance on a profile similar to the *LCPD* line profile figure 5.7 a).

Figure 5.10 b) shows a $\Delta f(X,Z)$ spectral map measured along a constant current profile (green line in figure 5.10 c) over a MC dimer, consisting of 100 individual $\Delta f(Z)$ spectra. The black line labeled '$Z_t(X)$ profile' is the constant tunneling current profile over the molecules. All $\Delta f(Z)$ spectra were acquired the following way: first the feedback loop was opened and the sample bias set to 3 mV, then the tip was quickly retracted by an offset and subsequently slowly approached. Our spectral map shows the $\Delta f(Z)$ curves of approaching the tip, starting from Z values far away from the sample. The points of closest tip-sample distances during an approach are 2.5 Å towards the sample, measured from the indicated black $Z_t(X)$ profile. A reference spectrum, taken on the bare Au(111) surface in large lateral distance from the molecules was subtracted from the individual $\Delta f(Z)$ spectra, to remove long-range attractive forces [22]. In this way only the short range tip-molecule forces remain.

A processed $\Delta f(Z)$ curve taken on the di-methyl group (indicated by the vertical dashed green line) is shown in figure 5.10 a). One can clearly identify the two $\Delta f(z)$

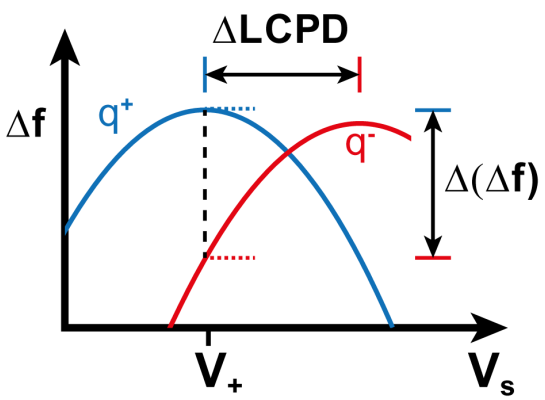

Figure 5.11.:
Sketch: how the $LCPD$ contrast inversion may affect the $\Delta f(Z)$ spectra. The two parabolas are centered at different $LCPD$. At a fixed $V_s = V_+$ and Z the shift of a parabola from blue (positive charge $q+$) to red (negative charge $q-$) will be observed as a decrease in Δf.

minima and also the maximum at $\Delta Z = 4$ Å. The second crossing of $\Delta f = 0$ is observed at $\Delta Z \sim 3$ Å. We interpret this as a weak bond formation with the tip, followed by repulsive interaction, where the upper methyl of the di-methyl group is pushed with the tip [45, 102, 147].

A closer look to the $\Delta f(Z)$ spectral map fig. 5.10 b) from $\Delta X = 12$ Å and $\Delta Z = 3.9$ Å reveals a discontinuity in the $\Delta f(Z)$. The same feature appears in the single spectrum 5.10 a) after the Δf maximum at $\Delta Z \leq 3.9$ Å (middle horizontal dashed line). A closer examination into single $\Delta f(Z)$ spectra shows, that the frequency shift decreases by $\sim$ 1 Hz upon a tip approach of only 0.05 Å. This feature is likely an effect of the $LCPD$ inversion.

Figure 5.11 sketches the effect of a $LCPD$ inversion (a horizontal shift of the $\Delta f(V_s)$ parabola) on $\Delta f(V_s = \text{constant})$. All the $\Delta f(Z)$ spectra were recorded with a sample bias of 3 mV. A shift of a $\Delta f(V_s)$ parabola (due to $LCPD$ inversion) from a $LCPD$ of 50 mV to a $LCPD = 800$ mV results in a decrease of the frequency shift by $\sim$ 1.5 Hz, which is compatible with our observation. Therefore this feature can be interpreted as a fingerprint for the $LCPD$ inversion.

An additional link to connect the constant height map with the constant current data is the tunneling conductance: we compare the different conductance values on top of the di-methyl at a sample bias of $V_s = 1$ V. Table 5.1 lists the conductance values for the

	Conductance at $V_s = 1$ V
const. current $LCPD$ map fig. 5.4 c)	$2 \pm 1 \times 10^{-6} G_0$
const. current line profile fig. 5.7 a)	$6 \pm 1 \times 10^{-6} G_0$
const. height $LCPD$ map fig. 5.6 a) (contrast inversion)	$3 \pm 2 \times 10^{-5} G_0$
const. current $\Delta f(Z)$ profile. 5.12 a) (at closest approach)	$3 \pm 2 \times 10^{-4} G_0$

Table 5.1.: Conductance on top of the di-methyl group

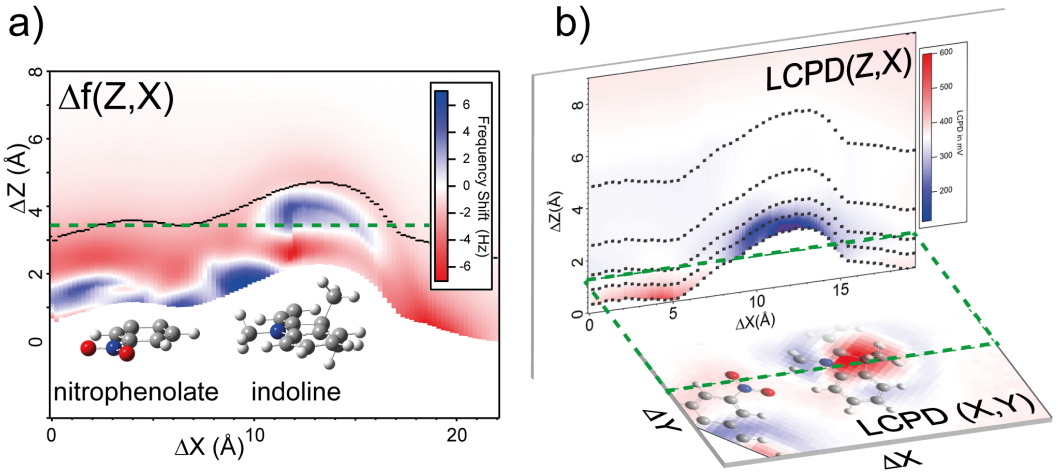

Figure 5.12.: a) $\Delta f(Z,X)$ spectral map from fig. 5.10 b). The green dashed line denotes the intersection line with a constant height map like figure 5.6 a) (also shown in b) **b)** $LCPD(Z,X)$ map from fig. 5.7 a) together with the constant height map figure 5.6 a). The green dashed line denotes the intersection line of the two maps along the ΔX axis.

different measurements: we find that the conductance at the $LCPD$ contrast inversion (fig. 5.6 a) is one order of magnitude higher than on the constant current $LCPD$ map (fig. 5.4 c) and line profile (fig. 5.7 a), which corresponds to a ΔZ height difference of ~ 1 Å.

From the correlation of the conductance values of constant height maps and constant current map and profiles we find the constant height map figure 5.6 a) corresponds to a cut in the $\Delta f(Z,X)$ spectral map figure 5.10 b) at $\Delta Z \sim 3.5$ Å. Figure 5.12 a) shows this line of intersection at the green dashed line. On top of the di-methyl $\Delta f(Z)$ is positive but already decreasing (for $\Delta Z \rightarrow 0$ Å). Due to the $\Delta f(Z)$ maximum at $\Delta Z \sim 4$ Å we have observed similar positive Δf values, while the tip was in different interaction regimes, either in the regime of contrast inversion or at higher Z.

Figure 5.12 b) shows the line of intersections between the constant current $LCPD$ profile figure 5.7 a) and the constant height map figure 5.6 a) (dashed green lines along ΔX). The ΔZ offset value of the intersection line was estimated on basis of the conductance values. In the $LCPD(Z)$ line profile the tip is about 1 Å in ΔZ direction farther away from the di-methyl than at the contrast inversion in the constant height map fig. 5.6 a).

This means the $LCPD$ inversion happens only in the region of repulsive short range interaction, where $\Delta f(Z)$ is already decreasing towards its second minimum. We interpret this such, that the upper methyl of the di-methyl is pushed by the tip [45, 102, 147, 158]. The tip is then very close to the molecular positive charge, here a methyl group at the indoline side of the MC molecule.

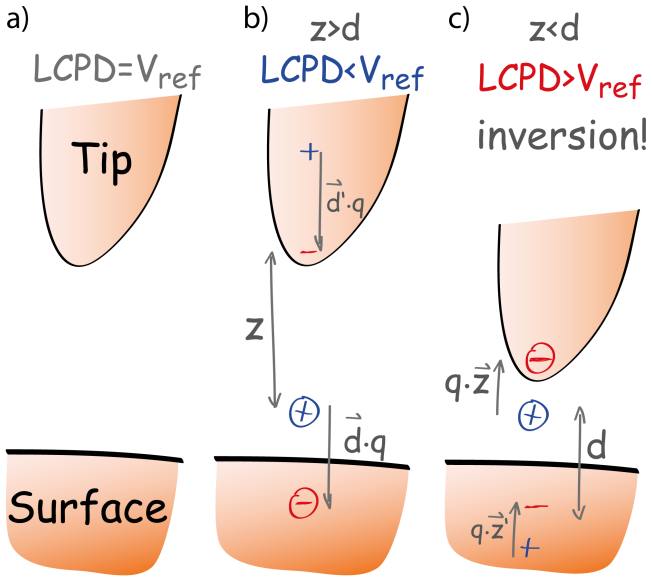

Figure 5.13.: $LCPD$ contrast inversion model **a)** Reference case of a metal tip and surface, to which the $LCPD$ refers. **b)** The tip is far from the positive point charge. The $LCPD$ is negative: a negative sample bias can compensate the electrostatic forces between the dipole $q \cdot \mathbf{d}$ and tip. **c)** The tip is closer to the positive charge, than the dimension of the molecule-surface dipole. The positive molecule induces a negative image charge in the tip, instead. A positive bias can compensate the electrostatic forces between the dipoles $q \cdot \mathbf{Z}$ and surface.

5.2.3. A Simple Electrostatic Model

The inversion of the $LCPD$ by approaching the tip into a repulsive short range interaction with the di-methyl has been confirmed in the $LCPD$ constant height maps (fig. 5.6 a) and is indicated in the $\Delta f(Z)$ spectral maps (fig. 5.10 a), too. Three possibilities can be considered to explain this inversion.

I) The contact of the tip with the molecule results in a charge transfer between tip and molecule, so that the molecule becomes negatively charged.

To have an effective charge transfer, a metal-organic coordination bond would need to form between the gold tip and the methyl side of the molecule. This is unlikely, since methyl groups are usually chemically not very reactive, as the hydrogens shield and saturate the carbon bonds [164]. Upon such contact formation one observes usually stronger, step-like increase of the conductance [24, 82], while we found no nonlinearity in the current-distance trace over the transition region (data not shown here). Also the force gradient should show a nonlinear change upon contact formation, which we did also not observe [24] (the observed $\Delta f(Z)$ step (figure 5.10 a,b) is a sharp, but continuous transition).

II) The observed repulsive force on the methyl group may bend the methyl away from the tip. This might lead to a distortion of the indoline side of the MC molecule, and modify the charge redistribution within the molecule. However, this would rather lead to an electronically more neutral molecule, than to a sudden negatively charged indoline group.

III) As the tip pushes the methyl group, it approaches also close to the positive charge, distributed over the methyl groups. In our model we consider a simplified Kelvin probe method picture, as sketched in figure 5.13. The reference case (a) includes only the tip and the surface. We assume no electrostatic forces and define $V_s = LCPD_a = 0$.

We describe the molecule's di-methyl group simplified as a single positive point charge q on the surface (sketched in fig. 5.9 b) as blue $\oplus$). The positive charge on the surface creates a negative image charge $\ominus$ in the surface. Both charges are separated by a distance d and form the dipole $q \cdot \mathbf{d}$. With $Z > d$, an image dipole $q \cdot \mathbf{d}'$ is induced in the tip. The attractive forces between them can be minimized by applying a more negative sample bias $V_s = LCPD_b < 0$. This is the typical case as we observe it e.g. in fig 5.4 c) on the di-methyl at the indoline group.

When the tip approaches the positive charge to distances $Z < d$, as shown in the sketch in fig. 5.9 c), the positive molecule charge q induces a negative image charge in the tip, creating the dipole $q \cdot \mathbf{Z}$. The dipole $q \cdot \mathbf{Z}$ induced an image dipole $q \cdot \mathbf{Z}'$ in the surface, leading also to attractive electrostatic forces. But now a positive sample bias $V_s = LCPD_c > 0$ is needed to compensate them. This situation could describe a $LCPD$ contrast inversion as observed in fig. 5.6 a).

In the latter model no intramolecular charge distributions are changed. It is rather a change of the experimental setup: our former sample - here the methyl next to the tip from the indoline part of the molecule - has become the probe, now probing the surface. However, the latter approach is rather phenomenological. More experiments can help here to get a better understanding of the process and to further support or exclude some of the listed processes. Also here functionalized tips would largely affect or even suppress the $LCPD$ contrast inversion. A non-metallic CO, Cl or Xe tip would e.g. shift the point of contrast inversion (assuming model III) to smaller Z distances.

5.3. Conclusion and Outlook

In this chapter we have investigated the open-form isomer of the ring opening-closing switch 1,3,3-Trimethylindolino-6'nitrobenzopyrylospiran, called here merocyanine (MC), adsorbed on Au(111).

The MC form exhibits a strong dipole moment due to an intramolecular charge donation from the indoline nitrogen to the delocalized π-system. We could show by $LCPD$ measurements that the zwitterionic character of the molecule is preserved on the surface. Electron accumulation is localized on the oxygen atoms of the nitrophenolate side, while electron depletion is observed over the methyl groups of the indoline side of the molecules. However, the fast decay of the electrostatic potential of the positive and negative charges suggests a strong screening by the surface electrons and also the mutual cancellation of the dipoles of neighboring molecules. Thus, no net dipole moment exists, but an overall smaller charge depletion among the merocyanine dimer chains. $LCPD$ spectra with more resolution in vertical direction could give better insight on the screening process and might then also give the possibility to quantify the partial charges within the sites of the molecule. A comparison to the closed neutral form of the molecule, the

so called spiropyran form, by AFM $LCPD$ measurements is planned as well.

We compared the electrostatic potential maps with DFT calculations and could identify the orientation of the nitrophenolate group in the MC dimer chain structure. An evaluation of short range interactions from $\Delta f(Z)$ spectra allowed us to assign the protrusion, observed in constant current STM topography, to the di-methyl side. With these observations we could improve the structural model of the MC dimer chains.

We observed an inversion of the $LCPD$ in a regime of repulsive forces between the tip and the di-methyl site of the indoline group in $\Delta f(V_s)$ spectra and found indications of the inversion also in $\Delta f(Z)$ spectra. Here we sketched 3 possible explanations, from which the third appears most plausible at the present level. We interpreted it such, that the molecular positive charge is closer to the tip than to the surface and becomes effectively part of the tip, probing the surface.

To improve our understanding of the $LCPD$ inversion process, we will continue the investigations with higher vertical resolution and closer approaches performing $\Delta f(V_s)$ spectroscopy. Different tip functionalization can help us to identify the length scales of the process. DFT calculation including a metal surface and metal tip are also considered, as they can deliver a detailed picture of the charge distribution within the system.

Chapter 6.

Summary

In this thesis we presented four different experiments that deal with fundamental properties of single molecule junctions. The experiments were carried out in a cryogenic STM/AFM in the tuning fork based qPlus design. The machine was newly constructed in the beginning of the thesis and successfully put into operation.

In particular we have shown in chapter 2 the lifting of the molecular wire 1,4-**b**is(**p**yridin-4-yl**e**thynyl)**b**enzene (BPEB) from a copper surface and could picture the lifting process with enormous detail. During the lifting we observed an atypical increase of the wire conductance, that originated from a structural change in the molecular junction. DFT simulations revealed that a pyridine ring rotation simultaneously with a sp to sp^2 rehybridization of one carbon atom was correlated with the increase in the conductance. The rehybridization led to an additional C-Cu bond, that gave rise to a direct current path into the metallic substrate. We could identify the structural change by a characteristic nonlinearity in $\Delta f(Z)$ spectra, correlated with the simultaneously measured conductance. An evaluation of the elastic regime between plastic steps allowed us to obtain energy (159 meV) and force (360 pN) values associated with the bond formed at the rehybridization. The disagreement of simulated force field $dF/dZ(Z)$ spectra with the experiment confirmed that the electronic structure, which allows for rehybridization, is essential to explain the conductance and Δf features. While DFT seemed to overestimate the binding energy ($\sim$ 1 eV) we found qualitative agreement between the experimental and the simulated lifting curves obtained from DFT.

In chapter 3 we observed the self-oscillation of a macroscopic AFM tuning fork caused by the stochastic motion of a hydrogen molecule. The H_2 molecule can lie in different adsorption states within a tunneling junction. Inelastic tunneling electrons could at a certain threshold voltage V_{th} trigger stochastic fluctuations between these states. The states were associated with different tip-forces in the order of hundreds of piconewtons. In spectra of $\Delta f(V_S)$ appeared two regimes of different Δf, associated with the H_2 molecular states and a nonlinear transition at V_{th}. The spectral distribution of the stochastic switching varied with the sample bias and the tunneling current. In a regime where the fluctuation rate matched the resonance frequency of the tuning fork oscillator, we observed negative damping and even self-oscillation of the tuning fork. The H_2 fluctuation provided more than 50 meV of kinetic energy per TF oscillation cycle. The

underlying effect has been identified as stochastic resonance. While the H_2 fluctuations exerted a force on the tip, the rate of the fluctuations was modulated by the vertical oscillation of the tip. The concerted dynamics of the molecular bi-stability and the tip oscillation created a coherent pathway to transfer energy from a noisy source into periodic motion.

In chapter 4 we studied the effect of the (dis)charging of TCNQ molecules on the dynamics of the AFM tuning fork in the charge transfer complex tetramethyltetrathiafulvalene-tetracyanoquinodimethane (TMTTF-TCNQ). TCNQ molecules exist here in a neutral or anionic ground state and could be charged or discharged, respectively, in the electric field between tip and surface. The (dis)charging appeared as a dip (charging) or peak (discharging) in $dI/dV(V_s)$ spectra. The critical field for (dis)charging depended on the distance between tip and molecule if the bias voltage was fixed. Thus, the oscillation of the AFM tip allowed for a periodic discharging-recharging cycle. In spectra of Δf the (dis)charging became manifested as a dip at the discharging voltage. We performed $\Delta f(V_s)$ spectroscopy and observed shifts of the $LCPD$ and the $\Delta f(V_s = LCPD)$, indicative for the respective charge state of a TCNQ molecule. The (dis)charging dip in Δf spectra originated from the discharging event, caused by a small non-linear change of the electrostatic force. We obtained an estimate for the force difference between the $TCNQ^-$ charge states of $\sim$ 13 pN. Throughout the measurements we observed no tip-sample dissipation. We concluded from this that the (dis)charging process is too fast and that it involves no structural rearrangements that comprise a change of the electric field strength needed for the (dis)charging. In $dI/dV(V_s)$ and $\Delta f(V_s)$ spectral maps along chains of TCNQ molecules we observed indications for a mutual influence of the molecular charge states: a discharged $TCNQ^-$ could become recharged when its neighbors became discharged.

In the last experiment (chapter 5) we investigated the intramolecular charge distribution of the zwitterionic merocyanine (MC) form of the molecular switch 1,3,3-Trimethylindolino-6'nitrobenzopyrylospiran. MC adsorbed on Au(111) forms chains of molecular dimers. The question we had was if the dipole moment of the molecule survives on the surface. From $\Delta f(V_s, X, Y)$ spectra we obtained spatially high resolved $LCPD$ maps and could confirm an intramolecular charge distribution similar as in the molecule in gas phase. In comparison with DFT simulations of the electrostatic potential of MC, the $LCPD$ maps helped us also to improve the former structural MC dimer model. A study of the vertical evolution of the molecular electrostatic potential showed an effective screening of the intramolecular charges by the substrate and by the arrangement of the charges in the neighbor molecules. At repulsive distances (contact regime) between the tip and a methyl group of the MC molecules we observed an atypical inversion of the $LCPD$. We interpreted the effect as an inversion of the sample-probe system. When the tip contacted the molecule, it became a part of the tip and probed the surface.

Appendix A.

Modelling by MM3 Force Field Calculations

Force field molecular mechanics calculations were performed utilizing the force field parameter set MM3 [86–88]. These provide most parameters for modelling organic molecules in gas phase with adequate accuracy to simulate intramolecular and intermolecular forces. Yet, we had to made certain amendments to the parameter set for the simulated lifting of the 1,4-bis(pyridin-4-ylethynyl)benzene [165]. These were regarding the copper atom (to simulate a tip), attached to a nitrogen atom of a pyridine ring.

To simulate the lifting from a surface, we modeled a slab of Cu atoms and placed a molecule on top, using the Tinsurbui command line tool from Gunnar Schulze [166]. The metal parameters were obtained also from [165].

In order to simulate a metal-coordination alike bond from the nitrogen atom of the second pyridine ring to the substrate, we defined pairwise Morse potentials between the N atom and the first layer atoms of the Cu surface.

The simulations were performed using the open source molecular modeling package Tinker [89], modified such, that pairwise Morse potentials can be defined between atoms.

A typical lifting energy vs. distance spectrum was obtained by repeating the following steps (initially starting from a minimized structure): I) displace the tip-Cu atom in Z-direction, II) minimization of the molecular structure while freezing the Cu atoms (utilizing the Newton method [167]), III) analysis of the structure to obtain the total energy of the system and finally start over with I).

Figure A.1 is the complete BPEB molecule lifting curve obtained from a MM3 force field simulation. The red frame surrounds the regions from the beginning to the end of the ring rotation (features 'B' to 's2' in fig. 2.7). Overall, the curve shows no similarities to the experimental lifting spectrum fig. 2.7 a). The sharp spikes in the dF/dZ curve A.1 a) are due to plastic structural changes in the tip-molecule junction. At $Z = 20$ Å the vertical stiffness increases to 25 N/m due to the molecule standing upright between tip and surface. The following dF/dZ (and also Force(Z)) curvature is due to the Morse potential bond of the last N atom above the surface and is indeed characteristic for the last step of the detachment of a molecule from the surface. We find an overall agreement with lifting and force field simulations as reported from the group of S. Tautz

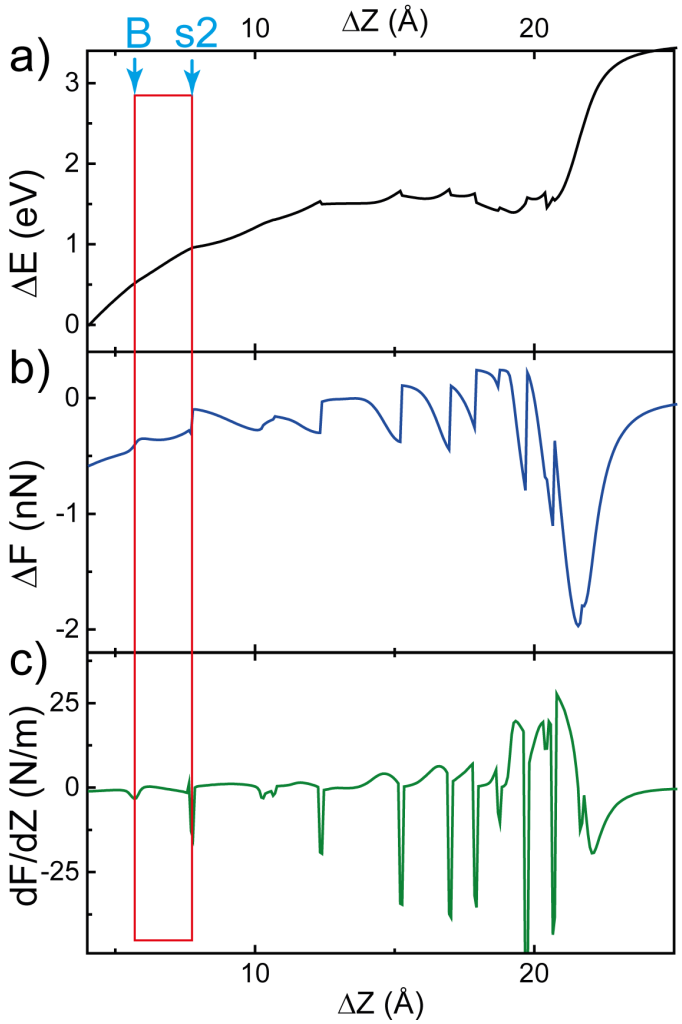

Figure A.1.:
a) Energy vs. Z, obtained from force field calculations and the derivatives in Z-direction: **b)** force and **c)** force gradient vs. tip-sample Z distance. The red frame surrounds the regions from the beginning to the end of the ring rotation (corresponding to the features 'B' to 's2' in fig. 2.7).

[24, 103]. They investigated the PTCDA molecule, which is more rigid and it is more two-dimensional compared to the rather 1-dimensional BPEB. Therefore PTCDA can slide smoother over the surface (like a sheet). Especially a rehybridization of one of its atoms with the surface is very unlikely.

Appendix B.

Nonlinearity of a Molecular H_2 Junction

The modeling of the H_2 driven tuning fork self oscillation with a stationary oscillation amplitude requires a nonlinear force term in the equation of motion, otherwise the effective *negative damping* would lead to an undamped (infinite) increase of the oscillation amplitude. Indeed, we could experimentally prove the existence of the nonlinearity in the coupled tuning fork-H_2 oscillator, originating from nonlinear tip-sample forces. Figure B.1 a) shows the oscillation amplitude A_{osc} of the tuning fork as a function of the driving frequency (at constant driving amplitude $A_D = 50$ mV). The tip is approached to tunneling distance on the H_2 covered surface ($V_s = -30$ mV, $I_t = 0.58$ nA). The hysteresis

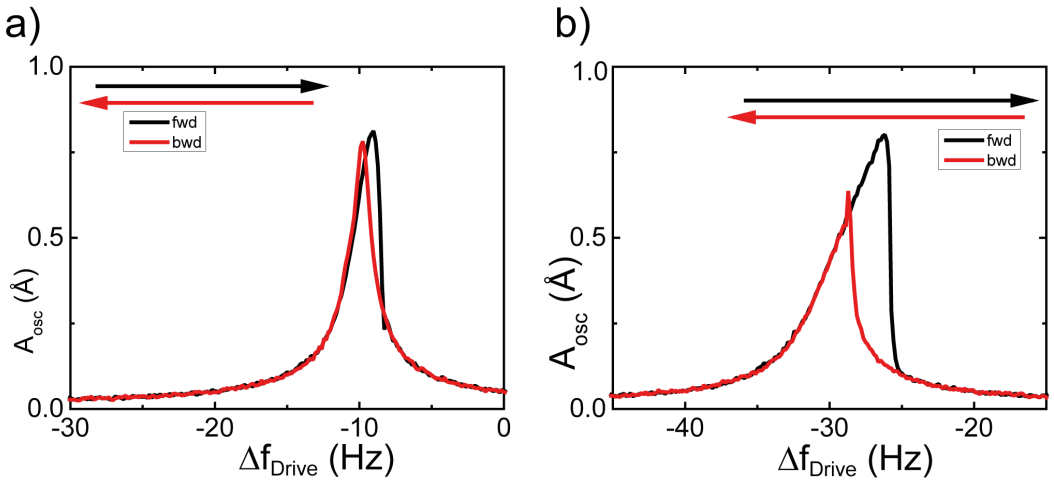

Figure B.1.: Nonlinearity of a molecular hydrogen junction. **(a)** Oscillation amplitude A_{osc} of the tuning fork as a function of the driving frequency (at constant $A_D = 50$ mV). For the black (red) line the excitation frequency was scanned from small (large) to larger (smaller) frequency. The hysteresis is an effect of the nonlinearity of the junction. The actual resonance frequency is shifted to $\sim$ -10 Hz from the resonance frequency ($f_0 = 20610.1$ Hz) of the free lever. The tip-sample distance on the hydrogen covered surface is determined by a tunnel current feedback ($V_s = -30$ mV, $I_t = 0.58$ nA). **(b)** Same experiment as a) but at smaller tip-sample distance ($V_s = 25$ mV, $I_t = 50$ nA). Due to the closer tip approach the actual resonance frequency is shifted to $\sim$ -30 Hz from the resonance frequency ($f_0 = 20610.1$ Hz) of the free lever . The hysteresis is more pronounced in b) (the Δf axis range is in both cases a) and b) 30 Hz, thus comparable).

in the A_{osc} vs. f_{drive} resonance curves appears, when the sweep of the frequency scan is repeated in reversed Δf direction and is typical for a nonlinear -e.g. Duffing- oscillator. Figure B.1 b) shows the same experiment but with closer tip approach, determined by the tunneling setpoint ($V_s = 25$ mV, $I_t = 50$ nA). The hysteresis is more pronounced, which is caused by a larger effect of the nonlinearity due to a closer tip-sample distance.

Routinely we scan the resonance peak of the tuning fork out of tunnel to calibrate the TF sensor every day. We use then driving amplitudes up to 1 V and observe correspondingly large oscillation amplitudes. In these measurements the resonance curves are symmetric, as in a linear harmonic oscillator. Thus we conclude, that the observed nonlinearities originate from nonlinear tip-sample forces.

List of Abbreviations

(nc-)**AFM**	(non-contact-) atomic force microscopy
BPEB	1,4-bis(pyridin-4-ylethynyl)benzene
(L)**DOS**	(local) density of states
DFT	density functional theory
H_2	(molecular) hydrogen
HOMO	highest occupied molecular orbital
KPFM	Kelvin probe force microscopy
LCPD	local contact potential difference
LUMO	lowest unoccupied molecular orbital
MC	merocyanine
(LT)**STM**	(low temperature) scanning tunneling microscopy
STS	scanning tunneling spectroscopy
TCNQ	tetracyanoquinodimethane
TMTTF	tetramethyltetrathiafulvalene
TF	tuning fork
UHV	ultra high vacuum
vdW	van der Waals

References

[1] Feynman, R. There's plenty of room at the bottom. *Engineering and Science* (1960).

[2] Binnig, G. & Rohrer, H. Tunneling through a controllable vacuum gap. *Applied Physics Letters* **40**, 178–180 (1982).

[3] Binnig, G. & Quate, C. F. Atomic Force Microscope. *Physical Review Letters* **56**, 930–933 (1986).

[4] Binnig, G., Gerber, C., Stoll, E., Albrecht, T. R. & Quate, C. F. Atomic Resolution with Atomic Force Microscope. *Europhysics Letters (EPL)* **3**, 1281–1286 (1987).

[5] Barth, J., Brune, H., Ertl, G. & Behm, R. Scanning tunneling microscopy observations on the reconstructed Au(111) surface: Atomic structure, long-range superstructure, rotational domains, and surface defects. *Physical Review B* **42**, 9307–9318 (1990).

[6] Giessibl, F. J. Atomic resolution on Si(111)-(7x7) by noncontact atomic force microscopy with a force sensor based on a quartz tuning fork. *Applied Physics Letters* **76**, 1470 (2000).

[7] Loth, S., Baumann, S., Lutz, C. P., Eigler, D. M. & Heinrich, A. J. Bistability in atomic-scale antiferromagnets. *Science (New York, N.Y.)* **335**, 196–9 (2012).

[8] Koumura, N., Zijlstra, R. W., van Delden, R. a., Harada, N. & Feringa, B. L. Light-driven monodirectional molecular rotor. *Nature* **401**, 152–5 (1999).

[9] Fletcher, S. P., Dumur, F., Pollard, M. M. & Feringa, B. L. A reversible, unidirectional molecular rotary motor driven by chemical energy. *Science (New York, N.Y.)* **310**, 80–2 (2005).

[10] Kudernac, T. *et al.* Electrically driven directional motion of a four-wheeled molecule on a metal surface. *Nature* **479**, 208–11 (2011).

[11] Liljeroth, P., Repp, J. & Meyer, G. Current-induced hydrogen tautomerization and conductance switching of naphthalocyanine molecules. *Science (New York, N.Y.)* **317**, 1203–6 (2007).

[12] Quek, S. Y. *et al.* Mechanically controlled binary conductance switching of a single-molecule junction. *Nature nanotechnology* **4**, 230–4 (2009).

[13] Alemani, M. *et al.* Electric field-induced isomerization of azobenzene by STM. *Journal of the American Chemical Society* **128**, 14446–7 (2006).

[14] Comstock, M. *et al.* Reversible Photomechanical Switching of Individual Engineered Molecules at a Metallic Surface. *Physical Review Letters* **99**, 1–4 (2007).

[15] Piantek, M. *et al.* Reversing the thermal stability of a molecular switch on a gold surface: ring-opening reaction of nitrospiropyran. *Journal of the American Chemical Society* **131**, 12729–35 (2009).

[16] Heise News, Jul. 2nd, 2012, Heise Zeitschriften Verlag GmbH & Co. KG, Hannover. UMC bekennt sich zur 20-Nanometer-Fertigungstechnik. *web site article, available online*
`http://www.heise.de/ct/meldung/UMC-bekennt-sich-zur-20-Nanometer-Fertigungstechnik-1630001.html`, visited: Jul. 15th 2013.

[17] Heise News, Dec. 22nd 2012 , Heise Zeitschriften Verlag GmbH & Co. KG, Hannover. Wettrennen um 14-Nanometer-Technik. *web site article, available online*
`http://www.heise.de/ct/meldung/Wettrennen-um-14-Nanometer-Technik-1774147.html`, visited: Jul. 15th 2013.

[18] UNESCO, 7, place de Fontenoy 75352 Paris 07 SP France . 'Memory of the World in the Digital Age: Digitization and Preservation', conference announcement. *web site, available online*
`http://www.unesco.org/new/en/communication-and-information/resources/news-and-in-focus-articles/all-news/news/international_conference_memory_of_the_world_in_the_digital_age_digitization_and_preservation/`, visited: Jul. 15th 2013.

[19] Zhirnov, V., Cavin, R., Hutchby, J. & Bourianoff, G. Limits to binary logic switch scaling-a gedanken model. *Proceedings of the IEEE* **9**, 1934–1939 (2003).

[20] Izydorczyk, J. & Izydorczyk, M. Microprocessor Scaling: What Limits Will Hold? *Computer* **43**, 20–26 (2010).

[21] Giessibl, F. J. Advances in atomic force microscopy. *Reviews of Modern Physics* **75**, 949–983 (2003).

[22] Gross, L., Mohn, F., Moll, N., Liljeroth, P. & Meyer, G. The chemical structure of a molecule resolved by atomic force microscopy. *Science (New York, N.Y.)* **325**, 1110–4 (2009).

[23] Gross, L. *et al.* Measuring the charge state of an adatom with noncontact atomic force microscopy. *Science (New York, N.Y.)* **324**, 1428–31 (2009).

[24] Fournier, N., Wagner, C., Weiss, C., Temirov, R. & Tautz, F. Force-controlled lifting of molecular wires. *Physical Review B* **84**, 16–18 (2011).

[25] Gahl, C. *et al.* Structure and excitonic coupling in self-assembled monolayers of azobenzene-functionalized alkanethiols. *Journal of the American Chemical Society* **132**, 1831–8 (2010).

[26] Binning, G., Rohrer, H., Gerber, C. & Weibel, E. Surface studies by scanning tunneling microscopy. *Phys. Rev. Lett.* **49**, 57–61 (1982).

[27] The nobel prize in physics 1986 – press release. *nobelprize.org* `http://nobelprize.org/nobel_prizes/physics/laureates/1986/press.html`, visited: 5.11.2008.

[28] Ho, W. Single-molecule chemistry. *The Journal of Chemical Physics* **117**, 11033 (2002).

[29] Giessibl, F. J. Atomic resolution of the silicon (111)-(7x7) surface by atomic force microscopy. *Science (New York, N.Y.)* **267**, 68–71 (1995).

[30] Edwards, H., Taylor, L., Duncan, W. & Melmed, A. J. Fast, high-resolution atomic force microscopy using a quartz tuning fork as actuator and sensor. *Journal of Applied Physics* **82**, 980 (1997).

[31] Torbrügge, S., Schaff, O. & Rychen, J. Application of the KolibriSensor to combined atomic-resolution scanning tunneling microscopy and noncontact atomic-force microscopy imaging. *Journal of Vacuum Science & Technology B: Microelectronics and Nanometer Structures* **28**, C4E12 (2010).

[32] Giessibl, F. J., Pielmeier, F., Eguchi, T., An, T. & Hasegawa, Y. Comparison of force sensors for atomic force microscopy based on quartz tuning forks and length-extensional resonators. *Physical Review B* **84**, 125409 (2011).

[33] Nolting, W. *Basic course on theoretical physics. 5: Quantum mechanics. Part 1: Foundations. (Grundkurs Theoretische Physik. 5: Quantenmechanik. Teil 1: Grundlagen.) 5. Aufl.* (Berlin: Springer. xvi, 424 S., 2002).

[34] Giaever, I. Electron tunneling between two superconductors. *Physical Review Letters* **5**, 464–466 (1960).

[35] Nicol, J., Shapiro, S. & Smith, P. H. Direct measurement of the superconducting energy gap. *Phys. Rev. Lett.* **5**, 461–464 (1960).

[36] Bardeen, J. Tunnelling from a many-particle point of view. *Phys. Rev. Lett.* **6**, 57–59 (1961).

[37] Tersoff, J. & Hamann, D. R. Theory of the scanning tunneling microscope. *Phys. Rev. B* **31**, 805–813 (1985).

[38] Lüth, H. *Solid Surfaces, Interfaces and Thin Films*. Graduate Texts in Physics (Springer Berlin Heidelberg, Berlin, Heidelberg, 2010).

[39] Kuypers, F. *Klassische Mechanik* (Wiley-VCH, Berlin, 2010).

[40] Giessibl, F. Forces and frequency shifts in atomic-resolution dynamic-force microscopy. *Physical Review B* **56**, 16010–16015 (1997).

[41] Sader, J. E. & Jarvis, S. P. Accurate formulas for interaction force and energy in frequency modulation force spectroscopy. *Applied Physics Letters* **84**, 1801 (2004).

[42] Jones, J. E. On the Determination of Molecular Fields. II. From the Equation of State of a Gas. *Proceedings of the Royal Society A: Mathematical, Physical and Engineering Sciences* **106**, 463–477 (1924).

[43] Kopitzki, K. & Herzog, P. *Einführung in die Festkörperphysik* (Vieweg+Teubner Verlag, Wiesbaden, 2007).

[44] Hamaker, H. The London-van der Waals attraction between spherical particles. *Physica* **4**, 1058–1072 (1937).

[45] Sun, Z., Boneschanscher, M. P., Swart, I., Vanmaekelbergh, D. & Liljeroth, P. Quantitative Atomic Force Microscopy with Carbon Monoxide Terminated Tips. *Physical Review Letters* **106**, 046104 (2011).

[46] Demtröder, W. *Experimentalphysik 2*. Springer-Lehrbuch (Springer Berlin Heidelberg, Berlin, Heidelberg, 2009).

[47] Kelvin, L. V. Contact electricity of metals. *Philosophical Magazine Series 5* **46**, 82–120 (1898).

[48] Nonnenmacher, M., O'Boyle, M. P. & Wickramasinghe, H. K. Kelvin probe force microscopy. *Applied Physics Letters* **58**, 2921 (1991).

[49] Lü, J. *et al.* Surface potential studies using Kelvin force spectroscopy. *Applied Physics A: Materials Science & Processing* **66**, S273–S275 (1998).

[50] Mohn, F., Gross, L., Moll, N. & Meyer, G. Imaging the charge distribution within a single molecule. *Nature Nanotechnology* **7**, 227–231 (2012).

[51] Mohn, F. Probing electronic and structural properties of single molecules on the atomic scale. *PhD Thesis* (2012).

[52] Stomp, R. *et al.* Detection of Single-Electron Charging in an Individual InAs Quantum Dot by Noncontact Atomic-Force Microscopy. *Physical Review Letters* **94**, 056802 (2005).

[53] Azuma, Y., Kanehara, M., Teranishi, T. & Majima, Y. Single Electron on a Nanodot in a Double-Barrier Tunneling Structure Observed by Noncontact Atomic-Force Spectroscopy. *Physical Review Letters* **96**, 016108 (2006).

[54] Ashcroft, N. W. & Mermin, N. D. *Solid State Physics* (Holt, Rinehart and Winston, New York, 1976).

[55] Bloch, F. Über die Quantenmechanik der Elektronen in Kristallgittern. *Zeitschrift für Physik* **52**, 555–600 (1929).

[56] Giessibl, F. Theory for an electrostatic imaging mechanism allowing atomic resolution of ionic crystals by atomic force microscopy. *Physical Review B* **45**, 13815–13818 (1992).

[57] Ibach, H. *Physics of Surfaces and Interfaces* (Springer, Berlin, 2006).

[58] Ploigt, H.-C., Brun, C., Pivetta, M., Patthey, F. & Schneider, W.-D. Local work function changes determined by field emission resonances: NaCl/Ag(100). *Physical Review B* **76**, 195404 (2007).

[59] Meyer, G. A simple lowtemperature ultrahighvacuum scanning tunneling microscope capable of atomic manipulation. *Rev. Sci. Instrum.* **67**, 2960 (1991).

[60] SPS-CreaTec GmbH. Magnusstr. 11, 12489 Berlin. *company web site, available online:*
`http://www.sps-createc.com/`, visited: Jun. 30th 2013.

[61] SPECS Zurich GmbH. Technoparkstrasse 1, 8005 Zurich, Switzerland. *company web site, available online:*
`http://www.specs-zurich.com/en/oc4-station-_content---1--1513.html`, visited: Jul. 7th 2013.

[62] VAb Vakuum-Anlagenbau GmbH. Marie-Curie-Str. 11, 25337 Elmshorn. *company web site, available online:*
`http://vab-vakuum.de`, visited: Jan. 20th 2013.

[63] Frohn, J., Wolf, J. F., Besocke, K. & Teske, M. Coarse tip distance adjustment and positioner for a scanning tunneling microscope. *Rev. Sci. Instrum.* **60**, 1200–1201 (1989).

[64] Corning SAS, Ophthalmic, 7 bis avenue de Valvins, 77167 Avon cedex, France. MACOR is a registered trademark of Corning Incorporated. *company web site, available online:*
`http://www.corning.com/WorkArea/showcontent.aspx?id=40321`, visited: Feb. 13th 2013.

[65] FEMTO Messtechnik GmbH. Klosterstr. 64, D-10179 Berlin. *company web site, available online:*
`http://www.femto.de/index.html?../products/dlpca.html`, visited: Jul. 7th 2013.

[66] Analog Devices, Inc., Corporate Headquarters. One Technology Way, Norwood, MA 02062-9106, USA. *company web site, pdf datasheet available online:* `http://www.analog.com/static/imported-files/data_sheets/AD823.pdf`, visited: Jul. 7th 2013.

[67] Stanford Research Systems, Inc. 1290-D Reamwood Avenue,Sunnyvale, CA 94089, USA. *company web site, available online:* `http://www.thinksrs.com/products/SR560.htm`, visited: Jul. 7th 2013.

[68] Epoxy technology. Product information sheet: EPO-TEK Thermal. *pdf datasheets on company web site, available online:* `http://www.epotek.com/categories.asp?ID=2`, visited: Jun. 30th 2013.

[69] Micro Crystal AG. *company web site, available online:* `http://www.microcrystal.com/`, visited: Jul. 5th 2013.

[70] Michaelson, H. B. The work function of the elements and its periodicity. *Journal of Applied Physics* **48**, 4729 (1977).

[71] Okamoto, H. & Massalski, T. B. The Au-Pd (Gold-Palladium) system. *Bulletin of Alloy Phase Diagrams* **6**, 229–235 (1985).

[72] Straumanis, M. E. & Yu, L. S. Lattice parameters, densities, expansion coefficients and perfection of structure of Cu and of Cu-In α phase. *Acta Crystallographica Section A* **25**, 676–682 (1969).

[73] Kim, Y. *et al.* Conductance and Vibrational States of Single-Molecule Junctions Controlled by Mechanical Stretching and Material Variation. *Physical Review Letters* **106**, 196804 (2011).

[74] Aradhya, S. V., Frei, M., Hybertsen, M. S. & Venkataraman, L. Van der Waals interactions at metal/organic interfaces at the single-molecule level. *Nature materials* **11**, 872–6 (2012).

[75] Meisner, J. S. *et al.* Importance of direct metal-π coupling in electronic transport through conjugated single-molecule junctions. *Journal of the American Chemical Society* **134**, 20440–5 (2012).

[76] Böhler, T., Grebing, J., Mayer-Gindner, A., Löhneysen, H. V. & Scheer, E. Mechanically controllable break-junctions for use as electrodes for molecular electronics. *Nanotechnology* **15**, S465–S471 (2004).

[77] Dr. Mario Ruben. Karlsruher Institut für Technologie. *work group website, available online*
`http://www.ruben-group.de/`, visited: Jul. 12th 2013.

[78] Xing, Y. *et al.* Optimizing single-molecule conductivity of conjugated organic oligomers with carbodithioate linkers. *Journal of the American Chemical Society* **132**, 7946–56 (2010).

[79] Lafferentz, L. *et al.* Conductance of a single conjugated polymer as a continuous function of its length. *Science (New York, N.Y.)* **323**, 1193–7 (2009).

[80] Henningsen, N. *et al.* Inducing the Rotation of a Single Phenyl Ring with Tunneling Electrons. *Journal of Physical Chemistry C* **111**, 14843–14848 (2007).

[81] Henningsen, N., Rurali, R., Franke, K. J., Fernández-Torrente, I. & Pascual, J. I. Trans to cis isomerization of an azobenzene derivative on a Cu(100) surface. *Applied Physics A* **93**, 241–246 (2008).

[82] Schulze, G. *Elementary Processes in Single Molecule Devices: Electronic Transport and Molecular Isomerization*. Ph.D. thesis (2009).

[83] Henningsen, N. *Azobenzene based Molecular Switches on Noble Metal Surfaces: Structure and Isomerization at the Nanometer Scale*. Ph.D. thesis (2009).

[84] Schmaus, S. *et al.* Giant magnetoresistance through a single molecule. *Nature nanotechnology* **6**, 185–9 (2011).

[85] Koch, M., Ample, F., Joachim, C. & Grill, L. Voltage-dependent conductance of a single graphene nanoribbon. *Nature nanotechnology* **7**, 713–7 (2012).

[86] Allinger, N. L., Yuh, Y. H. & Lii, J. H. Molecular mechanics. The MM3 force field for hydrocarbons. 1. *Journal of the American Chemical Society* **111**, 8551–8566 (1989).

[87] Lii, J. H. & Allinger, N. L. Molecular mechanics. The MM3 force field for hydrocarbons. 2. Vibrational frequencies and thermodynamics. *Journal of the American Chemical Society* **111**, 8566–8575 (1989).

[88] Lii, J. H. & Allinger, N. L. Molecular mechanics. The MM3 force field for hydrocarbons. 3. The van der Waals' potentials and crystal data for aliphatic and aromatic hydrocarbons. *Journal of the American Chemical Society* **111**, 8576–8582 (1989).

[89] Tinker home page. *web site, Software Tools for Molecular Design, available online* `http://dasher.wustl.edu/tinker/`, visited: Jun. 30th 2013.

[90] Yannoulis, P., Dudde, R., Frank, K. & Koch, E. Orientation of aromatic hydrocarbons on metal surfaces as determined by nexafs. *Surface Science* **190**, 519–528 (1987).

[91] Syomin, D., Kim, J., Koel, B. E. & Ellison, G. B. Identification of Adsorbed Phenyl (C 6 H 5) Groups on Metal Surfaces: Electron-Induced Dissociation of Benzene on Au(111). *The Journal of Physical Chemistry B* **105**, 8387–8394 (2001).

[92] Deprez, N. & McLachlan, D. S. The analysis of the electrical conductivity of graphite conductivity of graphite powders during compaction. *Journal of Physics D: Applied Physics* **21**, 101–107 (1988).

[93] Soler, J. M. *et al.* The SIESTA method for ab initio order- N materials simulation. *Journal of Physics: Condensed Matter* **14**, 2745–2779 (2002).

[94] Hohenberg, P. Inhomogeneous Electron Gas. *Physical Review* **136**, B864–B871 (1964).

[95] Kohn, W. & Sham, L. J. Self-Consistent Equations Including Exchange and Correlation Effects. *Physical Review* **140**, A1133–A1138 (1965).

[96] García-Gil, S., García, A., Lorente, N. & Ordejón, P. Optimal strictly localized basis sets for noble metal surfaces. *Physical Review B* **79**, 075441 (2009).

[97] Rubio-Bollinger, G., Joyez, P. & Agraït, N. Metallic Adhesion in Atomic-Size Junctions. *Physical Review Letters* **93**, 1–4 (2004).

[98] Frei, M., Aradhya, S. V., Koentopp, M., Hybertsen, M. S. & Venkataraman, L. Mechanics and chemistry: single molecule bond rupture forces correlate with molecular backbone structure. *Nano letters* **11**, 1518–23 (2011).

[99] Rief, M. Reversible Unfolding of Individual Titin Immunoglobulin Domains by AFM. *Science* **276**, 1109–1112 (1997).

[100] Kellermayer, M. S. Folding-Unfolding Transitions in Single Titin Molecules Characterized with Laser Tweezers. *Science* **276**, 1112–1116 (1997).

[101] Puchner, E. M., Franzen, G., Gautel, M. & Gaub, H. E. Comparing proteins by their unfolding pattern. *Biophysical journal* **95**, 426–34 (2008).

[102] Ternes, M., Lutz, C. P., Hirjibehedin, C. F., Giessibl, F. J. & Heinrich, A. J. The force needed to move an atom on a surface. *Science (New York, N.Y.)* **319**, 1066–9 (2008).

[103] Wagner, C., Fournier, N., Tautz, F. & Temirov, R. Measurement of the Binding Energies of the Organic-Metal Perylene-Teracarboxylic-Dianhydride/Au(111) Bonds by Molecular Manipulation Using an Atomic Force Microscope. *Physical Review Letters* **109**, 1–5 (2012).

[104] Langewisch, G., Falter, J., Fuchs, H. & Schirmeisen, a. Forces During the Controlled Displacement of Organic Molecules. *Physical Review Letters* **110**, 036101 (2013).

[105] Bernardo, C. & Gomes, J. Cluster model DFT study of acetylene adsorption on the Cu (100) surface. *Journal of Molecular Structure: THEOCHEM* **629**, 251–261 (2003).

[106] Pawin, G. *et al.* A surface coordination network based on substrate-derived metal adatoms with local charge excess. *Angewandte Chemie (International ed. in English)* **47**, 8442–5 (2008).

[107] van de Walle, A. & Ceder, G. Correcting overbinding in local-density-approximation calculations. *Physical Review B* **59**, 14992–15001 (1999).

[108] Staroverov, V., Scuseria, G., Tao, J. & Perdew, J. Tests of a ladder of density functionals for bulk solids and surfaces. *Physical Review B* **69**, 075102 (2004).

[109] Gupta, J., Lutz, C., Heinrich, a. & Eigler, D. Strongly coverage-dependent excitations of adsorbed molecular hydrogen. *Physical Review B* **71**, 1–5 (2005).

[110] Astumian, R. D. Thermodynamics and Kinetics of a Brownian Motor. *Science* **276**, 917–922 (1997).

[111] Douglass, J. K., Wilkens, L., Pantazelou, E. & Moss, F. Noise enhancement of information transfer in crayfish mechanoreceptors by stochastic resonance. *Nature* **365**, 337–40 (1993).

[112] Wiesenfeld, K. & Moss, F. Stochastic resonance and the benefits of noise: from ice ages to crayfish and SQUIDs. *Nature* **373**, 33–6 (1995).

[113] Kiselev, S. I. *et al.* Microwave oscillations of a nanomagnet driven by a spin-polarized current. *Nature* **425**, 380–3 (2003).

[114] Gammaitoni, L., Hänggi, P., Jung, P. & Marchesoni, F. Stochastic resonance. *Reviews of Modern Physics* **70**, 223–287 (1998).

[115] Stipe, B. C. Inducing and Viewing the Rotational Motion of a Single Molecule. *Science* **279**, 1907–1909 (1998).

[116] Thijssen, W., Djukic, D., Otte, A., Bremmer, R. & van Ruitenbeek, J. Vibrationally Induced Two-Level Systems in Single-Molecule Junctions. *Physical Review Letters* **97**, 226806 (2006).

[117] Horcas, I. *et al.* Wsxm: A software for scanning probe microscopy and a tool for nanotechnology. *Review of Scientific Instruments* **78**, 013705 (2007).

[118] Halbritter, a., Makk, P., Csonka, S. & Mihály, G. Huge negative differential conductance in Au-H_2 molecular nanojunctions. *Physical Review B* **77**, 075402 (2008).

[119] Trouwborst, M., Huisman, E., van der Molen, S. & van Wees, B. Bistable hysteresis and resistance switching in hydrogen-gold junctions. *Physical Review B* **80**, 081407 (2009).

[120] Temirov, R., Soubatch, S., Neucheva, O., Lassise, a. C. & Tautz, F. S. A novel method achieving ultra-high geometrical resolution in scanning tunnelling microscopy. *New Journal of Physics* **10**, 053012 (2008).

[121] Weiss, C. *et al.* Imaging Pauli Repulsion in Scanning Tunneling Microscopy. *Physical Review Letters* **105**, 086103 (2010).

[122] Stipe, B. C. Single-Molecule Vibrational Spectroscopy and Microscopy. *Science* **280**, 1732–1735 (1998).

[123] Smit, R. H. M. *et al.* Measurement of the conductance of a hydrogen molecule. *Nature* **419**, 906–9 (2002).

[124] Djukic, D. *et al.* Stretching dependence of the vibration modes of a single-molecule Pt-H2-Pt bridge. *Physical Review B* **71**, 161402 (2005).

[125] Brumme, T. *et al.* Dynamical bistability of single-molecule junctions: A combined experimental and theoretical study of PTCDA on Ag(111). *Physical Review B* **84**, 115449 (2011).

[126] Tierney, H. L. *et al.* Experimental demonstration of a single-molecule electric motor. *Nature nanotechnology* **6**, 625–9 (2011).

[127] Steele, G. a. *et al.* Strong coupling between single-electron tunneling and nanomechanical motion. *Science (New York, N.Y.)* **325**, 1103–7 (2009).

[128] Lassagne, B. *et al.* Coupling mechanics to charge transport in carbon nanotube mechanical resonators. *Science (New York, N.Y.)* **325**, 1107–10 (2009).

[129] Tekiel, A., Miyahara, Y., Topple, J. M. & Grutter, P. Room-temperature single-electron charging detected by electrostatic force microscopy. *ACS nano* **7**, 4683–90 (2013).

[130] Fernández-Torrente, I., Kreikemeyer-Lorenzo, D., Stróżecka, A., Franke, K. J. & Pascual, J. I. Gating the Charge State of Single Molecules by Local Electric Fields. *Physical Review Letters* **108**, 036801 (2012).

[131] Park, H. *et al.* Nanomechanical oscillations in a single-C60 transistor. *Nature* **407**, 57–60 (2000).

[132] Ferraris, J. *et al.* Electron transfer in a new highly conducting donor-acceptor complex. *Journal of the American Chemical Society* **95**, 948–949 (1973).

[133] Fernández-Torrente, I., Franke, K. & Pascual, J. Vibrational Kondo Effect in Pure Organic Charge-Transfer Assemblies. *Physical Review Letters* **101**, 2–5 (2008).

[134] Kitamura, S. & Iwatsuki, M. High-resolution imaging of contact potential difference with ultrahigh vacuum noncontact atomic force microscope. *Applied Physics Letters* **72**, 3154 (1998).

[135] Schulz, F. *Towards Measuring the Force of an Electron : Molecular Charge Transfer Investigated by Combined Scanning Tunneling and Atomic Force Microscopy*. Master's thesis (2012).

[136] König, T., Heinke, L., Simon, G. & Heyde, M. Three-dimensional electrostatic interactions in dynamic force microscopy: Experiment and theory. *Physical Review B* **83**, 1–6 (2011).

[137] Asaki, N. S. & Sukada, M. T. Effect of Microscopic Nonconservative Process on Noncontact Atomic Force Microscopy. *Jpn. J. Appl. Phys.* **39**, 1334–1337 (2000).

[138] Kantorovich, L. & Trevethan, T. General Theory of Microscopic Dynamical Response in Surface Probe Microscopy: From Imaging to Dissipation. *Physical Review Letters* **93**, 236102 (2004).

[139] Cockins, L. & Miyahara, Y. Energy levels of few-electron quantum dots imaged and characterized by atomic force microscopy. *PNAS* **107**, 9496–501 (2010).

[140] Nazin, G., Qiu, X. & Ho, W. Charging and Interaction of Individual Impurities in a Monolayer Organic Crystal. *Physical Review Letters* **95**, 166103 (2005).

[141] Pradhan, N. a., Liu, N., Silien, C. & Ho, W. Atomic Scale Conductance Induced by Single Impurity Charging. *Physical Review Letters* **94**, 076801 (2005).

[142] Choi, B.-Y. *et al.* Conformational Molecular Switch of the Azobenzene Molecule: A Scanning Tunneling Microscopy Study. *Physical Review Letters* **96**, 1–4 (2006).

[143] Alemani, M. *et al.* Adsorption and Switching Properties of Azobenzene Derivatives on Different Noble Metal Surfaces: Au(111), Cu(111), and Au(100). *Journal of Physical Chemistry C* **112**, 10509–10514 (2008).

[144] Sysoiev, D. *et al.* Pronounced effects on switching efficiency of diarylcycloalkenes upon cycloalkene ring contraction. *Chemical communications (Cambridge, England)* **48**, 11355–7 (2012).

[145] Scheurer, F., Speisser, V. & Carrie, B. Oligothiophene Nanorings as Electron Resonators for Whispering Gallery Modes **056802**, 1–5 (2013).

[146] Pavliček, N., Swart, I., Niedenführ, J., Meyer, G. & Repp, J. Symmetry Dependence of Vibration-Assisted Tunneling. *Physical Review Letters* **110**, 136101 (2013).

[147] Gross, L. *et al.* Bond-order discrimination by atomic force microscopy. *Science (New York, N.Y.)* **337**, 1326–9 (2012).

[148] Pavliček, N. *et al.* Atomic Force Microscopy Reveals Bistable Configurations of Dibenzo[a,h]thianthrene and their Interconversion Pathway. *Physical Review Letters* **108**, 086101 (2012).

[149] Albrecht, F., Neu, M., Quest, C., Swart, I. & Repp, J. Formation and Characterization of a Molecule-Metal-Molecule Bridge in Real Space. *Journal of the American Chemical Society* **135**, 9200–3 (2013).

[150] Cottone, G., Noto, R. & La Manna, G. Theoretical study of spiropyran-merocyanine thermal isomerization. *Chemical Physics Letters* **388**, 218–222 (2004).

[151] Schulze, G., Franke, K. J. & Pascual, J. I. Induction of a Photostationary Ring-Opening-Ring-Closing State of Spiropyran Monolayers on the Semimetallic Bi(110) Surface. *Physical Review Letters* **109**, 026102 (2012).

[152] Görner, H. Photochromism of nitrospiropyrans: effects of structure, solvent and temperature. *Physical Chemistry Chemical Physics* **3**, 416–423 (2001).

[153] Chibisov, A. K. & Görner, H. Singlet versus triplet photoprocesses in indodicarbocyanine dyes and spiropyran-derived merocyanines. *Journal of Photochemistry and Photobiology A: Chemistry* **105**, 261–267 (1997).

[154] Allinger, N. L. Conformational analysis. 130. MM2. A hydrocarbon force field utilizing V1 and V2 torsional terms. *Journal of the American Chemical Society* **99**, 8127–8134 (1977).

[155] Lapienis-Grochowska, D., Kryszewski, M. & Nadolski, B. Electronic structure of merocyanine form of indolinespirobenzopyrans determined by electronic spectroscopy and dielectric measurements. *Journal of the Chemical Society, Faraday Transactions 2* **75**, 312 (1979).

[156] Bletz, M., Pfeifer-Fukumura, U., Kolb, U. & Baumann, W. Ground- and First-Excited-Singlet-State Electric Dipole Moments of Some Photochromic Spirobenzopyrans in Their Spiropyran and Merocyanine Form. *The Journal of Physical Chemistry A* **106**, 2232–2236 (2002).

[157] Sadewasser, S. *et al.* New Insights on Atomic-Resolution Frequency-Modulation Kelvin-Probe Force-Microscopy Imaging of Semiconductors. *Physical Review Letters* **103**, 5–8 (2009).

[158] Moll, N., Gross, L., Mohn, F., Curioni, A. & Meyer, G. The mechanisms underlying the enhanced resolution of atomic force microscopy with functionalized tips. *New Journal of Physics* **12**, 125020 (2010).

[159] M. J. Frisch *et al.* Gaussian 09 Revision A.1 Gaussian Inc. Wallingford CT 2009.

[160] FU Berlin, ZEDAT. High-Performance Computing, Wissenschaftliches Rechnen an der Freien Universität Berlin. *website, available online* `http://www.zedat.fu-berlin.de/Compute/Home`, visited: Jul. 12th 2013.

[161] Chen, X., Sun, S., Li, F., Wang, X. & Xia, D. The interactions of oxygen with small gold clusters on nitrogen-doped graphene. *Molecules (Basel, Switzerland)* **18**, 3279–91 (2013).

[162] Yoon, B., Häkkinen, H. & Landman, U. Interaction of O_2 with Gold Clusters: Molecular and Dissociative Adsorption. *The Journal of Physical Chemistry A* **107**, 4066–4071 (2003).

[163] Bocquet, F., Nony, L. & Loppacher, C. Polarization effects in Non-Contact Atomic Force Microscopy : a key to model the tip-sample interaction above charged adatoms **83**, 1–32 (2011).

[164] Latscha, H. P., Kazmaier, U. & Klein, H. A. *Organische Chemie*. Springer-Lehrbuch (Springer Berlin Heidelberg, Berlin, Heidelberg, 2008).

[165] Allinger, N. L., Zhou, X. & Bergsma, J. Molecular mechanics parameters. *Journal of Molecular Structure: THEOCHEM* **312**, 69–83 (1994).

[166] Schulze, G. Tinsurbui. *Software for creating surfaces in tinker input files, contact author for more information* Email: gunnar.schulze@physik.fu-berlin.de.

[167] Ponder, J. W. & Richards, F. M. An efficient newton-like method for molecular mechanics energy minimization of large molecules. *Journal of Computational Chemistry* **8**, 1016–1024 (1987).

Acknowledgements

I would particularly like to thank Prof. J. I. Pascual for giving me the opportunity to write this thesis in his group, to set up this fantastic machine, and the possibility to perform so many fascinating experiments, but also for a great atmosphere in the group, lots of support and being always willing to listen to everything.

Prof. Stephanie Reich has my gratitude as my second supervisor and co-referee of this thesis.

My special thanks to Prof. Katharina J. Franke for great help and support in all matters.

Many thanks also to Felix von Oppen for a great collaboration in the hydrogen puzzle, and Alessandro Pecchia and Thomas Niehaus for the detailed theoretical lifting of a molecular wire.

Thanks to the AFM team, Martina Corso, Fabian Schulz, Nils Krane and Xianwen Chen for great results from so many different experiments. I want to thank Gunnar Schulze who shared an office with me for more than 4 years, we had great discussions about everything. Many more thanks also to all my present and former co-workers in the Pascual and Franke groups!

But there is also a life outside the lab. Many many thanks to Kerstin Tote for her great support, encouragement, patience in the last weeks of writing and above all for being there. And, last but not least thanks to my parents, grandparents and my brother for their support and help for as long as I can remember.

This work was possible also due to funding by the German Research Foundation (DFG) within the framework of the Collaborative Research Centre 658 'Elementary Processes in Molecular Switches at Surfaces'.

List of Publications

Publications related to this thesis

Christian Lotze, Martina Corso, Katharina J. Franke,
Felix von Oppen and José Ignacio Pascual
Driving a Macroscopic Oscillator with the Stochastic Motion of a Hydrogen Molecule
Science **338**, 779 (2012)

Publications not related to this thesis

Ch Lotze, Y Luo, M Corso, K J Franke, R Haag and J I Pascual,
Reversible electron-induced cis-trans isomerization mediated by intermolecular interactions
J. Phys.: Condens. Matter **24**, 394016 (2012)

T. R. Umbach, I. Fernández-Torrente, M. Ruby, F. Schulz, C. Lotze, R. Rurali,
M. Persson, J. I. Pascual, K. J. Franke
Atypical charge redistribution over a charge-transfer monolayer on a metal
New J. Phys. **15**, 083048 (2013)

Anna Stróżecka, Jingcheng Li, Robin Schürmann, Gunnar Schulze, Martina Corso,
Fabian Schulz, Christian Lotze, Sascha Sadewasser, Katharina J. Franke,
and José Ignacio Pascual
Multiple radiative pathways in electron induced luminescence of copper nitride nanocrystals
submitted

Contributions to Conferences

2009 Oral Contribution:
DPG-Frühjahrstagung der Sektion Kondensierte Materie (SKM) in Dresden 22.-27.3.2009
Conformational changes of an imine-based molecular switch on the Au(111) surface

Poster:
Joint meeting of Sfb 677 and Sfb 658 on Molecular Switches: Elementary Processes and Applications, Salzau 27.- 29.5.2009
Adsorption of Azobenzene Based Molecular Switches on a Au(111) surface

2010 Oral Contribution:
DPG-Frühjahrstagung der Sektion Kondensierte Materie (SKM) in Regensburg 21.–26.3.2010
Electron Induced Conformational Changes of Imine-based Molecular Switches on a Au(111) Surface

2011 Oral Contributions:
DPG-Frühjahrstagung der Sektion Kondensierte Materie (SKM) in Dresden 13.-18.3.2011
Dynamic Force Spectroscopy at a Single Molecule Junction

14th. International Conference on Noncontact Atomic Force Microscopy, 18.-22.9.2011
Dynamic Force Spectroscopy at the Single Molecule Junction

Workshop of the SFB 658-Integrated Research Training Group, Lübbenau 11.-12.8.2011
Dynamic Force Spectroscopy at the Single Molecule Junction

One-day Symposium on "Transport through Molecules" of the SFB 658, 21.10.2011
*Current-induced Forces in a Hydrogen Molecular Junc*tion

Poster:
WEH-Seminar on SCANNING PROBE TECHNIQUES, 28.11.-1.12.2011
Dynamic Force Spectroscopy at the Single Molecule Junction

2012 Oral Contributions:
DPG-Frühjahrstagung der Sektion Kondensierte Materie (SKM) in Berlin 27.2.-2.3.2012
Atomic Forces and Energy Dissipation of a Bi-Stable Molecular Junction

15th. International Conference on Noncontact Atomic Force Microscopy in Český Krumlov, CR, 1.-5.07.2012
Atomic Forces and Energy Dissipation of a Bi-Stable Molecular Junction

AVS, Tampa, Florida, USA 28.10.-2.11.2012
Atomic Forces and Energy Dissipation of a Bi-Stable Molecular Junction

Poster:
International SFB 658 Symposium on "Molecular Switches", Potsdam 20.2.2012
Dynamic Force Spectroscopy at the Single Molecule Junction

Berlin Symposium on Surface Science: „From Reciprocal to Real Space“, 12.-14.9.2012
Driving a Macroscopic Oscillator with the Stochastic Motion of a Hydrogen Molecule

2013 Oral Contributions:
Invited Talk: Fritz Haber Institut Berlin, Department seminar Physical Chemistry, 21.1.2013
Driving a Macroscopic Oscillator with the Stochastic Motion of a Hydrogen Molecule

DPG-Frühjahrstagung der Sektion Kondensierte Materie (SKM) in Regensburg 10.-15.3.2013
Driving a Macroscopic Oscillator with the Stochastic Motion of a Hydrogen Molecule

Workshop of the SFB 658-Integrated Research Training Group, Zeuthen 16.,17.5.2013
Driving a Macroscopic Oscillator with the Stochastic Motion of a Hydrogen Molecule